SUB- CONTINENTAL LITHOSPHERIC MANTLE DEFORMATION IN THE YERER-TULLU WELLEL VOLCANOTECTONIC LINEAMENT: A STUDY OF PERIDOTITE XENOLITHS

By

Kaitlyn R. Trestrail

A THESIS

Submitted to
Michigan State University
in partial fulfillment of the requirements
for the degree of

Geological Sciences – Master of Science

2016

ABSTRACT

SUB- CONTINENTAL LITHOSPHERIC MANTLE DEFORMATION IN THE YERER-TULLU WELLEL VOLCANOTECTONIC LINEAMENT: A STUDY OF PERIDOTITE XENOLITHS

By

Kaitlyn R. Trestrail

Volumetrically, the lithospheric mantle comprises the bulk of the continental lithosphere, yet the mechanisms by which the lithospheric mantle is deformed during rifting are unresolved. Stretching and thermo-mechanical erosion are often cited mechanisms for facilitating lithospheric deformation during continental rift development; however, the infiltration of melt into the lithosphere during rift development also results in chemical alteration of the lithospheric mantle. The purpose of this study is to test the potential mechanisms by which the continental lithospheric mantle is chemically altered during rift development. Here we present a study of mantle xenoliths derived from the lithospheric mantle in Ethiopia that has been deformed during rifting. We find that the lithospheric mantle beneath the this zone exhibits evidence of focused magma-lithosphere interaction, resulting in four distinct types of peridotite xenoliths: a) deformed xenoliths representing the pre-deformation lithospheric mantle; b) granular xenoliths representing overprinted lithospheric mantle; c) replacement dunite xenoliths, evidence of pervasive melt-lithosphere interaction; and d) cumulate xenoliths representing remnants of a metasomatic agent. The deformed xenoliths exhibit a high Mg# (>89) and exhibit little, if any, interaction with melt. The remaining xenolith groups exhibit lower Mg# (<89) suggestive of magma-lithosphere interaction. The high Ni content in olivine and depleted incompatible elements in orthopyroxene of the granular xenoliths are inconsistent with simple metasomatic enrichment and the existence of dunite with olivine (low Ca and Sc) and spinel (Cr# ~60) compositions is inconsistent with a cumulate origin, instead suggesting a replacement dunite. Our samples are derived from a zone of intensely sheared lithosphere and we suggest that melt channeling is preferred over chromatographic metasomatism due to melt focusing along steep topography on the lithosphere-asthenosphere boundary and shear-induced porosity.

ACKNOWLEDGMENTS

This work was made possible by the support and encouragement from many people and parties:

Special thanks to National Science Foundation (NSF) Petrology & Geochemistry program: EAR-1219647 for supporting this research. Your funding was instrumental to the data collection for this project. I would also like to thank the Michigan State Department of Geological Sciences for the fellowships and scholarships that made my education possible.

I would like to thank my committee members, Michael Velbel and Julie Libarkin, for all of the guidance and support during this project. Without your valuable feedback, this thesis would have been an impossible task. Thank you to Guillaume Girard for his help with the LA-ICP-MS on multiple data runs, data processing and precision analysis. His knowledge and improved mythology made these data possible.

Thank you to my family, Andy, Laurie, and Andrew Trestrail, for supporting me throughout my education, encouraging me to do my best, and for not making fun of me (too much) for having an unhealthy obsession with rocks.

Thank you Susan Krans, my 'big geosis', for all of your advice, time spent figuring out my data, and for being an incredible listener. Your friendship has been one of the greatest gifts I have received from my master's education. Thank you to Charles Hackel, for continuing to be my best friend throughout the making of this research. I couldn't have done it without you.

Lastly, a very special thank you goes to Tyrone Rooney. You have been by my side for my entire research career and I can safely say that you have molded me into something that I am extremely proud of. You've taught me how to ask questions (and then ask another), how to write (better), and to always expect a visit from the Spanish Inquisition!

TABLE OF CONTENTS

LIST OF TABLES

LIST OF FIGURES

KEY TO ABBREVIATIONS

ANS: Arabian-Nubian Shield

BTSH: Boru-Toru Structural High

CMER: Central Main Ethiopian Rift

EARS: East African Rift System

HFSE: High field strength elements

HREE: Heavy rare earth elements

KED: Kinetic Electron Dispersion

LA-ICP-MS: Laser ablation- inductively coupled plasma mass spectrometer

LILE: Large-ion lithophile element

LREE: Light rare earth elements

MER: Main Ethiopian Rift

NMER: Northern Main Ethiopian Rift

PGE: Platinum-group element

PPL: Plain-polarized light

REE: Rare earth element

SCLM: Sub-continental lithospheric mantle

SMER: Southern Main Ethiopian Rift

XPL: Crossed-polarized light

YTVL: Yerer-Tullu Wellel Volcanotectonic Lineament

1. Introduction

During the rifting of a continent, the thick continental lithosphere must transition to thinner, chemically distinct, oceanic lithosphere. Our current understanding of this transitional process is dominated by observations of crustal extension, which have shown that thick silicic continental crust is converted into thin mafic oceanic crust through a variety of stretching and intrusion mechanisms (e.g., Courtillot et al., 1999; Buck, 2006; Agostini et al., 2011; Corti, 2012). Comparatively few constraints exist as to how the volumetrically more significant subcontinental lithospheric mantle (SCLM) is deformed and removed during continental rifting (Kay and Kay, 1993; Zeyen et al., 1997; Morency et al., 2002). There are two dominant endmember processes that facilitate deformation of the lithospheric mantle during rifting: (1) simple shear and ductile stretching (e.g., Wiessel & Karner, 1989; Wilson et al., 2005), and (2) thermo-chemical alteration of the lithospheric mantle (e.g., Bedini et al, 1997; Vauchez et al., 1998).

Mechanical deformation and stretching of the lithospheric mantle is well constrained through the application of various geophysical techniques and associated modeling, which have provided details as to the thickness of the continental lithosphere at various stages of rift development (e.g., Begg et al., 2009; Huismans & Beaumont, 2011). However, the subtle geochemical changes imposed by thermo-chemical deformation of the mantle make it difficult to unambiguously resolve how lithospheric structure may be perturbed during rifting. Although evidence of prior thermo-chemical deformation of the continental lithospheric mantle is preserved in portions of the lithospheric mantle exhumed during late-stage extension (e.g., Lavier & Manatschal, 2006), direct investigation of large sections of the lithospheric mantle is not possible during the rifting process. Xenoliths, small pieces of the SCLM brought to the Earth's surface in volcanic eruptions, provide an alternative window into the SCLM and can provide insight into the processes that occur in the mantle during rifting (e.g., Bedini et al., 1997; Roger et al., 1999; Ferrando et al, 2007; le Roux et al., 2014).

Within the East African Rift, mantle xenolith studies have provided an important record of the establishment, evolution, and recent modification of the SCLM. Re/Os studies have provided constraints on the initial lithospheric age (e.g., Chesley et al., 1999; Reisberg et al., 1999); isotopic and trace element studies have revealed evidence of multi-stage metasomatic enrichment of the mantle by a variety of metasomatic agents (e.g., Rudnick et al., 1993; Bedini et al., 1997; Lee et al., 2000); and petrographic and textural evidence has demonstrated evidence of lithospheric chemical deformation (e.g., Kaeser et al., 2006). Increasingly, there is recognition that lithospheric deformation may promote enhanced metasomatic processes. Simple shear of the lithospheric mantle may create topography along the lithosphere-asthenosphere boundary, promoting focused flow of magmas into the lithosphere and creating pronounced thermo-chemical alteration of the lithospheric mantle (e.g., Havlin et al., 2013). While rift-border faults provide a potential nexus for such lithospheric modification (Corti, 2012), the intersection of a rift with a pre-existing lineament provides a particularly effective avenue for the focusing of magmas into the lithospheric mantle (Rooney et al., 2014a).

Here we present petrographic and geochemical data from peridotite xenoliths hosted by ~5 Ma lavas collected along the western portion of the Yerer-Tullu Wellel volcano-tectonic lineament (YTVL), an east-west trending feature adjacent to the Main Ethiopian Rift (MER) [Figure 1], which represents a lithospheric weakness formed during the Pan-African orogeny **(**Rooney et al., 2014a). We evaluate the characteristics of the lithospheric mantle in this region and how it has responded to extensional strain and metasomatism by examining xenolith petrography and phase geochemistry. Our work builds upon the earlier studies that explored the thermal and chemical conditions of the upper mantle in this region (e.g., Conticelli et al., 1999; Ferrando et al., 2008). A common conclusion of these studies was that the textural and compositional characteristics of the SCLM was the result of recrystallization due to varying degrees of interaction with the Afar plume (e.g., Bedini et al., 1997; Roger et al., 1999; Ferrando et al, 2008). While the Afar plume is influential, the absence of pervasive alteration of the SCLM has led to the development of speculative models suggesting the eruption of the Ethiopian Flood basalts was facilitated

by channelized magma flow in the lithospheric mantle (Roger et al., 1999). We present a model of channelized flow in the SCLM beneath the YTVL developed from observations using peridotite xenoliths. Our results show that focused flow resulted in the formation of depleted lithologies (dunite) by the dissolution of phases such as pyroxene. In xenoliths less affected by melt-rock reaction, the formation of granular texture was accompanied by a depletion of the more incompatible trace elements. The results of this study show that focused flow beneath the YTVL has significantly altered the lithological and geochemical composition of the lithospheric mantle, confirming previous conceptual models of channelized flow of magma through the African lithosphere.

2. Background

Many of the geologic processes and phenomena that occur today in East Africa are the result of, or influenced by, the geologic history of the Pan-African orogeny. The Pan-African orogeny consisted of a series of collisions that ultimately resulted in the formation of the supercontinents of Gondwanaland and Pannotia (Cutten, 2002) along the Pan-African Mozambique Belt of East Africa (McWilliams, 1981). The Arabian-Nubian Shield (ANS) (i.e., the area from Jordan south to Sudan and from western Egypt to eastern Saudi Arabia) was formed by the Pan-African Orogeny from approximately 1,200 to 550 Ma (Stein & Goldsetin, 1996). ANS magmatic history is divided into four phases: Phase I being the erupting of tholeiitic basalts from 900 to 870 Ma, phase II being island-arc calc-alkaline magmatism from 870 to ~650 Ma, phase III being pervasive metamorphism and the formation of granitic batholiths from 640 to 600 Ma, and phase IV being the creation of alkaline granites and dolerites from 600 Ma to ~540 Ma (Bentor, 1985). Pb, Sr, Nd, and O isotopes from the core region of the ANS indicate a lack of pre-established continental crust prior to the above mentioned events (Stein & Goldstein, 1996).

Phase I (900 to 870 Ma), the eruption of tholeiitic basalts and sediments such as volcanogenic clastics and breccias, suggests an initial oceanic setting in which magmas were erupted at a very high rate creating an oceanic plateau. REE patterns of tholeiitic basalts from Phase I are relatively flat and similar to those of known oceanic plateaus (e.g., Ontong Java Pleateau) (Stein & Goldstein, 1996), suggesting a similar origin.

Phase II (~870 – ~650 Ma), island-arc calc-alkaline magmatism, likely occurred as a result of the arrival of the oceanic plateau at a plate margin generating calc-alkaline andesites and diorite-tonalite-trondhjemites (Bentor, 1985). Phase II calc-alkaline magmas show more enriched LREE and fractionated HREE patterns (Stein & Goldstein, 1996) and it is suggested that the parent endmember for these calc-alkaline magams was a garnet lherzolite with a flat REE pattern (Stern, 1994), not unlike the REE pattern

seen in Phase I tholeiitic magmas. Phase II magmas were generated at an anomalously high volume suggesting a thermal anomaly as a result of a rising plume head (Stein & Goldstein, 1996).

Phase III (640 – 600 Ma) pervasive metamorphism and formation of granitic batholiths suggest the initiation of the assembly of the Pan-African continent, where the lithosphere is significantly thickened and metamorphosed and large volumes of calc-alkaline granitoids, gabbros, and diorites were generated as a result of a major collisional event with other ANS terrains and other cratons. REE patterns in Phase III are comparable to other Archean and Proterozoic orogenies (Stein & Goldstein, 1996).

Lastly, Phase IV (600 – ~540 Ma), the creation of alkaline granite and dolerites, further suggests the assembly of the Pan-African continent followed by the extension of the lithosphere and crust. Phase IV alkaline granites show a negative Eu anomaly and low Sr content, suggesting plagioclase fractionation of mafic melts, likely due to the presence of normal faulting and volcanoclastic sedimentation (Stein & Goldstein, 1996).

The inherent lithospheric weaknesses resulting from the Pan-African Orogeny have influenced the lithosphere and lithospheric mantle in East Africa, creating optimal zones for shearing (Abebe et al., 1998; Keranen et al., 2008). The YTVL is suggested to be a terrain boundary between a northern and southern section of Precambrian crust, with Oligocene underplating to the north but not in the south. Therefore the YTVL, a structural weakness created though the Pan-African orogeny, may aid in focused melt intrusion into the SCLM.

2.1 East African Rift System

The East African Rift System (EARS) is the largest active continental rifting system in the world. It stretches from the Afar triple junction to Mozambique in a north-south fashion [Figure 1]. The EARS is comprised of three main components: the Afar dome, the East African dome, and the Turkana depression. The Afar dome, in the north, is a topographic swell that extends from the eastern border of Sudan to the western edge of Ethiopia. It reaches as far north as Yemen and extends south to the southern border of

Ethiopia. The East African dome is the southern topographic swell that extends from the eastern border of the Democratic Republic of the Congo to the eastern border of Kenya and from Kenya to the northern border of Tanzania. The Turkana Depression separates the two domes. The northernmost branch of the EARS, referred to as the Main Ethiopian Rift (MER) lies between the east-west trending Ethiopian and Somalian plateaus – the two major topographic highs in this region [Figure 2]. The MER is divided into three sub-regions based on stages of continental rifting, magmatism, deformation and structure (Corti, 2009): The Northern Main Ethiopian Rift (NMER), which extends southwestward from the Afar –MER boundary, bounds the Central Main Ethiopian Rift (CMER) at the Boru Toru Structural High (BTSH) (Bonini et al., 2005); the CMER continues southwestward and is bounded by the Southern Main Ethiopian Rift (SMER), at approximately 7° N.; the SMER stretches southward to the Turkana depression (~5° N) where it is accommodated by a series of basin and ranges [Figure 2].

2.2 Magmatism in the EARS

Since the Eocene, the MER has experienced episodic volcanism and magmatic activity which has influenced the structure and tectonics of the region (Burke, 1996; Wolfenden et al., 2004; Corti et al., 2009). Magmatism in the EARS began at approximately 40-45 Ma in the Turkana depression and the EARS has been volcanically active intermittently since then (Furman et al., 2007). At ~30 Ma, magmatism was dominated by the rapid eruption of the 2000 meter thick flood basalt province centered on Ethiopia. Approximately 350,000 km^3 of basalt was extruded covering an area of approximately 600,000 km^2 in Ethiopia and Eritrea (Mohr, 1983; Furman et al., 2007) and is associated with the breakup of the Afro-Arabian shield – the event responsible for forming the Red Sea and Gulf of Aden (Wolfenden et al., 2004). From ~29-10 Ma, the EARS experienced intermittent episodic volcanism in Turkana and southern Ethiopia (Furman et. al., 2007). Volcanism also occurred along the Ethiopian Plateau with the eruption of isolated shield volcanoes during this time period (Kieffer et al., 2004). Quaternary volcanic activity along the MER occurs as a result of the oblique faults of the Wonji Fault belt system (Corti et al., 2009). Basalts are extruded along the NNE- SSW trending Wonji Fault belts forming small flows, scoria

cones and phreatomagmatic deposits (Abebe et al., 2005). Quaternary volcanic activity occurring on the plateau first developed in the Tana graben due to extension-related tectonics. Extension resulted in the formation of fissure-type lava fields, and small to medium tuff cones, rings and maars which erupted alkali basalts in the plateau region (Ferrando et al, 2008). Throughout its magmatic history, the MER has experienced extension as the continental lithosphere is actively deforming and eventually being converted to oceanic lithosphere.

2.3 Rift evolution

Evolution of the MER is an actively debated and unresolved topic due to the complexities of the structural, petrological and geochemical mechanisms involved (e.g. Wofenden et al., 2004; Bonini et al., 2005; Buck et al., 2006; Keranen et al., 2008; Corti et al., 2012). Wolfenden et al. (2004) proposes a northward propagation while alternative hypotheses suggests other mechanisms such as rift initiation via dike emplacement (Buck, 2006; Havlin et al., 2014) and stationary hotspot volcanism underlying a northward moving plate (Rogers, 2006) which suggests a southward propagation. Bonini et al. (2005) suggests a three-part evolution which encompasses a northward propagation in the SMER until 11 Ma followed by a southward propagation in the NMER, and eventually the formation of the CMER post 5-6 Ma. Keranen et al. (2008) argues for a north to south rift propagation starting in Afar, moving southward, stalling at the NMER-CMER boundary for some time, then continuing south through the CMER.

While most of the studies previously mentioned are based on surface structural evidence (Wolfenden et al., 2004; Bonini et al., 2005) and modeling approaches (Buck, 2006; Rogers, 2006), only the study by Keranen et al., (2008) takes lithospheric structure heterogeneities into account when assessing the evolution of the MER. They propose that structural evidence seen at the surface extends into the lithospheric mantle to influence rift propagation. They also indicate that the YTVL [Figure 3] plays an extremely important role in rift evolution by accommodating strain in the form of extensional strain from the NMER.

2.4 Yerer-Tullu Wellel Volcanotectonic Lineament

The YTVL, which is located within the Afar dome, stretches 700 km from the western edge of the MER at the NMER-CMER boundary to the Sudan border (Abebe et al., 1998). The YTVL is composed of a Proterozoic-Paleozoic basement with Mesozoic continental and marine sediments and Cenozoic volcanics (Abebe et al., 1998). The northern border of the YTVL is defined partially by the Ambo Fault System, an east-west trending structure that divides the Ethiopian plateau [Figure 2] and the edge of the thick mafic underplate beneath the Ethiopian Volcanic Plateau (Keranen et al., 2008) [Figure 3]. The southern border is less well defined.

Abebe et al. (1998) proposed that in the late Miocene (~12Ma) the YTVL accommodated extension of the MER along the Precambrian lithospheric weaknesses associated with the Ambo Fault System. This system is likely a remnant lithospheric weaknesses created during the Pan-African Orogeny (Stein & Goldstein, 1996). Based on P-wave velocities, Keranen et al. (2008) proposes that the YTVL accommodated extension from the NMER due to the influence of the thick mafic underplate under the Ethiopian Volcanic Plateau in addition to the Ambo Fault System. This east-west trending weakness combined with the lack of the thick mafic underplate seen under the plateau allowed volcanism to occur along the YTVL in several phases: 12-7 Ma further west, 6-2 Ma in the middle, and <1 Ma in the east (Abebe et al., 1998; Keranen et al., 2008).

Keranen et al., (2008) emphasizes the importance of understanding how pre-existing weaknesses or pre-rift structures in the crust and upper mantle influence the propagation of rifting [Figure 3]. While crustal structures can be studied easily along the YTVL, constraints on the behavior of the sub-continental lithospheric mantle during extension are lacking. Using peridotite mantle xenoliths, we can examine the state of the lithospheric mantle during the period of extension accommodation by the YTVL.

2.5 How mantle xenoliths record lithospheric mantle processes

To test how rift evolution influences the SCLM, mantle xenoliths can be examined to infer geochemical, structural and petrological processes that occur in the SCLM – particularly deformation of the lithospheric mantle and metasomatism (e.g. , Bedini et al., 1997; Roger et al., 1999; Ferrando et al, 2008; le Roux et al., 2014).

The xenoliths studied in Ethiopia exhibit the impact of a mantle plume on the continental lithosphere. On the Ethiopian plateau (Lake Tana Region), xenoliths exhibit evidence of interaction between the continental lithosphere and melts/fluids associated with the Afar plume (Conticelli et al., 1999; Roger et al., 1999; Ferrando et al., 2008; Frezzotti et al., 2010). Roger et al. (1999) conducted a comparative study between Oligocene and Quaternary hosted xenoliths from Lake Tana Province revealing that the lithospheric mantle beneath the Ethiopian plateau has been less affected by plume emplacement than the lithosphere beneath the axis of the rift. In the Sidamo region of Southern Ethiopia, similar studies investigated the influence of fluid percolation in lithospheric mantle to study thermo-mechanical erosion of the lower lithosphere via plume activity (Bedini et al., 1997; Lorand et al., 2003; Reisburg et al., 2004; Bianchini et al., 2014). These studies examined xenoliths for LILE (large-ion lithophile element) enrichment, platinum group element (PGE) chemistry and Os isotope data to support a model of chromatographic metasomatism associated with an ascending mantle plume (Bedini et al., 1997).

Our study area at Nekempte [Figure 2] on the Ethiopian Plateau has likely been affected by similar plume-lithosphere processes; however, it is also located along a significant Precambrian structural lineament, the YTVL. This study area thus provides an opportunity to examine not only metasomatic enrichment associated with an ascending mantle plume, but the impact of a zone of structural weakness on lithologies within the SCLM. To date, the only study known to provide constraints on xenoliths from this region is the thermobarometric study by Conticelli et al. (1999). That study, while limited in scope, provides a basis on which to build our current study. We expand upon earlier work by firstly, examining a

much more significant suite of xenoliths; and secondly, by applying laser ablation ICP-MS techniques to reveal trace element systematics of minerals within the xenoliths.

3. Methods

3.1 Sample selection

The mantle xenoliths presented in this study were collected from Nekempte, located about 250 km east of the Western border of the YTVL and 25 km south of the northern border of the YTVL [Figure 2]. These xenoliths erupted with Cenozoic lavas aged at 5.92 ± 0.18 Ma (Abebe et al., 1998). Approximately 150 xenolith samples were recovered from a quarry. Xenoliths were commonly peridotite and pyroxenite (examined in a different study) hosted in phonalite. Peridotite xenoliths were selected for analysis on the basis of freshness.

3.1.1 Analytical Methods - Laser ablation (LA)- ICP-MS

Through petrographic examination of the sample suite, four thin sections were selected for detailed geochemical analysis on the basis of how representative the sample was of the freshest samples in the overall population. In-situ laser ablation (LA)- Inductively Coupled Plasma Mass Spectrometer (ICP-MS) analyses was conducted using a Thermoscientific ICAP Q quadrupole ICP-MS at Michigan State University. The system consists of the ICP-MS and a Photon Machines Analyte G2 193 nm excimer laser ablation system equipped with a 15 x 15 HelEx sample chamber. The laser was set at 4.1 mJ/cm^{-2} fluence and 10 Hz repetition rate. The sample chamber was placed in a 0.75 L/min high-purity helium carrier gas flux at 1 atm. The laser was paired with the mass spectrometer used in kinetic energy dispersion (KED) mode for molecular interference reduction and ability to measure major elements. It was tuned using NIST612 for best signal intensity on Co, In, Th, and U as well as the lowest oxide production rate on ThO/Th (<0.7%) and lowest double charged cations on Ba^{2+}/ Ba (<2%) production rates. The analysis had a reproducibility of 5 replicated analyses of NIST SRM 612 on ^{59}Co, ^{115}In, ^{232}Th, and ^{238}U (1σ rsd <5%).

Calibration was achieved from a set of ~ 20 standards including fused powders and natural and synthetic basalt glass standards [See appendix A]. An internal standard correction was performed using two steps. The first step was to measure MgO for pyroxene and olivine and TiO_2 for spinel. Two isotopes

were measured: one as an internal standard and one as unknown for concentration correction. An arbitrary concentration was assumed to MgO or TiO_2 in the minerals. The second step was to normalize all elements for MgO of TiO_2 for the arbitrary value. Next, a sum of major element oxides was calculated as the oxides are likely to not equal 100%. Then, all major and trace elements were normalized to 100% oxides because only anhydrous minerals were analyzed and these will have exactly 100% oxides in them. In addition, the NMNH olivine (San Carlos) + diopside standards were analyzed as unknowns [Appendix A].

All chemical analytical data were collected from minerals grains that were at least one mineral grain distance from the xenolith-host lava contact. Olivine, orthopyroxene and clinopyroxene were typically ablated with a spot size of 110 microns for approximately 30 seconds, of which 20-25 seconds of the best signal was kept for processing. Smaller spot size was used sometimes for smaller crystals to avoid overlap. Olivine, orthopyroxene, clinopyroxene, and spinel were chosen prior to chemical analysis via petrographic analysis. Crystals were chosen carefully ensuring that they were large enough to for multiple ablation spots and did not display evidence of secondary alteration or fluid inclusion trails. Olivine, orthopyroxene, and clinopyroxene were analyzed for all major elements as well as trace elements including: Sc, V, Cr, Co, Ni, Cu, Zn, Ga, Sr, Y, Zr, Nb, Ba, La, Ce, Nd, Sm, Eu, Gd, Dy, Er, Yb, and Hf. Spinels were analyzed for major elements MgO, Al_2O_3, TiO_2, MnO, and FeO as well as trace elements Sc, V, Cr, Co, Ni, Cu, Zn, and Ga. Data processing was performed using Qtegra software for masspectrometry.

Replicated analyses of JB1a and BHVO-1 fused powder standards interspersed between samples were run every ~1 hour [Appendix A]. Precision was normally within <5% (1σ) at concentrations typical of basalt standards. Precision at lower concentrations was estimated from peridotite fused powder standards PCC-1 and DTS- 1 run as unknowns [Appendix B]. Detection limit [Table 1] is defined at 3 times standard deviation (1σ) on gas blank measurements. Any values less than the detection limit were omitted.

4. Petrography

Physical deformation (e.g. kink banding and undulose extinction) and chemical enrichment (e.g. pargasitic amphibole/phlogopite, fluid inclusions) processes in the SCLM may be revealed through petrographic examination of mantle xenoliths. Ferrando et al. (2008) classified the spinel-lherzolite xenoliths from Injibara, Ethiopia [Figure 2] based on their petrography, specifically the amount of recrystallization (which they attributed to thermal activity), and provided a comprehensive analysis of peridotite mantle xenoliths from the Lake Tana region in Ethiopia [Figure 2]. To a first order, we adopt the classification scheme presented by Ferrando et al. (2008), with the presumption that large scale processes that have impacted the Northern Ethiopian Plateau, also affect our study area in the South.

Ferrando et al. (2008) divided their xenoliths into three groups: deformed, granular and transitional; deformed having minimal recrystallization (~ less than 30% of the xenolith), granular having a considerable amount (~more than 30% of the xenolith), and transitional forming a bridge between the two endpoints. The deformed spinel lherzolite xenoliths contain two generations of olivine (Ol I, Ol II_D) and orthopyroxene (Opx I, Opx II_D), the first being coarse (~4 mm) and the second fine (<1 mm). Clinopyroxene (Cpx I), spinel (Spl I), amphibole crystals, and intragranular fluid inclusion trails also occur.

The granular xenoliths are characterized by having more second generation olivine (Ol II_G), orthopyroxene (Opx II_G), and spinel (Spl II_G). There are fewer first generation crystals such as olivine (Ol I), orthopyroxene (Opx I), and clinopyroxene (Cpx I). Amphibole is present but sparsely distributed. Transitional xenoliths are intermediate between deformed and granular xenoliths. Ferrando et al., (2008) constrained the P-T conditions of these mantle xenoliths to a pressure range of about 1.3- 2.0 GPa and to have undergone multiple thermal events. In deformed and granular samples, temperatures range from 947 – 1015° C for the first generation crystals. In the granular xenoliths, the second generation olivine and spinel are re-equilibrated at higher temperature ranges of 1043 – 1167° C (Ferrando et al., 2008).

Samples from Nekempte were analyzed microscopically with a Nikon Eclipse E600 Polarized Light microscope. Images were acquired with an attachable Nikon Digital Sight DS-US camera and NIS Elements F software. Following Ferrando et al. (2008), the samples can be divided into two distinct suites of xenoliths: deformed and granular [Figure 4a-c]. In addition, a cumulate [Figure 4d] and dunite [Figure 4e] xenolith were examined.

4.1 Deformed xenoliths

Deformed spinel-bearing xenoliths [Figure 4a-b] are classified based on mineralogy, crystal size, amount of recrystallization, kink banding, and other textures present (e.g., fluid inclusion trails). In general, deformed xenoliths are harzburgite to dunite with large kinked crystals of olivine and orthopyroxene (1mm – 8mm).

4.1.1 Mineralogy

Deformed xenoliths contain two generations of olivine and orthopyroxene: coarse and fine-grained generations [Figure 5]. Other minerals, such as spinel, occur as smaller anhedral crystals and are not as abundant. Samples are on average 70% olivine, 28% orthopyroxene, 1% clinopyroxene, and <1% spinel. Coarse-grained olivine(Ol I) is characterized by larger (3mm – 8mm) sub-rounded, deformed, fractured crystals with undulatory extinction. It very commonly contains iddingsite and talc in its fractures. Fine-grained olivin (Ol II_D) is small (<1mm – 3mm) rounded, subhedral, undeformed crystals that occur at triple junctions of Ol I and Opx I.

Coarse-grained orthopyroxene(Opx I) is large (3mm – 5mm), sub-rounded, deformed crystals that are heavily fractured. Fine exsolution lamellae of Cpx I are widely distributed. Fine-grained (<1mm – 3mm) Orthopyroxene (Opx II_D) are less common but form in triple junctions with Ol and Opx I. Exsolution lamellae never eccur in Opx II_D. Spinel (Spl I) (<1– 2mm) is sparsely distributed and are always undeformed, anhedral, “holly leaf” shaped crystals that occur interstitially between Ol I and Opx I.

Clinopyroxene is present in very low abundances (~1%) in the deformed xenoliths, and is typically only 1– 3mm in size. Amphibole is not present in the deformed harzburgite xenoliths.

4.1.2 Textures

Deformed xenoliths exhibit little sign of recrystallization (i.e. small crystals, lack of kink banding). Large olivine and orthopyroxene crystals (3mm – 8mm) are surrounded by smaller second generation crystals; however, the second generation crystals are less abundant (only about 30% of the sample). Kink banding occurs in approximately 80% of the olivine of the deformed xenoliths. Kink banding seldom occurs in second generation olivine crystals. Orthopyroxene rarely display exsolution lamellae in first generation crystals; however, they often show a dissolution texture which appears as a "bearded" texture occurring at the rim of the mineral. Intragranular fluid inclusion trails [Figure 4f] occur in coarse-grained olivine and orthopyroxene.

4.2 Granular xenoliths

Granular spinel-bearing harzburgite xenoliths [Figure 4c] resemble deformed harxburgite xenoliths in that they also contain two generations of olivine and orthopyroxene: coarse and fine-grained generations [Figure 5]; However, the fine-grained generation is much more abundant. In general, granular xenoliths are distinguished by having more recrystallization indicated by the large amount of small (<1mm– 3mm) olivine and orthopyroxene crystals.

4.2.1 Mineralogy

Granular xenoliths are approximately 70 % Olivine, 26% Orthopyroxene, and 3% Spinel. Ol I (>3 mm) is present but less abundant than second generation olivine (Ol II_G) which fill the interstices between the first-generation crystals. Similarly, second-generation orthopyroxene (Opx II_G) is more common than Opx I and fills the interstitial spaces between Ol I and Opx I. There are two generations of spinel in the granular xenoliths: the first generation being "holly leaf" spinel (Spl I) and the second generation spinel

(Spl II_G) occurs as small rounded blebs approximately 1– 3mm in diameter. No clinopyroxene or amphibole are present in the granular xenoliths.

4.2.2 Textures

The granular xenoliths represent the most recrystallized xenolith from the sample suite; about 80% of the xenoliths contain recrystallized olivine and orthopyroxene. The recrystallized olivine ($OlII_G$) and orthopyroxene ($OpxII_G$) fill the interstitial spaces of the first generation crystals of Ol I_G and $OpxI_G$ and often form triple-junctions with other second generation crystals. The granular xenoliths display little to no kink banding in first generation crystals of olivine and orthopyroxene. Kink banding never occurs in second generation crystals. First generation olivine and orthopyroxene are often fractured and filled with secondary minerals (e.g., Iddingsite, Talc). Second generation crystals have minimal fracturing compared to the first generation crystals. Exsolution lamellae were not observed in the granular xenoliths. Fluid inclusion trails are common in granular xenoliths occurring in both first and second generation crystals.

4.3 Cumulate xenoliths

The cumulate xenolith [Figure 4d] is classified based on its classic cumulate texture. It has similar characteristics to the granular xenoliths; however, its abundance of subhedral crystals is what makes it unique from other xenolith types of this suite.

4.3.1 Mineralogy

The cumulate xenolith is comprised of approximately 80% olivine, 15% orthopyroxene, 3% clinopyroxene, and 2% spinel. Olivine (Ol_C) range from <1mm to ~4 mm in size and are euhedral to subhedral crystals. It is often zoned and fractured. Anhedral orthopyroxene (Opx_C) are <1mm – ~3mm in size and fill the interstices of the olivine crystals. Clinopyroxene (Cpx_C) are anhedral, and range from 1–2mm in size. Brown spinel is anhedral and often rounded and fractured. They range from <1mm – ~3mm in size. Minerals often meet at triple junctions.

4.3.2 Textures

The sample displays a cumulate texture in which euhedral to subhedral olivine crystals (Ol_C) have accumulated. Orthopyroxene (Opx_C), clinopyroxene (Cpx_C), and spinel (Spl_C) fill the interstices of the olivine crystals. The classic cumulate texture indicates a lack of recrystallization or replacive textures. There is no kink-banding in the cumulate xenoliths; however, some olivine crystals are moderately zoned. Clinopyroxene sometimes display weak exsolution lamellae. Mineral dissolution is common along the outer edges of clinopyroxenes throughout the sample. Exsolution lamellae are very sparsely distributed in the cumulate xenoliths. Fluid inclusion trails are very widespread in all mineral assemblages.

4.4 Dunite xenoliths

The dunite xenoliths [Figure 4e] display similar characteristics to those of the deformed xenoliths; however, due to their significant difference in mineralogy, they must be classified as their own group.

4.4.1 Mineralogy

Dunite xenoliths consist of 98% olivine and 2% spinel. Coarse grained olivine(Ol_{RD})is subrounded to anhedral and range from 1mm to 8mm in size and constitute approximately 80% of the sample. Olivine is often fractured and filled with secondary minerals such as iddingsite. Fine grain olivine is rare, anhedral, and is 1mm or less in size. Spinel(Spl_{RD}) are anhedral “holly leaf” spinel ranging from 1–3 mm. No orthopyroxene, clinopyroxene, or amphibole occur in the dunite xenoliths.

4.4.2 Textures

The dunite xenoliths contain very large (up to 8mm) kinked olivine constituting ~80% of the entire xenolith. Limited, if any, recrystallization textures (granularity) are present in the dunite xenoliths. Fluid inclusions are abundant in the dunite xenoliths and often occur in linear trails.

5. Results

5.1 Major, minor, and compatible element chemistry

Chemically, the data from the deformed xenoliths, granular xenoliths, and cumulate xenoliths plot in four distinct groups based on % Fo content in olivine, % En content in orthopyroxene, and Cr# in spinel. Mineral chemistry results are provided in Tables 2-5.

Major and minor element analysis for olivines reveals that the xenoliths plot in four distinct groups based on forsterite ranging from ~ 85% Fo to ~91% Fo (Figure 6). The deformed xenoliths have a forsterite content of approximately 89– 91 %. Selected element abundances include CaO (0.05– 0.15 weight percent), TiO_2 (0.004– 0.021 wt %), Al_2O_3 (0.016– 0.43 wt %), Ni (2500– 2900 ppm), Cr (~125– ~425 ppm), and Co (125– 145 ppm). The granular xenoliths have forsterite contents that range from ~88 – 90 %, CaO (0.03– 0.1 wt %), TiO_2 (0.025– 0.01 wt %), Al_2O_3 (0.015– 0.36 wt %), Ni (~2800–3100 ppm), Cr (~25– ~125 ppm), and Co (135– 155 ppm). The cumulate xenolith has a lower Fo content of 85– 86%, higher CaO (0.1– 0.3 wt %) and lower Ni (~1900 – 2600 ppm). TiO_2 ranges from 0.025– 0.02 wt %, Al_2O_3 (0.02– 0.37 wt %), Cr (~100– ~325ppm) and Co from 135– 170 ppm. The dunite xenolith has a forsterite content of approximately 86.5– 89 % Fo, CaO (0.049– 0.16 wt %), TiO_2 (0.0025–0.026), Al_2O_3 (0.014–0.24 wt %), Ni (2300– 2800 ppm), Cr (~60– ~110 ppm) and Co (142– 168 ppm).

Orthopyroxene mineral analyses reveal the same clustering based on % En, with ranges from 84% En to 90 % En (Figure 7). Deformed xenoliths have orthopyroxene compositions of approximately 88– 90 % enstatite, with ranges of CaO (0.79– 1.13 wt %), MnO (0.128– 0.139 wt %), Zn (31– 43 ppm), Sc (16.8– 21.9), Cr (4100– 5250 ppm), Co (54– 79 ppm), V (79– 92 ppm), and Ni (680– 820). Granular xenoliths have a pyroxene composition of approximately 88–89 % enstatite, with ranges of CaO (0.51– 0.74 wt %), MnO (0.133– 0.148 wt %), Zn (33– 38 ppm), Sc (14.1– 17.0 ppm), Cr (1500– 2200 ppm), Co (57– 68 ppm), V (89– 101 ppm), and Ni (720– 850 ppm). Cumulate xenoliths have an enstatite content of approximately 84.5–85.5 % enstatite. CaO ranges from 0.750– 0.910 wt %, MnO (0.180– 0.189 wt %),

Zn (46– 54 ppm), Sc (18.5– 21.9 ppm), Cr (2100– 2450 ppm), Co (59– 70 ppm), V (122– 133 ppm), and Ni (610– 680 ppm). Dunite xenoliths contained no orthopyroxene.

Spinel geochemical data were collected for the granular, cumulate and transitional xenoliths [Figure 8]. The analyzed deformed xenolith did not contain sufficient spinel for analysis. Spinel from the three xenoliths have variable chromium number (Cr/ (Cr+Al). Granular xenolith spinels have a Cr# of 0.271–0.334 with varying FeO (12.17–14.70 wt %, MgO (20.00– 22.92), TiO_2 (0.113– 0.147 wt %), MnO (0.088– 0.112), Sc (0.197– 0.968), V (375–489), Co (231–263), and Ni (3226– 4095). Cumulate xenoliths have a Cr# of 0.387– 0.421 and variances in FeO (16.27– 19.67 wt %), MgO (17.71– 19.50 wt %), TiO_2 (0.503– 0.824 wt %), MnO (0.113– 0.155 wt %), Sc (2.084– 3.248 ppm), V (725– 849 ppm), Co (189.1–212 ppm), and Ni (2365– 2922 ppm). Dunite xenoliths have a Cr# of 0.551– 0.588 and variances in FeO (15.73– 17.89 wt %), MgO (17.63– 23.18 wt %), TiO_2 (0.3541– 0.7586 wt %), MnO (0.111– 0.130 wt %), Sc (1.079– 3.230 ppm), V (680– 776 ppm), Co (226– 250 ppm), and Ni (2175– 2744 ppm).

5.2 Incompatible trace element chemistry

Trace elements were analyzed in olivine, orthopyroxene and clinopyroxene. Trace element abundances for olivines were below the detection limits of the LA-ICP-MS for most trace elements; therefore, they are not discussed. Trace elements in orthopyroxene reveal three distinct trace element signatures for the deformed, granular, and cumulate xenolith. Orthopyroxene (normalized to chondrite) (Figure 9a) in the deformed xenoliths is slightly more enriched in the LREE (i.e., La, Ce) and depleted in the HREEs (i.e., Er, Yb) when compared to the other two types of xenoliths. The orthopyroxene in the granular xenolith shows a significant depletion in the LREEs and enrichment in HREEs. The cumulate xenoliths have a similar REE pattern to the granular xenoliths although they are slightly more enriched in all of the REEs. Primitive-mantle normalized (Figure 9b) shows the orthopyroxene in the deformed xenolith as being enriched in Ce and Zr, and depleted in Y and Er compared to the other types of xenoliths. Zr/Hf_{PM} ratios (primitive-mantle normalized) of orthopyroxene in the deformed xenoliths range

from ~40 to 58, while orthopyroxene in all other xenoliths have Zr/Hf_{PM} ratios less than the chondritic value of approximately 34.2 (Weyer et al., 2003). Orthopyroxene in the granular and cumulate xenoliths are enriched in Dy, Y, and Er compared to the deformed xenoliths.

Clinopyroxene trace element data was collected from both the deformed and cumulate xenolith. Clinopyroxene was absent in the granular and transitional xenoliths. Clinopyroxene trace element analyses (normalized to chondrite) (Figure 10a), the cumulate xenoliths have a relatively flat REE pattern ranging from approximately ~10–20 ppm for all elements. The clinopyroxene in the deformed xenoliths are enriched in LREEs (i.e. La, Ce), though La and Ce behave differently, and are depleted in the HREEs (i.e. Dy, Er, and Yb).

6. Discussion

6.1 Location of samples within the SCLM

The SCLM records the complex interaction between pre-existing depleted peridotite and percolating melts/fluids over the lifetime of the lithosphere (e.g., Bodinier et al., 1990). These interactions result in significant modal and chemical heterogeneity that complicate the interpretation of xenolith suites. There is a growing consensus that chromatographic processes, which may result in the geochemical (Bedini et al., 1997) and modal (Pilet et al., 2011) stratification of the SCLM, play an important role in defining the petrographic and geochemical structure of the SCLM. At depth, metasomatic processes may generate pyroxenites within the SCLM; at mid-lithospheric depths, amphibole-rich lithologies are common; while at shallower lithospheric depths, widely disseminated metasomatic phases are evident (e.g., Pilet et al., 2011). Consequently, the interpretation of the geochemical characteristics of mantle xenoliths derived from the SCLM requires constraints as to their depth of formation/equilibration.

Where an aluminum-rich phase is present, the mantle xenolith suite from Nekempte exhibits spinel and lacks garnet, thereby limiting the depth of equilibration of these xenoliths to the spinel peridotite stability range. To more accurately quantify the depth of equilibration, we have applied the two pyroxene geothermobarometer of Putirka (2008). To ensure equilibrium between co-existing pyroxenes we only selected pyroxene pairs that have a K_D (Fe-Mg) value of between 0.95 and 1.23. Results of our thermo-barometric calculation show that the pressures and temperatures of equilibration are within a limited range between 1055 and 1114 °C, and 0.99 to 1.08 GPa [Table 6]. These pressure estimates suggest that the samples are derived from the shallowest portion of the lithospheric mantle, located just below the Moho [Figure 11].

Previous thermo-barometric studies of samples from Nekempte are limited (Conticelli et al., 1999), and are based on data from a single harzburgite sample (1.13 GPa, 1045^{o}C). The value is consistent with the results of the present study, and when combined with other xenolith localities in Ethiopia (Conticelli

et al., 1999; Roger et al., 1999; Rooney et al., 2005; Ferrando et al., 2007), requires a geotherm in the region that is significantly greater than the 40mWm^{-2} value expected for a steady state continental shield (e.g., Anderson, 2007). Previous studies have suggested that this elevated geotherm is the result of the Ethiopian SCLM undergoing recrystallization resulting from the thermal contributions from mantle plume(s) (e.g., Conticelli et al., 1999). The majority of regional xenolith samples support such a model; however, granular xenoliths from Injibara exhibit equilibration temperatures ~100^{o}C higher than deformed xenoliths at nominally similar pressures (Ferrando et al., 2007). These observations of significant thermal heterogeneity within a single region prompted Ferrando et al. (2007) to suggest a model whereby infiltration of melt associated with the Afar plume has perturbed the geothermal gradient of the Ethiopian SCLM. Maximum temperatures in the Nekempte xenoliths are observed in the cumulate xenoliths rather than the deformed xenoliths [Figure 11]; however, no thermobarometry calculations were performed for the granular xenoliths due to their inherent lack of clinopyroxene. A processed-based comparison is difficult due to our limited data; however, it is apparent that both the deformed and cumulate xenoliths measured from Nekempte have equilibrated at a temperature of about 100°C hotter than most of the xenoliths observed in other regional studies, but are equivalent to the temperatures observed in granular xenoliths from Nekempte (Conticelli etal., 1999) suggesting a similar thermal history.

6.2 Textural evidence of deformation

Suture zones and major structural lineaments are locales whereby shearing observed within the continental crust is also likely reflected in deformation of the SCLM. Along the Ethiopian rift, the YTVL, a Precambrian suture zone that reactivated and likely accommodated extension in the MER during the Cenozoic (Abebe et al., 1999; Keranen et al., 2008), is one of the most significant zones of lithospheric weakness in the region. Previous studies have shown the YTVL to be zone of significant crustal thinning (Keranen et al., 2008) and a region of focused Cenozoic volcanism (Abebe et al. 1999). Xenoliths from

Nekempte, which lies along the YTVL, thus have the potential to record deformation associated with the shearing of the lithosphere along this lineament.

The xenoliths analyzed from Nekempte exhibit evidence of dynamic recrystallization (e.g., Roger et al., 1999; Ferrando et al., 2008; Frezzotti et al., 2010). This process occurs where stress is applied to the SCLM, and the minerals accommodate the resulting strain by breaking down and rebuilding 'daughter' crystals in the interstitial spaces surrounding the 'parent' crystal. 'Parent' and 'daughter' generations were identified petrographically in deformed and granular xenoliths from Nekempte with the granular having undergone more dynamic recrystallization than deformed. These observations are similar to those of xenoliths from Injibara, described and classified by Ferrando et al., 2008. Ferrando and coworkers classified their xenoliths from Injibara into three groups: deformed, granular, and transitional. Deformed xenoliths are petrographically characterized by their larger (>3mm) crystal size and stress banding. Deformed xenoliths contain two generations of olivine and orthopyroxene, and one generation of clinopyroxene and spinel. Their overall larger grain size indicates a lack of significant recrystallization. Granular xenoliths are characterized by their smaller (<1–3mm) crystals and minimal stress banding. The granular samples contain two generations of olivine, orthopyroxene, clinopyroxene, and spinel. Transitional were described as samples having characteristics of both the deformed and granular types.

Following the classification scheme from Ferrando et al. (2008), the sample suite from Nekempte, contains both deformed and granular xenoliths [Figure 4a-c]. Deformed xenoliths contains two generations of olivine (>3mm), and orthopyroxene (>3mm), and one generation of spinel. The other deformed xenolith appears to be a dunite having 100% olivine and spinel. No clinopyroxene was present in the deformed xenoliths. The granular xenolith has two generations of olivine (<1–3mm), and orthopyroxene (<1–3mm), and one generation of sparsely distributed clinopyroxene and spinel. This sample suite presents some similar characteristics to the suite from Injibara; however, some differences must be noted. No transitional xenoliths were present in the Nekempte suite, and the fourth xenolith observed from Nekempte had a cumulate texture, indicated by euhedral to subhedral olivines with olivine

and orthopyroxene filling the interstices. The peridotite xenoliths from Injibara did not exhibit cumulate textures and consisted of only lherzolite and hartzburgite xenoliths; no dunite compositions were noted (Ferrando et al., 2008). Previous work has postulated that the level of recrystallization was positively correlated with the amount of interaction with plume derived melts (e.g., Roger et al, 1999; Ferrando et al., 2008; Frezzotti et al, 2010).

6.3 Evidence of metasomatic agents

The textural and thermobarometric evidence presented above suggest that the dominant mechanism of deformation within the Ethiopian SCLM is melt/fluid-rock interaction. The composition of these metasomatic agents remains less well constrained and requires a geochemical investigation of the phases within the xenoliths.

6.3.1 Evidence of hydrous metasomatism

Prior studies have suggested that a Cl-rich $H_2O - CO_2$ fluid was a pervasive metasomatic agent within the regional lithospheric mantle (Frezzotti et al., 2010). This conclusion is based upon data collected from amphibole and fluid inclusions in spinel lherzolites, which indicated that this modal metasomatic event occurred at around 1000° C, and interaction between CO_2 and H_2O - rich fluids and the deformed xenoliths may have caused the cryptic enrichment of Fe and Al in pyroxenes in addition to the growth of new amphibole (Frezzotti etal., 2010).

The origin of the suggested hydrous metasomatism event was be hypothesized to be associated with the earliest stages of mantle upwelling accompanying a rising plume (Frezzotti et al., 2010). The heterogeneity of the lithospheric mantle in East Africa suggests that the hydrous fluids generating the metasomatism percolated through the region via fracture migration, explaining the variation in both volatiles and LREE observed in the lithospheric mantle. Enrichment in Cl and water in mantle xenoliths is indicative of interaction with a recycled crust source (Frezzotti et al., 2010). This is also in agreement with enrichments in Pb, Ba, Th, U, and Sr within the hydrous metasomatic fluid phases (Frezzotti, et al.,

2010). These data suggest a source that was either rich in marine sediments contained in a subducting oceanic slab (a remnant of the Pan-African Orogeny) or a result of decarbonation or outgassing of hydro-saline melts at depth (Frezzotti et al., 2010). The origin of this hydrous metasomatism event remains uncertain, as isotopic evidence also points to the formation of amphibole cumulates at mid-lithosphere depths associated with the initial formation of the lithosphere during the Pan-African subduction and orogenic event (Rooney et al., 2014a). While regional evidence suggests that the lithosphere may have been broadly affected by this hydrous metasomatism process, xenoliths at Nekempte exhibit no evidence of hydrous modal metasomatism, requiring a different metasomatic agent.

6.3.2 Evidence of carbonatite metasomatism

The geochemical alteration of the continental lithospheric mantle by small-volume carbonate fluids has been noted by previous investigations of the SCLM (e.g., Rudnick et al., 1993); however, this work was undertaken in the southern East African Rift, where thicker continental lithosphere is predominant and carbonatite eruptions have been noted (e.g., Bell & Tilton, 2001). Within the northern East African Rift, carbonatites are absent and prior investigation of xenoliths has not suggested the influence of carbonatitric metasomatism. However, the absence of this signature from previous xenolith studies in the northern East African Rift might instead reflect an analytical bias towards in-situ analysis of clinopyroxene over orthopyroxene. Due to lower concentrations in incompatible elements, it is analytically challenging to measure trace element abundances within mantle orthopyroxenes, however, newer instrumentation now allows such analyses. In circumstances where complex modal metasomatism is apparent, different xenolith phases (such as opx) may reveal previously undetected complexity.

Orthopyroxene within the deformed xenoliths from Nekempte exhibit unusual trace element values, which may be characteristic of carbonatitic metasomatism [Figure 9a-b]. Elevated values of Zr/Hf in xenoliths and mantle-derived melts have been frequently linked with the influence of carbonatite metasomatism (e.g., Dupuy et al., 1992; Rudnick et al., 1993; Yaxley et al., 1998). Zr/ Hf ratios of a

carbonatitic metasomatic agent are thought to range from ~ 60– 80 (Ionov et al., 1993), elevated significantly over the chondritic value of ~34.2 (Weyer et al., 2003). Notably, orthopyroxenes from deformed xenoliths at Nekempte exhibit higher Zr/Hf ratios (40–58) when compared to the granular and other xenolith types in the suite (~20–45), and are suggestive of a carbonatite metasomatism event. Elsewhere in East Africa, carbonatite metasomatism is has been suggested in peridotite xenoliths from the Omari Cinder Cone (Tanzania), on the basis of a very high Zr/Hf ratio and significant LREE enrichment (Rudnick et al., 1993). The orthopyroxenes from the deformed Nekempte xenoliths exhibit a significant enrichment in LREE in comparison to the granular varieties [Figure 9a-b], consistent with a carbonatitic metasomatism model.

Similarly, clinopyroxene trace element data normalized to primitive mantle [Figure 10a-b] show elevated Zr/Hf ratios (~38– 39) [Figure 12] for the deformed xenoliths compared to the cumulate xenoliths (Zr/Hf= ~29– 35) further indicating a possible metasomatic enrichment that is carbonatitic in origin. Chazot et al. (1994) observed similar characteristic in spinel-bearing lherzolites from Yemen and indicated that the strong partitioning of Zr and Hf in amphibole and clinopyroxene in their xenoliths may indicate that their xenoliths recrystallized from a carbonatitic melt that interacted with an anhydrous lherzolite or harzburgite mantle.

6.3.3 Evidence of melt-lithosphere interaction

Previous studies have suggested that much of the deformation and rerystallization evident in xenoliths derived from the Ethiopian SCLM result from the interaction of silicate melts with the host peridotite (e.g., Roger et al., 1999; Ferrando et al., 2008). The model of Ferrando et al., (2008) suggests a two stage event whereby an initial hydrous metasomatic agent altered the SCLM and formed hydrous phases. The second metasomatic event in this model is caused by a melt which is 100°C warmer than the prior metasomatic agent. This second event promoted recrystallization of second generation crystals of olivine and pyroxenes and increase in Fe and Al, and decrease in Ni, Cr, and Cl. Similar chemistry in the first and

second generations of crystals in the granular xenoliths indicate nearly complete re-equilibration during the second cryptic metasomatic event. It is suggested that the physical and chemical variations in these xenoliths may have due to the localization of melts, the deformed xenoliths having been affected by a more uniform pervasive metasomatic event and the granular xenoliths having been impacted by local infiltration of melt.

An alternate model is presented by Bedini et al. (1997), who suggest that, rather than a dual-stage metasomatic event, a single-stage event that induced varying degrees of melt can explain both the physical and chemical variations in the xenoliths of the East African SCLM (in particular at Megga). This model suggests that the deformed xenoliths have been metasomatized with small melt fractions enriched in LILEs and depleted in HFSEs and the granular xenoliths have been metasomatized with large basaltic melt fractions. The metasomatic protolith, the SCLM prior to metasomatism, would have been heterogeneous to account for the mineralogical variations in the deformed xenoliths (i.e., both lherzolites and harzburgites are observed); however, deformed xenolith clinopyroxene trace element chemistry differs significantly, which Bedini et al. (1997) attributed to chromatographic effects connected to porous flow of small melt fractions where harzburgite will reach equilibrium much faster than lherzolite. In contrast, granular xenoliths are proposed to have interacted with large melt fractions of basaltic melts in order to explain the observed depletion in the LREEs. Granular xenoliths range from harzburgite to cpx-rich lherzolites, yet they still have a relatively uniform chemical composition. This signature is attributed to complete re-equilibration with a LREE-depleted melt – such as a basalt, with large melt/rock ratios associated with melt percolation at a higher porosity and/or over an extended period of time. Because the granular xenoliths contain relic porphyroclasts, it is suggested that the granular xenoliths may have formed at the expense of the deformed xenoliths. This is further indicated by the small variation in mineral chemistry of the granular xenoliths compared to the more heterogeneous mineral chemistry of the deformed facies.

Xenoliths from Nekempte exhibit similar features to those of Injibara and Megga. At all three localities, deformed xenoliths have been enriched by a metasomatic agent, although the composition of this agent differs from locality to locality: a Cl-rich H_2O- CO_2 fluid at Injibara; a LILE enriched/HFSE depleted small degree melt at Megga; and a LILE and HFSE enriched carbonatitic fluid at Nekempte. In contrast, the granular xenoliths at all three localities appear to be derived through the same process of significant melt-rock reaction. This process results in the strongly recrystallized granular xenoliths being depleted in the highly incompatible elements attributed to extensive re-equilibration with large volumes of basaltic melt. We examine this process in the context of melt focusing.

6.4 Evidence of focused melt transport

Reactivated structural lineaments such as the YTVL exhibit characteristics that facilitate the transport of melt from the asthenosphere into the lithosphere. It is suggested that the YTVL has aided in focused magmatic intrusion as evidenced by the extensive magmatism along its length over the past ~15 Ma (Abebe et al., 1998). In particular, shear pathways and topography of the lithosphere-asthenosphere boundary (Havlin et al., 2013; Rooney et al., 2014a) may result in the focusing of magma along structural lineaments. Such focused flow results in surface eruptions (e.g., Rooney et al., 2014a), but its passage through the lithosphere may have profound impacts on the SCLM where it may promote metasomatic alteration and recrystallization.

Havlin et al. (2013) indicates that shearing may influence diking and melt intrusion into the lithosphere by increasing porosity within the SCLM. Shear-induced porosity can result in porous zones or channels, which can serve as pathways for percolating magmas and fluids to interact with the SCLM, modifying its composition and other physical properties (Tomassi et al., 2004; Le Roux et al., 2007; Tomassi et al., 2008). It is suggested that these ‘channels’ are focused in ductile shear zones (deformed lithospheric mantle) (Kelemen et al., 1993; Whitehead & Kelemen, 1994) and focused flow in these shear

zones facilitates reactions dissolving clinopyroxene and precipitating olivine, ultimately resulting in a zone of precipitated dunite (Kelemen et al., 1992).

The xenoliths examined from Nekempte have a range in textural and geochemical characteristics that help constrain the model of focused melt flow and how it may operate in the Ethiopian SCLM. Based on both petrographic and chemical evidence, our current model incorporates both the textural characteristics and chemical characteristics of all four types of xenoliths: deformed, granular, cumulate, and replacement dunite, into a system that demonstrates the effects of a percolating fluid in a zone of ductile shearing [Figure 13]. Each type of xenolith plays a crucial role in explaining the dynamic system along the YTVL.

6.4.1 Pre-existing subcontinental lithospheric mantle: Deformed xenoliths

In our model, the deformed xenolith represents the initial state of the SCLM beneath the YTVL prior to being subjected to focused melt flow. Deformed xenoliths are characterized by their overall larger grain size (> 3mm) and stress banding. The large grain size along with stress banding suggests that they have undergone little recrystallization and therefore have been influenced less by stress or melt interaction. Additionally, deformed xenoliths have the highest Mg content (Fo= ~89–91, En= ~89–90) [Figure 6,7] suggesting perhaps a more depleted origin. High Zr/Hf ratios are observed in the deformed xenoliths, which we have suggested reflects carbonatite metasomatism (Rudnick et al., 1993; Weyer et al., 2003) [Figure 12]. This is not seen in the granular xenoliths, suggesting a later overprinting event that may have erased the earlier carbonatitic signature. These physical and chemical attributes combined suggest that the deformed xenoliths have undergone minimal chemical interaction with large volumes of melt and represent the “country rock” of the SCLM in the Ethiopian region.

6.4.2 Overprinted lithospheric mantle: Granular xenoliths

The granular xenolith in our model represents overprinted SCLM that was once similar in texture and chemistry to the deformed xenolith. Texturally, granular xenoliths are characterized by having overall smaller (<1–3mm) crystals and minimal to no stress banding suggesting recrystallization (Bedini et al.,

1997; Ferrando et al., 2008; Frezzotti et al., 2010; Roger et al., 2010). Recrystallization is further indicated by the decrease in magnesium content (Fo= ~87–89; En= ~88–89) (Ferrando et al., 2008) and depletion in LREE in orthopyroxene trace element chemistry[Figure 9, 10] which suggests a chemical interaction with large volumes of melt (Bedini et al., 1997). The granular xenolith was formed at the expense of the deformed xenolith lithology after being exposed to melt/ fluids generated from a porous melt channel adjacent to the xenolith.

6.4.3 Evidence of pervasive melt-lithosphere interaction: Replacement dunite xenoliths

The dunite xenolith discovered within the Nekempte suite is characterized by large olivine crystals (>3mm), the absence of pyroxene, and abundant spinel. Our initial hypothesis for the origin of this lithology was melt depletion of a peridotite during the initial stabilization of the regional lithosphere. On that basis, the dunite xenoliths would simply have experienced a greater degree of melt extraction in comparison to the deformed harzburgites. However, the geochemical characteristics of crystals within the xenoliths preclude this mode of origin. A melt-depletion model for the origin of this sample would result in residual olivine with elevated Fo content; however, our observations show that rather than being more enriched in Fo in comparison to the deformed harzburgite, the magnesium content was actually lower (Fo ~86–89). These data, when combined with low Ni content in olivine (~2300 – 2800 ppm) and high values of TiO_2 in spinel (~0.34– 0.75 wt%), and a lack of pyroxene, instead suggest this lithology may have formed by a replacement process (e.g., Suhr, 1999).

With Nekempte lying along a zone of lithospheric weakness, one must explore how deformation of the SCLM can affect the ease with which melt can influence the surrounding SCLM during melt localization and focusing. When a melt perturbs the shallow lithospheric mantle, the ascending melts will dissolve the pyroxene and precipitate olivine, forming zones or channels of ‘replacive dunite’ surrounded by harzburgite mantle (Kelemen & Dick, 1995). Channelized flow of melts in the SCLM can generate extreme variations in the more incompatible elements, even on small scales (1– 100m) (Speigelman &

Kelemen, 2003). This is consistent with data collected from orthopyroxene and clinopyroxene which both show extreme variation in the more incompatible trace elements [Figure 9, 10]. The presence of replacement dunite indicates significant melt-rock reaction has taken place within the SCLM (Spiegelman & Kelemen, 2003). The formation of replacement dunites, which lack the pyroxene phases, is useful for tracing the origin of other xenoliths at Nekempte, but can be challenging to adequately constrain. However, spinel provides some additional information and, in particular, Cr# in spinel can assist in further solidifying the case for focused melt transport. The dunite replacement xenoliths have an extremely high Cr# of ~0.6, much higher that the granular xenoliths (~0.3) and the cumulate xenoliths (~0.4) [Figure 8]. High Cr# in spinel of peridotites typically indicates a higher degree of partial melting of the peridotite (Hellebrand, 2001); however, because the replacement dunite was created at the expense of the orthopyroxene and clinopyroxene, it is plausible that the spinel was also created at the expense of the other minerals (i.e. olivine, pyroxene). High Cr# is observed in ophiolites at contacts between peridotites and pyroxenites and is suggested to be a consequence of dissolution of pyroxenes into a Cr-saturated magma (Bédard & Hébert, 1998). In other words, an exchange in Al and Cr can occur between pyroxene and spinel that will result in an increase in Cr# in spinel (Wilson, 1982). We suggest the high Cr# in the spinel of the replacement dunite xenoliths occurs as a result of the active dissolution of pyroxene during the chemical exchange between the melt channel and surrounding SCLM.

*6.4.4 Remnants of the metasomatic agent: Cumulate xenolith*s

The final type of xenolith presented in this study is the cumulates, which we suggest represent the remnant of the melt channel represented in the model. Texturally, these xenoliths are characterized by typical cumulate texture, which consists of subhedral olivine and orthopyroxene (<1– 3mm) crystals with interstitial anhedral pyroxenes. These xenoliths have the lowest magnesium content (Fo= ~84–86; En= ~85), more consistent with a melt composition. Additionally, igneous olivines have higher and more variable calcium concentrations and lower nickel concentrations (<2200 ppm) due to fractionation (Foley et al., 2013). Calcium concentrations in the olivine of the cumulate xenolith range from ~0.1–0.25 wt %

for CaO [Figure 6], much higher and more variable than the other xenoliths, and nickel concentrations for olivine in the cumulate xenolith are as low as 1900 ppm indicating its cumulate nature.

As melt percolates or flows through the lithosphere, it will fractionate as it slowly cools. As the melt cools, crystals will form and accumulate at the bottom of a magma body, forming a cumulate. The presence of a cumulate xenolith in the SCLM of Nekempte provides further evidence for a need for a model of channelized focused melt flow because a cumulate indicates a remnant of the melt channel itself where igneous processes are actively occurring.

The dynamism and heterogeneity of the East-African SCLM has often been explained in a more simplistic fashion involving models which are primarily driven by wide-spread metasomatism (e.g., Conticelli et al., 1999; Ferrando et al., 2008); however, speculation on channelized flow exists in current literature (Roger et al, 1999). It is suggested by some that these heterogeneities are primarily due to mechanisms and processes that are associated with a rising mantle plume (Bedini et al., 1997; Frezzotti et al., 2010) while other suggest theses heterogeneities of the SCLM are primarily driven by a Pan-African event (e.g. Kelemen et al, 1992; Havlin et al., 2013; Rooney et al, 2014a). While it is unclear which of these two mechanisms (if not both) have influenced the SCLM, it is apparent that a significant melt transport event has occurred along the YTVL. The origin of the unique lithologies of the YTVL may be plume-related, a result of reactivation of the YTVL, or a combination of the two. Isotopic data are needed to constrain the origin(s) of the large melt-fractions that strongly influence the physical and chemical properties of the SCLM.

7. Conclusions

The SCLM beneath the YTVL exhibits evidence of focused melt-lithosphere interaction. A close examination of the variety of xenoliths present at Nekempte demonstrate that melt beneath the YTVL (a reactivated Precambrian lineament) is strongly channelized. The xenoliths preserved within the Nekempte Suite reveal heterogeneous textures that range from deformed and granular lithologies through to replacement dunites and cumulates.

Similar to other xenolith suites examined in the region, Nekempte exhibits both granular and deformed xenolith varieties. However, we propose a new model that reconciles the presence of other xenolith lithological varieties that are difficult to explain by previously presented mechanisms.

We suggest that pervasive melt/rock reaction (also noted elsewhere within the Ethiopian plateau) was initiated by the interaction of basaltic melt with the SCLM resulting in wide-scale recrystallization and the formation of granular xenoliths. The depletion in LREE in orthopyroxene and the absence of clinopyroxene suggests that the mechanism of melt/rock reaction involved substantial flux of melt in order to scavenge the LREEs and destabilize clinopyroxene in the granular xenoliths. As this melt/rock reaction proceeded to completion, dunite xenoliths were formed at the expense of pyroxene. These replacement dunites are characterized by olivine with lower Mg# and spinel with very high Cr# (~0.6). Cumulate xenoliths evident in the Nekempte suite are hypothesized to represent fragments of metasomatizing basaltic melt.

We conclude that shearing associated with the YTVL has influenced the lithospheric mantle such that melt channeling is preferred over chromatographic metasomatism. This conclusion is consistent with previous studies suggesting an enhanced magma supply along the YTVL (Abebe et al., 1998). Conceptual numerical modeling and observations from the YTVL show that shear-induced porosity and melt focusing along steep topography of the lithosphere-asthenosphere boundary contribute to focused magma supply in the YTVL (Havlin et al., 2013; Rooney et al., 2014a). While previous studies have

shown that the crust along the YTVL is deformed during rifting (Keranen et al., 2008), our data suggests that deformation in the form of chemical alteration also extends into the lithospheric mantle. The mechanisms of deformation along structural lineaments is thus, in part, due to the influence of focused magmatic flow through the lithospheric mantle.

APPENDICES

APPENDIX A

TABLES

Table 1 Detection limits

	SiO_2	TiO_2	Al_2O_3	FeO	MnO	MgO	CaO	Na_2O	K_2O	Sc	V	Cr	Co	Ni	Cu	Zn	Ga
	wt %	wt %	wt %	wt %	wt %	wt %	wt %	wt %	wt %	ppm	ppm	ppm	ppm	ppm	ppm	ppm	ppm
Batch 1 (5-Dec-14)	0.300	0.000	0.003	0.002	0.000	0.150	0.150	0.001	0.001	0.200	0.100	0.800	0.040	0.500	0.040	0.200	0.030
Batch 2 (9-Dec-14)	0.150	0.000	0.001	0.000	0.000	0.007	0.150	0.001	0.001	0.200	0.030	0.050	0.020	0.150	0.050	0.200	0.030
Batch 3 (1-Apr-15)	1.000	0.000	0.001	0.002	0.000	0.015	0.007	0.020	0.007	0.300	0.040	0.400	0.060	0.700	0.200	0.600	0.080
Batch 4 (29-Apr-15)	0.400	0.000	0.007	0.003	0.000	0.002	0.005	0.003	0.002	0.100	0.100	3.000	0.030	0.150	0.050	0.200	0.070
Min Detection Limit	0.150	0.000	0.001	0.000	0.000	0.002	0.005	0.001	0.001	0.100	0.030	0.050	0.020	0.150	0.040	0.200	0.030

	Rb	Sr	Y	Zr	Nb	Ba	La	Ce	Nd	Sm	Eu	Gd	Dy	Er	Yb	Hf
	ppm	ppm	ppm	ppm	ppm	ppm	ppm	ppm	ppm	ppm	ppm	ppm	ppm	ppm	ppm	ppm
Batch 1 (5-Dec-14)	0.030	0.050	0.008	0.020	0.005	0.030	0.003	0.003	0.010	0.020	0.003	0.010	0.006	0.004	0.006	0.005
Batch 2 (9-Dec-14)	0.040	0.020	0.010	0.020	0.007	0.030	0.004	0.004	0.009	0.020	0.003	0.010	0.007	0.004	0.004	0.005
Batch 3 (1-Apr-15)	0.150	0.030	0.020	0.030	0.010	0.060	0.006	0.005	0.020	0.030	0.005	0.020	0.020	0.008	0.010	0.010
Batch 4 (29-Apr-15)	0.060	0.300	0.010	0.080	0.020	0.300	0.020	0.020	0.005	0.010	0.003	0.008	0.007	0.005	0.006	0.007
Min Detection Limit	0.030	0.020	0.008	0.020	0.005	0.030	0.003	0.003	0.005	0.010	0.003	0.008	0.006	0.004	0.004	0.005

Major and trace element detection limits. Detection limit is defined at three times standard deviation (1σ) on gas blank measurement. Any value less than the detection limit were omitted from the data.

Table 2 Olivine mineral chemistry

	Sample	SiO_2 wt%	TiO_2 wt %	Al_2O_3 wt%	$Cr2O_3$ wt %	FeO wt %	MnO wt %	MgO wt%	CaO wt%	Na_2O wt%	% Fo	Sc ppm	V ppm	Cr ppm	Co ppm	Ni ppm	Cu ppm	Zn ppm
Deformed	AB-OL1-1	42.04	0.007	0.017	0.021	9.321	0.133	48.41	0.064	0.010	90.05	2.555	3.927	140.46	139.52	2,725.16	2.733	57.06
	AB-OL1-2	41.63	0.005	0.029	0.022	9.420	0.131	48.72	0.056	0.010	90.05	2.596	3.373	151.68	138.82	2,786.00	2.350	44.66
	AB-OL1-3	41.08	0.009	0.044	0.023	9.709	0.136	48.89	0.078	0.054	89.76	2.933	3.783	159.98	139.12	2,929.08	3.217	44.63
	AB-OL1-4	41.69	0.007	0.026	0.021	9.445	0.136	48.61	0.075	0.013	89.95	3.143	4.418	146.35	135.52	2,893.90	2.722	46.70
	AB-OL1-5	41.39	0.006	0.037	0.023	9.916	0.138	48.43	0.072	0.012	89.48	3.344	3.963	154.02	141.10	2,905.67	2.629	53.54
	AB-OL1-6	41.21	0.006	0.028	0.023	9.560	0.130	48.99	0.070	0.010	89.93	3.318	3.200	157.97	140.93	2,847.89	1.719	51.10
	AB-OL1-7	40.89	0.006	0.025	0.023	9.317	0.131	49.55	0.064	0.017	90.26	2.699	3.388	155.16	136.65	2,801.91	1.834	53.29
	AB-OL1-8	41.23	0.006	0.024	0.023	9.606	0.139	48.92	0.065	0.010	89.87	2.944	4.104	160.52	134.19	2,729.62	1.955	59.82
	AB-OL1-9	40.89	0.004	0.019	0.024	9.136	0.129	49.75	0.063	0.011	90.46	2.936	3.983	161.53	137.38	2,770.51	1.566	58.07
	AB-OL1-10	41.05	0.006	0.016	0.025	9.345	0.132	49.38	0.065	0.010	90.20	3.245	4.243	168.88	134.26	2,810.54	1.825	58.06
	AB-OL2-1	40.85	0.006	0.046	0.024	9.144	0.131	49.74	0.064	0.011	90.45	2.561	3.958	162.70	134.45	2,757.67	2.256	59.87
	AB-OL2-2	41.43	0.007	0.108	0.023	9.367	0.131	48.84	0.083	0.015	90.06	3.194	3.837	156.45	137.21	2,816.86	2.391	56.58
	AB-OL2-3	40.72	0.006	0.030	0.024	9.257	0.134	49.78	0.067	0.013	90.35	2.967	4.333	166.80	135.15	2,809.95	1.886	57.02
	AB-OL2-4	41.35	0.005	0.028	0.024	9.099	0.131	49.31	0.062	0.012	90.42	2.523	3.899	163.55	136.20	2,758.30	2.139	60.30
	AB-OL2-5	40.89	0.007	0.068	0.024	9.228	0.134	49.59	0.071	0.014	90.34	3.278	4.082	163.32	135.76	2,771.29	2.102	58.85
	AB-OL3-1	41.12	0.006	0.088	0.033	9.088	0.129	49.42	0.095	0.031	90.41	3.490	5.870	227.29	132.18	2,675.26	2.772	58.50
	AB-OL3-2	41.49	0.008	0.079	0.030	8.977	0.131	49.19	0.097	0.017	90.47	3.128	5.933	206.68	130.87	2,716.54	2.182	59.87
	AB-OL3-3	41.31	0.008	0.030	0.039	8.965	0.128	49.46	0.091	0.013	90.54	4.164	6.131	268.79	130.13	2,719.04	1.516	60.08
	AB-OL3-4	40.86	0.007	0.033	0.033	9.366	0.131	49.49	0.097	0.013	90.16	3.165	5.121	222.91	134.70	2,741.02	2.113	59.57
	AB-OL3-5	40.91	0.007	0.034	0.035	9.118	0.133	49.70	0.085	0.013	90.44	3.010	6.085	237.39	134.69	2,758.12	1.728	61.91
	AB-OL4-1	41.31	0.007	0.048	0.044	9.075	0.133	49.32	0.085	0.014	90.42	3.757	6.276	298.21	133.08	2,665.62	1.765	61.54
	AB-OL4-2	40.49	0.007	0.025	0.028	9.318	0.132	49.94	0.070	0.013	90.32	3.858	4.828	194.04	141.19	2,713.28	1.590	60.96
	AB-OL4-3	41.22	0.008	0.097	0.030	9.247	0.133	49.18	0.088	0.018	90.23	3.168	4.749	205.90	135.25	2,665.84	1.979	58.48
	AB-OL4-4	41.54	0.009	0.209	0.047	8.927	0.134	49.00	0.116	0.028	90.46	3.585	6.361	318.34	139.78	2,665.65	2.399	57.15
	AB-OL4-5	40.70	0.007	0.076	0.027	9.245	0.131	49.74	0.073	0.016	90.35	2.879	4.469	182.36	185.80	2,697.06	2.194	61.95
	AB-OL5-1	41.17	0.018	0.436	0.054	9.284	0.144	48.58	0.139	0.104	90.01	4.817	8.917	369.15	126.10	2,513.29	10.99	58.39
	AB-OL5-2	41.57	0.014	0.212	0.061	9.062	0.139	48.81	0.118	0.042	90.29	4.720	9.469	416.82	129.64	2,607.77	7.557	63.41
	AB-OL5-3	41.36	0.021	0.307	0.044	9.299	0.142	48.54	0.136	0.087	90.00	3.548	7.512	300.66	129.14	2,522.05	39.34	60.44
	AB-OL5-4	41.23	0.013	0.227	0.040	9.251	0.142	48.89	0.126	0.067	90.12	4.034	6.877	274.85	132.01	2,651.99	8.832	61.36
	AB-OL5-5	41.33	0.011	0.331	0.043	9.195	0.141	48.74	0.134	0.055	90.14	3.980	8.140	293.27	128.22	2,627.62	11.67	55.62
	AB-OL6-1	40.92	0.006	0.017	0.023	9.052	0.131	49.80	0.058	0.009	90.56	2.837	3.411	157.09	134.55	2,699.11	1.138	59.78
	AB-OL6-2	40.98	0.006	0.018	0.023	9.049	0.130	49.75	0.060	0.009	90.55	2.833	3.499	159.25	135.26	2,723.93	1.316	59.13
	AB-OL6-3	40.78	0.006	0.024	0.023	8.878	0.128	50.11	0.062	0.010	90.77	2.737	3.528	157.69	130.35	2,679.54	1.332	56.75
	AB-OL6-4	41.27	0.005	0.018	0.023	8.947	0.130	49.55	0.063	0.009	90.60	2.925	3.602	158.11	129.54	2,687.52	1.253	56.89
	AB-OL6-5	41.75	0.007	0.021	0.023	9.070	0.129	48.95	0.061	0.009	90.39	2.479	3.534	157.79	132.43	2,722.09	1.546	57.26
	AB-OL6-6	40.78	0.006	0.036	0.023	9.211	0.130	49.75	0.066	0.014	90.39	3.058	3.761	160.63	133.71	2,723.31	1.362	59.92
	AB-OL6-7	41.06	0.006	0.018	0.024	9.142	0.130	49.57	0.066	0.009	90.42	2.738	3.461	160.87	131.23	2,724.71	1.145	57.41
	AB-OL6-8	41.13	0.006	0.021	0.024	9.266	0.130	49.38	0.060	0.010	90.28	3.140	3.838	163.29	134.23	2,736.40	1.312	61.11
	AB-OL6-9	40.58	0.007	0.019	0.023	9.113	0.131	50.08	0.063	0.009	90.54	2.658	3.727	157.24	131.48	2,690.05	1.358	58.48
	AB-OL6-10	41.16	0.007	0.021	0.023	9.190	0.130	49.42	0.062	0.009	90.36	2.606	3.538	157.97	132.63	2,684.80	1.318	57.92
	AB-OL7-1	40.50	0.006	0.019	0.029	9.117	0.132	50.14	0.073	0.012	90.54	3.097	5.338	199.81	133.00	2,671.77	1.482	60.72
	AB-OL7-2	41.03	0.005	0.016	0.027	9.078	0.133	49.65	0.073	0.012	90.49	3.006	4.789	185.07	133.37	2,724.45	1.594	61.38
	AB-OL7-3	40.91	0.005	0.014	0.028	9.142	0.131	49.72	0.068	0.012	90.45	3.317	5.158	192.36	134.63	2,733.84	1.718	61.89
	AB-OL7-4	40.78	0.005	0.016	0.027	9.018	0.130	49.96	0.079	0.012	90.59	3.374	4.772	182.47	135.19	2,718.24	1.633	62.08
	AB-OL7-5	41.38	0.011	0.167	0.030	9.992	0.145	48.14	0.121	0.025	89.29	3.003	5.976	202.75	133.42	2,578.50	3.411	64.25
	AB-OL8-1	40.59	0.005	0.022	0.024	9.151	0.130	50.03	0.065	0.010	90.50	2.858	3.578	160.82	131.94	2,657.72	1.253	59.97
	AB-OL8-2	41.26	0.005	0.021	0.024	9.348	0.132	49.17	0.058	0.010	90.17	2.983	3.673	166.75	135.61	2,733.97	1.218	60.29
	AB-OL8-3	40.49	0.006	0.020	0.023	8.988	0.127	50.29	0.062	0.010	90.70	3.164	3.440	157.06	133.14	2,717.61	1.411	61.38
	AB-OL8-4	40.54	0.006	0.004	0.024	9.292	0.133	49.96	0.055	0.007	90.36	2.990	3.109	163.38	135.12	2,754.35	1.383	62.33
	AB-OL8-5	40.90	0.006	0.018	0.024	9.129	0.133	49.74	0.064	0.010	90.47	2.744	3.305	160.88	130.92	2,674.31	1.266	59.06
	AB-OL8-6	40.75	0.007	0.017	0.023	9.023	0.132	50.00	0.058	0.010	90.61	3.243	3.742	158.14	134.69	2,692.78	1.491	60.32
	AB-OL8-7	41.11	0.006	0.015	0.023	8.908	0.127	49.76	0.063	0.010	90.68	2.969	3.540	157.98	132.56	2,727.42	1.299	59.72
	AB-OL8-8	40.79	0.006	0.016	0.024	9.166	0.132	49.82	0.062	0.010	90.45	2.717	3.637	162.70	131.56	2,728.18	1.346	60.57
	AB-OL8-9	40.97	0.005	0.018	0.023	8.938	0.130	49.87	0.059	0.010	90.67	3.066	3.233	156.53	132.30	2,752.27	1.457	59.47
	AB-OL8-10	40.58	0.006	0.029	0.024	8.937	0.131	50.24	0.065	0.009	90.73	2.411	3.539	160.98	131.66	2,756.73	1.171	60.98
	AB-OL9-1	40.66	0.005	0.018	0.023	9.012	0.130	50.10	0.066	0.010	90.64	2.363	3.329	159.84	132.81	2,794.26	1.802	60.19
	AB-OL9-2	41.28	0.005	0.044	0.023	9.349	0.131	49.11	0.068	0.011	90.15	2.788	3.224	159.46	136.29	2,766.29	1.975	65.47
	AB-OL9-3	40.72	0.006	0.023	0.023	9.210	0.132	49.84	0.057	0.010	90.42	2.886	3.584	157.83	134.66	2,859.78	1.444	61.96
	AB-OL9-4	40.61	0.005	0.019	0.023	9.187	0.131	49.97	0.062	0.010	90.46	2.733	3.427	160.59	136.06	2,823.51	1.774	60.19
	AB-OL9-5	40.83	0.006	0.018	0.022	9.514	0.134	49.42	0.068	0.013	90.05	2.617	3.632	148.85	137.29	2,813.26	1.620	65.50
	AB-OL9-6	40.88	0.006	0.019	0.021	9.065	0.131	49.83	0.060	0.010	90.55	2.703	3.766	142.76	137.23	2,787.77	1.500	61.99
	AB-OL9-7	40.71	0.005	0.022	0.023	9.315	0.133	49.74	0.061	0.011	90.30	2.477	3.515	156.84	135.43	2,705.50	1.284	68.21
	AB-OL9-8	40.25	0.006	0.017	0.019	11.01	0.163	48.45	0.085	0.011	88.44	2.912	3.876	129.22	136.41	2,557.10	2.361	86.44
	AB-OL9-9	39.98	0.008	0.026	0.022	11.33	0.165	48.38	0.092	0.014	88.13	3.183	3.680	150.42	135.29	2,559.42	2.944	85.60
	AB-OL9-10	40.88	0.005	0.018	0.023	9.054	0.129	49.84	0.065	0.009	90.55	2.269	3.239	159.89	133.52	2,743.38	1.747	60.63
	AB-OL10-1	40.08	0.006	0.040	0.023	11.30	0.159	48.29	0.100	0.015	88.13	3.208	3.991	160.53	134.60	2,665.61	2.723	82.98
	AB-OL10-2	40.85	0.007	0.264	0.023	12.85	0.161	45.46	0.132	0.043	86.01	3.387	4.547	159.27	129.78	2,454.23	4.091	83.61
	AB-OL10-3	40.50	0.006	0.021	0.023	10.63	0.151	48.60	0.082	0.013	88.84	3.333	4.030	158.19	136.23	2,685.00	2.566	79.70
	AB-OL10-4	40.23	0.006	0.021	0.021	11.40	0.159	48.10	0.077	0.013	88.03	3.057	4.143	144.06	140.22	2,637.79	2.583	85.81
	AB-OL10-5	39.75	0.008	0.025	0.023	11.81	0.169	48.12	0.106	0.014	87.62	3.344	4.771	159.72	138.48	2,586.22	2.347	85.23
	AB-OL11-1	40.18	0.006	0.019	0.022	12.98	0.195	46.49	0.115	0.012	86.15	3.068	3.263	151.33	145.10	2,334.40	2.761	104.69
	AB-OL11-2	40.31	0.006	0.022	0.027	10.79	0.155	48.62	0.084	0.014	88.69	3.246	3.486	183.80	138.31	2,663.60	2.880	88.92
	AB-OL11-3	40.60	0.005	0.019	0.026	10.60	0.154	48.53	0.084	0.012	88.85	3.074	3.946	177.04	135.02	2,712.70	2.578	89.04
	AB-OL11-4	40.49	0.007	0.083	0.023	11.05	0.166	48.07	0.105	0.019	88.30	3.031	4.355	157.73	134.22	2,651.29	2.685	87.37
	AB-OL11-5	40.60	0.004	0.021	0.024	10.99	0.161	48.11	0.098	0.015	88.37	3.220	3.761	162.72	132.22	2,492.74	2.866	84.74
Granular	BX-OL1-1	40.98	0.003	0.017	0.006	10.38	0.145	48.41	0.056	0.007	89.07	1.986	2.635	43.41	146.23	2,940.80	1.364	55.74
	BX-OL1-2	40.59	0.004	0.018	0.006	10.13	0.141	49.05	0.055	0.007	89.42	1.950	2.667	43.77	142.61	2,869.71	1.179	57.35
	BX-OL1-3	40.91	0.003	0.018	0.006	10.37	0.145	48.49	0.052	0.007	89.09	1.752	2.574	43.76	148.90	2,967.81	1.182	52.94
	BX-OL1-4	40.57	0.004	0.018	0.006	10.43	0.146	48.77	0.046	0.007	89.10	1.963	2.521	43.44	146.83	2,920.22	1.245	55.32
	BX-OL1-5	40.64	0.004	0.020	0.006	10.25	0.143	48.88	0.057	0.006	89.27	1.847	2.581	43.12	142.90	2,923.01	1.230	53.29
	BX-OL1-6	41.05	0.003	0.018	0.006	10.60	0.142	48.14	0.048	0.008	88.82	1.720	2.551	43.98	144.01	2,918.14	1.284	55.89
	BX-OL1-7	40.71	0.003	0.020	0.006	10.36	0.145	48.70	0.049	0.007	89.14	1.998	2.677	42.94	145.85	2,960.68	1.302	52.98
	BX-OL1-8	41.02	0.005	0.017	0.006	10.35	0.146	48.40	0.051	0.007	89.09	2.277	2.905	43.25	146.54	2,969.11	1.205	54.85
	BX-OL1-9	40.77	0.004	0.019	0.006	10.32	0.143	48.68	0.056	0.007	89.17	2.257	2.697	43.29	146.68	2,945.14	1.222	54.45
	BX-OL1-10	40.61	0.003	0.020	0.006	10.26	0.143	48.91	0.051	0.007	89.27	2.302	2.673	42.80	145.35	2,918.70	1.184	55.65
	BX-OL2-1	40.79	0.003	0.017	0.006	10.45	0.146	48.52	0.060	0.009	89.01	1.850	3.341	43.31	145.71	2,956.11	1.585	53.82
	BX-OL2-2	40.74	0.003	0.015	0.006	10.49	0.143	48.54	0.064	0.008	88.98	1.904	2.736	41.16	145.28	2,850.67	1.484	52.76
	BX-OL2-3	40.79	0.003	0.016	0.006	10.47	0.143	48.52	0.049	0.007	89.01	2.022	3.309	43.76	149.87	2,971.18	1.515	54.35
	BX-OL2-4	40.93	0.003	0.015	0.006	10.62	0.146	48.22	0.055	0.007	88.80	1.842	2.786	42.70	152.93	3,023.70	1.525	54.00
	BX-OL2-5	40.66	0.003	0.019	0.006	10.41	0.147	48.71	0.051	0.007	89.10	2.401	3.102	43.43	149.10	2,908.85	1.693	52.74

Major and trace elements concentrations for olivine in xenoliths from Nekempte, Ethopia.

-- = Not Analyzed

Table 2 (cont'd)

	Sample	SiO_2 wt%	TiO_2 wt %	Al_2O_3 wt%	$Cr2O_3$ wt %	FeO wt %	MnO wt %	MgO wt%	CaO wt%	Na_2O wt%	% Fo	Sc ppm	V ppm	Cr ppm	Co ppm	Ni ppm	Cu ppm	Zn ppm
Granular	BX-OL2-6	40.30	0.004	0.018	0.007	10.61	0.149	48.86	0.054	0.008	88.94	2.110	2.759	46.21	147.94	2,958.69	1.801	51.93
	BX-OL2-7	40.74	0.003	0.024	0.006	10.27	0.142	48.76	0.056	0.008	89.24	2.081	2.548	42.03	143.99	2,896.19	1.855	51.81
	BX-OL2-8	41.04	0.003	0.019	0.006	10.33	0.144	48.40	0.049	0.008	89.11	1.646	2.777	43.38	145.00	2,952.29	1.502	52.75
	BX-OL2-9	40.05	0.004	0.019	0.007	12.12	0.158	47.58	0.060	0.010	87.28	2.090	2.712	47.27	147.98	2,610.49	2.216	77.30
	BX-OL2-10	40.71	0.003	0.021	0.006	10.46	0.146	48.59	0.051	0.008	89.03	1.717	3.013	42.25	145.99	2,966.62	1.664	50.06
	BX-OL3-1	41.20	0.006	0.121	0.007	10.68	0.144	47.74	0.066	0.023	88.63	2.118	6.224	51.04	147.34	2,936.03	0.578	57.27
	BX-OL3-2	40.95	0.004	0.091	0.007	10.53	0.151	48.19	0.060	0.018	88.87	1.956	4.225	47.38	147.27	2,986.33	0.604	58.05
	BX-OL3-3	41.02	0.004	0.061	0.007	10.36	0.146	48.34	0.051	0.015	89.07	2.083	3.467	47.59	144.14	2,911.68	0.671	53.44
	BX-OL3-4	40.91	0.003	0.019	0.008	10.64	0.144	48.21	0.057	0.010	88.78	1.764	3.408	56.45	147.53	3,029.63	0.808	60.14
	BX-OL3-5	40.75	0.003	0.017	0.007	10.58	0.146	48.44	0.052	0.008	88.89	1.805	3.153	49.87	150.33	3,048.93	0.639	58.51
	BX-OL4-1	40.31	0.004	0.022	0.013	10.40	0.147	49.05	0.061	0.009	89.16	2.586	5.141	89.05	145.58	2,923.13	1.055	53.73
	BX-OL4-2	40.89	0.007	0.159	0.015	10.50	0.144	48.21	0.073	0.013	88.89	2.363	6.263	102.91	146.89	2,874.86	0.988	53.38
	BX-OL4-3	41.06	0.006	0.136	0.013	10.15	0.141	48.42	0.070	0.013	89.26	2.320	7.793	88.54	142.10	2,946.99	1.091	54.71
	BX-OL4-4	41.06	0.009	0.129	0.062	10.25	0.156	48.28	0.085	0.019	89.11	3.888	11.58	420.93	135.38	2,611.34	2.429	50.40
	BX-OL4-5	40.66	0.005	0.051	0.034	10.00	0.145	49.04	0.070	0.016	89.52	3.781	13.45	234.43	139.32	2,893.07	1.593	52.52
	BX-OL5-1	41.01	0.003	0.018	0.006	10.24	0.143	48.53	0.051	0.007	89.22	1.890	2.757	42.55	145.47	2,917.14	1.574	58.10
	BX-OL5-2	40.65	0.003	0.020	0.006	10.45	0.147	48.66	0.053	0.008	89.04	2.064	2.670	43.26	147.00	2,945.46	1.563	52.99
	BX-OL5-3	40.43	0.004	0.018	0.006	10.63	0.147	48.71	0.056	0.007	88.89	2.017	2.610	43.49	146.36	3,005.65	1.415	51.30
	BX-OL5-4	40.69	0.003	0.018	0.006	10.39	0.143	48.70	0.049	0.007	89.12	1.920	2.734	41.96	144.23	2,972.48	1.260	53.00
	BX-OL5-5	41.13	0.004	0.017	0.006	10.46	0.141	48.18	0.054	0.009	88.94	2.177	2.837	44.06	144.42	2,927.42	1.783	55.13
	BX-OL5-6	41.53	0.004	0.018	0.006	10.26	0.142	48.00	0.049	0.007	89.10	1.768	2.947	44.22	141.20	2,967.23	1.369	52.57
	BX-OL5-7	40.65	0.003	0.019	0.006	10.62	0.145	48.52	0.043	0.007	88.88	2.378	2.633	43.50	149.01	3,003.57	1.570	55.46
	BX-OL5-8	41.20	0.003	0.018	0.006	10.26	0.142	48.31	0.054	0.007	89.15	2.180	2.741	42.96	145.61	2,967.84	1.295	52.69
	BX-OL5-9	40.41	0.003	0.016	0.008	12.07	0.165	47.25	0.071	0.011	87.23	2.238	2.963	52.22	149.90	2,786.15	1.861	81.68
	BX-OL5-10	40.31	0.003	0.020	0.006	10.15	0.141	49.32	0.051	0.008	89.47	1.670	2.739	44.43	144.88	2,885.44	1.536	53.92
	BX-OL6-1	41.14	0.003	0.017	0.006	10.39	0.144	48.24	0.055	0.009	89.02	1.823	3.435	44.32	149.71	2,944.38	0.797	51.18
	BX-OL6-2	40.86	0.004	0.018	0.006	10.48	0.146	48.44	0.047	0.007	88.99	2.180	2.601	41.83	150.14	3,015.83	1.140	53.28
	BX-OL6-3	40.71	0.004	0.019	0.006	10.21	0.139	48.86	0.053	0.007	89.32	2.208	2.525	40.95	145.62	2,954.09	1.342	49.82
	BX-OL6-4	40.93	0.004	0.019	0.006	10.47	0.145	48.38	0.053	0.007	88.98	1.968	2.610	44.45	148.41	2,998.83	1.411	54.47
	BX-OL6-5	40.57	0.003	0.020	0.007	10.40	0.144	48.80	0.055	0.007	89.12	1.992	2.611	45.91	147.22	3,008.58	1.452	54.13
	BX-OL6-6	40.79	0.003	0.020	0.006	10.36	0.144	48.63	0.056	0.008	89.13	1.996	2.562	43.52	145.99	2,985.41	1.485	53.58
	BX-OL6-7	41.24	0.003	0.017	0.006	10.25	0.142	48.29	0.051	0.007	89.17	2.381	2.866	42.12	147.70	2,998.82	1.297	53.20
	BX-OL6-8	41.33	0.003	0.021	0.006	10.26	0.142	48.18	0.060	0.007	89.13	2.206	2.748	44.13	144.65	2,961.78	1.422	53.70
	BX-OL6-9	41.07	0.004	0.018	0.007	10.31	0.141	48.40	0.050	0.007	89.14	1.590	2.877	44.54	142.83	2,951.09	1.763	58.04
	BX-OL6-10	40.92	0.003	0.018	0.007	10.28	0.141	48.58	0.059	0.009	89.19	2.154	3.226	48.02	147.61	3,014.42	1.463	57.00
	BX-OL7-1	41.06	0.007	0.160	0.013	10.38	0.145	48.15	0.079	0.019	88.98	2.708	6.063	88.72	146.26	3,010.07	0.685	53.76
	BX-OL7-2	40.73	0.005	0.039	0.011	10.25	0.146	48.74	0.075	0.014	89.22	3.296	5.462	72.61	140.92	2,948.61	0.686	52.68
	BX-OL7-3	40.87	0.004	0.025	0.007	10.39	0.147	48.49	0.061	0.010	89.06	2.261	3.441	48.28	147.77	2,980.57	0.773	53.47
	BX-OL7-4	40.48	0.005	0.300	0.010	10.58	0.147	48.34	0.077	0.047	88.83	1.700	4.707	68.05	141.82	3,050.81	0.970	58.79
	BX-OL7-5	41.72	0.010	0.380	0.015	10.51	0.148	47.05	0.108	0.052	88.60	2.885	6.108	104.35	145.24	2,946.81	0.770	55.78
	BX-OL8-1	41.00	0.003	0.018	0.006	10.34	0.142	48.45	0.050	0.007	89.12	1.890	2.412	44.40	147.78	3,029.68	1.241	54.51
	BX-OL8-2	41.43	0.004	0.017	0.006	10.35	0.143	47.99	0.053	0.007	89.01	1.884	2.619	43.39	146.49	3,015.24	1.245	53.56
	BX-OL8-3	41.05	0.004	0.018	0.006	10.31	0.145	48.41	0.051	0.006	89.13	2.424	2.648	43.16	148.26	2,972.01	1.363	54.58
	BX-OL8-4	40.83	0.003	0.019	0.006	9.977	0.141	48.96	0.057	0.008	89.54	2.087	2.452	44.05	142.99	2,963.36	1.361	53.67
	BX-OL8-5	41.06	0.003	0.019	0.006	10.30	0.143	48.42	0.053	0.007	89.14	2.112	2.683	43.16	148.52	3,031.15	1.164	51.20
	BX-OL8-6	41.40	0.003	0.021	0.006	10.12	0.140	48.26	0.053	0.007	89.28	1.657	2.621	43.07	144.84	2,915.61	1.180	55.41
	BX-OL8-7	40.88	0.003	0.019	0.006	10.25	0.144	48.64	0.055	0.008	89.23	1.989	2.783	43.28	147.58	3,041.52	1.151	54.23
	BX-OL8-8	41.68	0.003	0.020	0.006	10.13	0.141	47.97	0.049	0.007	89.22	1.718	2.647	43.38	143.79	2,972.02	1.376	53.32
	BX-OL8-9	40.58	0.003	0.020	0.006	10.41	0.146	48.78	0.053	0.006	89.11	1.858	2.571	43.97	147.09	3,004.50	1.280	51.98
	BX-OL8-10	40.92	0.003	0.018	0.006	10.68	0.146	48.18	0.053	0.008	88.74	2.167	2.662	43.49	147.75	3,055.39	1.374	51.96
Cumulate	AU-OL1-1	40.64	0.008	0.071	0.035	13.34	0.190	45.51	0.224	0.016	85.45	5.256	8.049	241.77	159.27	2,253.15	2.805	91.31
	AU-OL1-2	39.50	0.009	0.084	0.034	13.65	0.184	46.33	0.224	0.019	85.40	5.013	7.662	231.47	158.16	2,308.66	2.390	89.90
	AU-OL1-3	40.94	0.009	0.113	0.037	13.41	0.184	45.11	0.210	0.017	85.29	5.686	9.427	256.02	154.47	2,307.59	4.714	92.55
	AU-OL1-4	40.96	0.007	0.140	0.030	13.17	0.184	45.30	0.205	0.024	85.57	4.029	6.812	204.07	156.78	2,275.43	3.020	87.77
	AU-OL1-5	39.60	0.005	0.049	0.031	13.45	0.178	46.51	0.194	0.016	85.66	5.168	6.678	211.17	153.44	2,315.75	2.857	87.95
	AU-OL2-1	40.04	0.008	0.185	0.028	13.65	0.188	45.64	0.244	0.026	85.19	5.188	6.285	189.34	160.40	2,121.60	2.557	89.81
	AU-OL2-2	40.26	0.004	0.023	0.029	13.49	0.184	45.80	0.220	0.015	85.40	4.563	5.992	195.31	159.14	2,124.95	1.999	88.28
	AU-OL2-3	40.28	0.005	0.032	0.026	13.49	0.195	45.75	0.231	0.021	85.36	5.371	6.450	175.51	158.07	2,073.53	2.035	91.77
	AU-OL2-4	39.77	0.004	0.026	0.027	13.43	0.190	46.36	0.207	0.018	85.62	4.300	6.681	187.72	161.04	2,073.16	2.001	89.95
	AU-OL2-5	39.43	0.005	0.028	0.027	13.32	0.184	46.81	0.212	0.014	85.83	4.785	5.962	183.21	160.84	2,034.67	1.925	92.59
	AU-OL3-1	39.27	0.008	0.049	0.034	13.60	0.189	46.65	0.204	0.029	85.55	5.800	9.479	233.10	160.78	1,979.70	1.445	97.07
	AU-OL3-2	40.25	0.008	0.051	0.036	13.35	0.185	45.92	0.217	0.014	85.56	5.720	9.558	243.57	160.37	1,996.89	1.896	93.40
	AU-OL3-3	40.19	0.008	0.086	0.036	13.55	0.179	45.76	0.199	0.020	85.36	6.180	9.149	244.29	157.77	1,956.91	1.680	84.61
	AU-OL3-4	39.92	0.005	0.029	0.028	13.08	0.182	46.56	0.202	0.016	85.99	4.749	6.681	191.24	159.51	2,029.23	1.681	90.87
	AU-OL3-5	40.03	0.005	0.036	0.028	13.08	0.174	46.47	0.191	0.016	85.98	4.946	6.732	189.73	156.59	1,987.91	1.876	91.79
	AU-OL4-1	40.11	0.005	0.031	0.029	13.15	0.179	46.32	0.190	0.016	85.88	4.502	6.983	196.61	158.28	1,923.00	1.277	92.69
	AU-OL4-2	40.18	0.009	0.173	0.027	13.13	0.183	46.06	0.236	0.025	85.78	4.664	8.299	186.42	153.97	1,916.96	1.637	86.89
	AU-OL4-3	39.77	0.004	0.031	0.027	13.35	0.184	46.46	0.193	0.014	85.74	4.618	7.509	186.36	163.72	2,010.98	1.687	93.03
	AU-OL4-4	40.19	0.012	0.105	0.025	13.88	0.203	45.34	0.231	0.032	84.89	4.828	8.914	170.81	164.76	2,042.34	2.849	92.92
	AU-OL4-5	40.12	0.006	0.056	0.026	13.57	0.181	45.83	0.207	0.017	85.35	4.716	8.015	174.82	159.79	2,009.15	1.551	90.84
	AU-OL5-1	39.97	0.005	0.042	0.026	13.12	0.179	46.48	0.189	0.015	85.96	5.310	6.904	178.46	159.57	1,954.46	2.562	94.47
	AU-OL5-2	40.08	0.004	0.031	0.026	12.93	0.177	46.58	0.194	0.014	86.14	4.817	6.851	177.22	156.76	1,902.57	2.299	90.76
	AU-OL5-3	40.41	0.005	0.033	0.026	13.03	0.177	46.11	0.210	0.015	85.91	4.619	7.042	179.05	163.84	1,974.19	2.434	92.58
	AU-OL5-4	40.54	0.005	0.036	0.028	13.01	0.180	46.02	0.187	0.014	85.93	5.201	7.819	189.10	157.51	2,019.35	1.964	89.25
	AU-OL5-5	40.29	0.007	0.034	0.021	13.42	0.176	45.91	0.151	0.014	85.58	4.562	6.534	145.27	161.47	2,084.72	3.909	84.34
	AU-OL5-6	39.59	0.005	0.034	0.023	13.54	0.182	46.48	0.155	0.014	85.61	4.827	7.125	157.78	164.79	2,003.41	4.148	90.28
	AU-OL5-7	39.96	0.005	0.042	0.024	13.64	0.184	46.01	0.147	0.015	85.40	4.254	7.534	161.11	162.59	2,184.13	3.224	86.53
	AU-OL5-8	39.80	0.007	0.038	0.021	13.82	0.186	46.01	0.133	0.014	85.26	4.601	6.883	146.90	163.08	2,244.84	3.653	89.76
	AU-OL5-9	39.91	0.006	0.037	0.022	13.60	0.186	46.13	0.117	0.015	85.50	4.243	6.895	151.94	167.64	2,248.95	3.862	96.74
	AU-OL5-10	40.17	0.004	0.037	0.022	13.08	0.181	46.37	0.140	0.014	86.01	4.249	7.002	153.48	158.95	2,276.16	3.264	92.27
	AU-OL6-1	40.27	0.004	0.033	0.026	13.38	0.182	45.91	0.206	0.016	85.54	4.788	7.307	180.31	160.90	2,146.97	1.700	92.96
	AU-OL6-2	39.89	0.005	0.035	0.025	13.39	0.181	46.31	0.170	0.018	85.68	4.872	6.867	173.46	159.57	2,287.16	2.795	88.73
	AU-OL6-3	39.65	0.005	0.037	0.024	13.28	0.181	46.65	0.179	0.016	85.86	4.800	6.970	166.52	161.58	2,199.88	2.566	83.08
	AU-OL6-4	39.60	0.006	0.040	0.023	13.13	0.177	46.87	0.158	0.020	86.07	4.427	7.193	160.37	160.61	2,121.72	3.244	86.54
	AU-OL6-5	40.48	0.005	0.035	0.026	13.35	0.187	45.75	0.178	0.017	85.56	4.863	7.365	179.66	158.40	2,139.47	2.595	88.57
	AU-OL6-6	39.43	0.005	0.036	0.025	13.81	0.182	46.34	0.186	0.021	85.31	5.385	6.534	171.23	161.10	2,047.71	2.964	92.93
	AU-OL6-7	40.03	0.005	0.035	0.024	13.29	0.182	46.28	0.159	0.017	85.77	4.468	6.855	167.62	163.28	2,078.17	4.120	93.91
	AU-OL6-8	40.24	0.004	0.035	0.026	13.26	0.184	46.01	0.201	0.059	85.68	4.621	6.862	178.30	162.80	2,062.10	3.319	88.39
	AU-OL6-9	39.94	0.005	0.035	0.024	13.02	0.175	46.63	0.175	0.019	86.10	4.426	6.696	166.31	160.58	2,039.92	3.744	90.18
	AU-OL6-10	39.72	0.004	0.037	0.026	13.49	0.178	46.38	0.168	0.027	85.62	4.573	6.968	178.64	160.02	2,002.19	3.042	87.21

-- = Not Analyzed

Table 2 (cont'd)

	Sample	SiO_2 wt%	TiO_2 wt %	Al_2O_3 wt%	$Cr2O_3$ wt %	FeO wt %	MnO wt %	MgO wt%	CaO wt%	Na_2O wt%	% Fo	Sc ppm	V ppm	Cr ppm	Co ppm	Ni ppm	Cu ppm	Zn ppm
Cumulate	AU-OL7-1	39.95	0.008	0.037	0.024	13.34	0.185	46.27	0.190	0.014	85.69	4.756	7.999	164.61	152.81	2,581.77	2.115	93.00
	AU-OL7-2	39.92	0.005	0.051	0.020	13.30	0.188	46.36	0.164	0.015	85.78	3.624	6.870	136.92	142.53	2,512.26	2.791	85.39
	AU-OL7-3	40.46	0.004	0.031	0.020	13.25	0.181	45.92	0.144	0.016	85.74	3.475	7.381	133.66	153.92	2,555.25	3.138	89.21
	AU-OL7-4	40.15	0.005	0.036	0.019	13.28	0.183	46.19	0.146	0.015	85.78	3.421	7.344	129.50	147.57	2,571.84	3.730	85.90
	AU-OL7-5	40.09	0.006	0.032	0.021	13.41	0.181	46.10	0.157	0.020	85.62	4.244	6.927	143.30	151.70	2,545.51	3.007	89.35
	AU-OL8-1	40.64	0.007	0.049	0.022	13.70	0.185	45.21	0.183	0.021	85.09	4.984	7.086	153.12	158.93	2,305.29	2.610	91.30
	AU-OL8-2	40.64	0.006	0.028	0.020	13.59	0.188	45.39	0.126	0.031	85.30	3.540	6.781	138.00	155.73	2,296.63	2.224	89.28
	AU-OL8-3	40.32	0.008	0.032	0.017	13.21	0.181	45.96	0.127	0.151	85.80	3.068	6.601	118.95	148.53	2,321.80	1.946	86.08
	AU-OL8-4	40.78	0.006	0.032	0.018	13.70	0.188	45.13	0.120	0.045	85.14	3.828	6.281	124.05	150.61	2,370.47	2.475	86.99
	AU-OL8-5	40.50	0.006	0.037	0.019	13.55	0.190	45.48	0.142	0.093	85.34	3.596	6.485	129.26	154.03	2,307.37	2.825	84.86
	AU-OL8-6	39.14	0.006	0.036	0.017	13.95	0.186	46.37	0.150	0.156	85.22	2.980	6.074	118.26	151.64	2,361.75	2.704	81.34
	AU-OL8-7	40.36	0.005	0.029	0.026	13.52	0.185	45.61	0.221	0.065	85.32	4.155	6.681	174.52	156.09	2,145.95	2.158	91.18
	AU-OL8-8	40.35	0.006	0.042	0.023	13.64	0.180	45.44	0.201	0.129	85.19	4.247	7.124	157.63	159.20	2,277.48	2.424	91.67
	AU-OL8-9	40.31	0.006	0.033	0.021	13.50	0.183	45.77	0.151	0.047	85.46	4.013	6.731	141.76	155.51	2,273.18	3.148	93.15
	AU-OL8-10	40.20	0.007	0.033	0.018	13.24	0.185	46.10	0.139	0.084	85.79	3.463	6.225	122.35	151.42	2,415.16	3.207	90.90
	AU-OL9-1	39.80	0.008	0.053	0.048	13.42	0.176	46.35	0.192	0.014	85.65	5.099	13.281	329.40	143.79	2,167.47	0.837	91.63
	AU-OL9-2	40.23	0.009	0.051	0.048	14.08	0.194	45.23	0.192	0.016	84.74	5.354	18.200	330.85	144.62	2,121.11	0.466	93.37
	AU-OL9-3	39.57	0.010	0.057	0.048	14.05	0.195	45.85	0.199	0.056	84.93	6.052	19.089	331.77	148.25	2,115.38	0.501	94.31
	AU-OL9-4	39.62	0.009	0.108	0.048	13.99	0.195	45.77	0.216	0.085	84.94	6.085	13.224	328.61	145.81	2,127.43	0.502	93.25
	AU-OL9-5	40.58	0.017	0.382	0.050	14.12	0.199	44.16	0.294	0.210	84.26	6.076	19.118	339.36	137.29	1,932.63	0.944	90.93
	AU-OL10-1	40.38	0.007	0.054	0.026	13.49	0.183	45.69	0.175	0.017	85.42	4.759	7.202	175.77	157.28	2,293.08	3.751	92.97
	AU-OL10-2	40.10	0.006	0.034	0.023	13.10	0.180	46.41	0.149	0.026	86.00	4.081	6.439	156.40	153.48	2,226.20	4.127	88.01
	AU-OL10-3	40.44	0.005	0.035	0.023	13.43	0.183	45.69	0.139	0.071	85.52	3.940	6.375	155.18	152.79	2,289.42	4.612	94.77
	AU-OL10-4	40.48	0.005	0.030	0.026	13.45	0.188	45.65	0.170	0.033	85.45	3.936	6.671	178.14	168.73	2,259.38	4.017	89.20
	AU-OL10-5	40.59	0.006	0.041	0.026	13.17	0.182	45.68	0.213	0.103	85.66	4.266	6.435	175.10	170.80	2,210.36	3.572	94.60
	AU-OL10-6	40.00	0.006	0.040	0.023	13.81	0.185	45.70	0.160	0.095	85.16	3.849	6.815	155.78	154.01	2,275.70	3.065	92.33
	AU-OL10-7	40.70	0.007	0.040	0.024	13.68	0.184	45.18	0.173	0.033	85.12	3.976	6.862	161.15	155.25	2,312.46	4.459	95.20
	AU-OL10-8	40.25	0.006	0.035	0.023	13.40	0.189	45.93	0.138	0.049	85.60	3.600	6.633	153.98	152.21	2,254.90	3.475	91.98
	AU-OL10-9	40.68	0.006	0.039	0.026	13.69	0.183	45.21	0.162	0.029	85.12	4.083	6.660	175.90	165.87	2,286.66	4.081	90.30
	AU-OL10-10	39.99	0.005	0.034	0.026	13.66	0.186	45.95	0.145	0.024	85.37	4.062	6.557	176.32	164.76	2,285.32	4.385	102.36
Replacement Dunite	AE-OL1-1	40.08	0.004	0.022	0.015	12.55	0.163	47.10	0.069	--	86.77	2.379	3.535	101.19	156.26	2,650.65	2.286	103.38
	AE-OL1-2	39.47	0.004	0.017	0.015	11.81	0.156	48.47	0.053	--	87.77	2.353	3.790	104.58	154.22	2,575.07	1.955	73.85
	AE-OL1-3	39.82	0.003	0.016	0.014	11.06	0.149	48.88	0.060	--	88.54	2.410	3.255	95.53	149.27	2,516.15	1.993	66.11
	AE-OL1-4	39.69	0.003	0.015	0.015	11.29	0.148	48.77	0.062	--	88.30	2.559	3.661	101.90	151.22	2,504.43	1.882	68.88
	AE-OL1-5	40.15	0.004	0.024	0.013	12.00	0.155	47.44	0.098	--	87.32	2.253	3.471	86.40	151.61	2,584.54	1.967	65.94
	AE-OL2-1	40.77	0.003	0.016	0.012	10.74	0.143	48.26	0.055	--	88.71	2.303	3.232	84.40	149.55	2,518.40	1.668	62.68
	AE-OL2-2	40.80	0.004	0.017	0.012	11.24	0.152	47.71	0.064	--	88.11	2.662	3.345	84.10	149.59	2,560.74	1.567	63.90
	AE-OL2-3	40.26	0.003	0.020	0.012	11.34	0.151	48.15	0.074	--	88.11	2.346	3.322	85.12	150.65	2,570.67	1.534	64.13
	AE-OL2-4	40.25	0.003	0.017	0.013	11.55	0.151	47.96	0.058	--	87.89	2.572	3.286	85.70	157.95	2,607.67	1.612	66.99
	AE-OL2-5	39.92	0.004	0.018	0.013	11.43	0.151	48.41	0.059	--	88.10	2.586	3.264	88.55	154.19	2,565.94	1.684	64.84
	AE-OL3-1	40.26	0.004	0.016	0.013	11.45	0.149	48.03	0.088	--	87.97	2.235	4.220	87.58	159.89	2,626.85	1.701	67.62
	AE-OL3-2	40.03	0.003	0.020	0.012	11.60	0.151	48.13	0.055	--	87.89	2.457	3.104	84.89	153.24	2,580.05	1.530	66.80
	AE-OL3-3	40.69	0.003	0.016	0.012	11.47	0.153	47.58	0.062	--	87.89	2.208	3.379	85.51	150.90	2,578.31	1.303	64.36
	AE-OL3-4	40.39	0.004	0.017	0.013	11.37	0.151	48.00	0.058	--	88.07	2.226	3.350	86.19	150.20	2,499.72	1.623	63.63
	AE-OL3-5	40.49	0.004	0.019	0.012	11.08	0.152	48.17	0.061	--	88.36	2.468	3.245	84.84	153.78	2,616.40	1.908	65.23
	AE-OL4-1	40.39	0.003	0.018	0.013	11.61	0.155	47.76	0.053	--	87.79	2.614	2.946	86.08	159.63	2,663.07	1.491	65.51
	AE-OL4-2	40.84	0.004	0.014	0.012	11.28	0.150	47.65	0.053	--	88.07	2.479	3.047	85.22	150.01	2,557.68	1.586	63.96
	AE-OL4-3	40.51	0.003	0.017	0.012	11.78	0.153	47.47	0.058	--	87.57	2.353	3.185	83.51	151.11	2,589.81	1.746	65.39
	AE-OL4-4	39.68	0.003	0.019	0.013	11.79	0.153	48.23	0.072	--	87.72	2.724	3.156	87.92	157.47	2,769.81	1.957	66.58
	AE-OL4-5	39.75	0.004	0.019	0.012	11.34	0.152	48.61	0.074	--	88.20	2.493	3.376	84.71	155.54	2,584.98	1.756	67.07
	AE-OL5-1	40.58	0.004	0.017	0.012	11.02	0.145	48.17	0.055	--	88.42	2.302	2.932	82.04	148.37	2,481.68	1.607	60.28
	AE-OL5-2	40.12	0.004	0.017	0.013	12.03	0.159	47.61	0.048	--	87.39	2.567	3.386	91.08	154.30	2,567.45	1.818	64.28
	AE-OL5-3	39.18	0.003	0.014	0.012	11.30	0.143	49.31	0.047	--	88.43	2.243	3.233	81.44	149.71	2,555.81	1.509	68.62
	AE-OL5-4	39.55	0.004	0.018	0.013	11.59	0.154	48.62	0.057	--	88.00	2.473	3.416	85.84	155.76	2,505.16	1.894	64.85
	AE-OL6-1	39.51	0.004	0.018	0.012	11.53	0.152	48.71	0.059	--	88.07	2.309	3.366	82.83	155.10	2,526.35	1.152	64.08
	AE-OL6-2	40.16	0.004	0.018	0.012	11.15	0.151	48.45	0.053	--	88.36	2.196	3.225	85.36	153.29	2,571.76	1.579	64.64
	AE-OL6-3	39.90	0.026	0.108	0.011	11.43	0.157	48.19	0.126	--	87.97	2.703	5.195	77.72	152.27	2,562.39	1.419	60.71
	AE-OL6-4	39.45	0.004	0.017	0.013	11.95	0.158	48.36	0.052	--	87.62	2.457	3.358	87.23	155.29	2,707.11	1.693	66.59
	AE-OL6-5	40.04	0.004	0.017	0.012	11.59	0.153	48.13	0.056	--	87.89	2.331	3.287	81.40	151.82	2,594.74	1.191	61.80
	AE-OL7-1	39.20	0.004	0.016	0.013	11.74	0.149	48.83	0.057	--	87.92	2.498	3.657	87.33	154.91	2,604.58	1.538	64.37
	AE-OL7-2	39.94	0.003	0.017	0.012	11.28	0.150	48.54	0.056	--	88.27	2.488	3.179	81.96	152.90	2,631.09	1.624	66.92
	AE-OL7-3	40.35	0.005	0.052	0.013	11.00	0.147	48.36	0.068	--	88.47	2.346	3.314	86.87	145.13	2,559.91	5.748	62.15
	AE-OL7-4	39.90	0.004	0.019	0.013	11.73	0.149	48.09	0.089	--	87.72	2.396	3.568	85.71	159.47	2,620.82	1.481	63.90
	AE-OL7-5	39.48	0.004	0.019	0.012	11.20	0.146	49.08	0.060	--	88.45	2.586	3.004	83.49	150.03	2,585.70	1.529	60.55
	AE-OL8-1	40.14	0.004	0.017	0.013	11.17	0.148	48.45	0.065	--	88.34	2.520	3.258	86.05	152.21	2,537.25	1.156	65.49
	AE-OL8-2	40.12	0.004	0.016	0.013	11.05	0.145	48.58	0.059	--	88.48	2.500	3.165	86.71	151.62	2,519.45	1.061	63.63
	AE-OL9-1	40.58	0.003	0.025	0.012	10.54	0.144	48.51	0.095	--	88.89	2.281	3.152	80.92	147.01	2,524.17	0.963	64.71
	AE-OL9-2	39.78	0.003	0.025	0.013	11.42	0.151	48.39	0.117	--	88.03	2.568	3.406	87.41	151.17	2,615.20	2.206	70.55
	AE-OL10-1	39.81	0.004	0.018	0.011	11.75	0.153	48.19	0.060	--	87.76	2.126	3.20	78.58	156.89	2,620.67	1.415	60.12
	AE-OL10-2	39.56	0.010	0.047	0.013	11.92	0.152	48.12	0.105	--	87.54	2.412	3.762	87.75	151.67	2,595.92	1.492	59.53
	AE-OL10-3	39.68	0.004	0.027	0.012	11.33	0.147	48.51	0.121	--	88.14	2.556	3.029	82.91	149.83	2,516.85	1.625	65.40
	AE-OL10-4	39.07	0.004	0.015	0.012	11.27	0.155	49.41	0.056	--	88.45	2.367	3.457	82.49	150.15	2,529.13	1.083	60.61
	AE-OL10-5	40.49	0.004	0.022	0.012	11.78	0.156	47.38	0.081	--	87.52	2.464	3.521	82.95	158.00	2,617.25	1.320	66.33
	AE-OL11-1	39.16	0.012	0.055	0.014	12.61	0.166	47.85	0.120	--	86.84	2.464	4.380	97.97	159.85	2,550.91	4.605	68.03
	AE-OL11-2	39.10	0.005	0.028	0.012	12.02	0.155	48.56	0.074	--	87.59	2.562	3.300	81.71	158.06	2,656.05	6.216	63.39
	AE-OL11-3	39.15	0.006	0.028	0.013	13.10	0.170	47.30	0.104	--	86.28	2.457	3.532	86.77	168.33	2,830.31	1.857	72.29
	AE-OL11-4	39.17	0.005	0.024	0.015	12.29	0.155	48.29	0.048	--	87.31	2.299	4.959	100.47	150.18	2,470.43	1.768	59.96
	AE-OL11-5	41.11	0.005	0.026	0.012	12.10	0.152	46.21	0.137	--	86.89	2.338	3.357	79.10	157.47	2,522.92	4.906	59.00
	AE-OL12-1	39.15	0.005	0.021	0.012	11.46	0.154	49.12	0.065	--	88.21	1.996	3.245	83.17	143.08	2,438.30	1.868	58.98
	AE-OL12-2	41.05	0.007	0.028	0.011	11.68	0.152	46.85	0.102	--	87.47	2.281	3.061	78.12	146.60	2,434.69	1.900	63.55
	AE-OL12-3	39.84	0.005	0.029	0.012	12.00	0.149	47.87	0.061	--	87.47	2.816	3.500	82.46	156.62	2,560.19	2.231	66.51
	AE-OL12-4	40.38	0.005	0.049	0.012	11.43	0.150	47.49	0.162	--	87.77	1.900	3.189	83.55	149.92	2,476.20	1.648	63.13
	AE-OL12-5	40.41	0.015	0.079	0.012	11.46	0.152	47.67	0.110	--	87.84	2.507	4.290	79.76	150.52	2,520.87	1.706	62.79
	AE-OL13-1	40.04	0.005	0.017	0.012	11.67	0.153	48.04	0.060	--	87.79	2.334	3.524	84.29	153.78	2,528.92	1.754	62.42
	AE-OL13-2	40.37	0.005	0.020	0.012	11.42	0.156	47.96	0.053	--	88.01	2.726	3.231	79.29	156.54	2,651.25	1.463	63.58
	AE-OL13-3	39.81	0.004	0.017	0.013	11.27	0.146	48.64	0.075	--	88.28	2.553	3.164	87.40	148.94	2,530.02	1.660	67.13
	AE-OL13-4	40.15	0.005	0.020	0.011	11.39	0.147	48.23	0.056	--	88.11	2.339	3.405	76.73	152.51	2,539.54	1.033	62.08
	AE-OL13-5	40.94	0.005	0.018	0.012	11.59	0.150	47.23	0.053	--	87.70	2.206	3.203	79.95	155.33	2,676.20	1.667	68.91
	AE-OL14-1	39.88	0.012	0.234	0.000	12.28	0.162	47.21	0.131	--	86.97	1.876	3.961	88.53	143.77	2,348.01	3.408	64.46

-- = Not Analyzed

Table 3 Orthopyroxene mineral chemistry

	Sample	SiO_2 wt%	TiO_2 wt %	Al_2O_3 wt%	FeO wt %	MnO wt %	MgO wt%	CaO wt%	Na_2O wt%	%En	Sc ppm	V ppm	Cr ppm	Co ppm	Ni ppm	Cu ppm	Zn ppm	Ga ppm	Sr ppm	Y ppm	Zr ppm	Nb ppm	La ppm	Ce ppm	Nd ppm	Sm ppm	Eu ppm	Gd ppm	Dy ppm	Er ppm	Yb ppm	Hf ppm
Deformed	AB-OPX1-1	56.35	0.169	2.802	5.836	0.130	33.76	0.832	0.122	89.71	17.64	86.09	4,814.88	56.53	763.19	1.636	40.25	3.162	1.035	0.975	6.680	0.083	0.045	0.167	0.155	0.079	0.030	0.094	0.148	0.101	0.167	0.133
	AB-OPX1-2	56.69	0.179	2.894	5.920	0.135	33.17	0.886	0.121	89.34	19.23	89.08	5,114.57	56.00	728.18	1.634	39.24	3.348	1.003	1.001	7.025	0.080	0.036	0.173	0.172	0.074	0.031	0.116	0.172	0.124	0.160	0.169
	AB-OPX1-3	55.83	0.171	2.793	5.954	0.139	34.09	0.898	0.125	89.53	19.07	87.78	4,663.75	57.10	730.15	1.847	41.54	3.544	1.069	1.062	7.156	0.067	0.036	0.151	0.174	0.076	0.033	0.085	0.144	0.130	0.148	0.176
	AB-OPX1-4	56.16	0.156	2.745	6.008	0.134	33.74	0.926	0.124	89.32	19.65	87.09	4,639.97	58.38	743.23	1.587	40.57	3.525	0.996	1.078	7.281	0.060	0.039	0.182	0.203	0.077	0.037	0.091	0.158	0.130	0.181	0.137
	AB-OPX1-5	57.14	0.165	2.807	5.883	0.133	32.87	0.885	0.124	89.31	19.15	86.29	4,958.72	57.15	732.28	2.014	41.16	3.397	1.002	1.070	7.037	0.057	0.035	0.166	0.169	0.075	0.033	0.133	0.146	0.120	0.177	0.163
	AB-OPX1-6	56.18	0.143	2.792	5.878	0.133	33.88	0.867	0.122	89.63	18.49	84.03	4,543.74	57.02	723.84	1.831	39.76	3.239	1.092	1.052	7.065	0.047	0.041	0.179	0.196	0.074	0.022	0.124	0.186	0.109	0.173	0.143
	AB-OPX1-7	56.67	0.174	2.903	6.060	0.134	33.03	0.915	0.119	89.06	20.09	86.02	4,839.06	58.30	726.36	2.038	39.38	3.188	0.868	0.978	6.766	0.075	0.040	0.153	0.174	0.045	0.029	0.098	0.155	0.128	0.162	0.149
	AB-OPX1-8	56.33	0.172	2.848	5.968	0.132	33.53	0.904	0.121	89.35	19.11	87.44	4,838.90	56.88	737.55	2.113	40.62	3.479	1.031	1.120	7.063	0.069	0.039	0.165	0.191	0.062	0.026	0.116	0.139	0.114	0.156	0.147
	AB-OPX1-9	56.57	0.171	2.824	5.908	0.137	33.36	0.902	0.128	89.38	19.48	88.79	4,874.24	55.48	713.12	2.009	39.88	3.734	1.010	0.963	7.016	0.050	0.042	0.167	0.192	0.087	0.025	0.095	0.172	0.112	0.154	0.172
	AB-OPX1-10	57.10	0.168	2.873	5.901	0.133	32.80	0.904	0.124	89.23	19.30	86.51	4,860.16	56.17	715.58	1.217	39.71	3.194	1.018	1.104	7.138	0.068	0.038	0.159	0.171	0.077	0.033	0.112	0.172	0.127	0.181	0.164
	AB-OPX-2-1	56.41	0.180	2.942	5.674	0.129	33.57	0.960	0.125	89.66	20.41	88.09	5,179.67	55.29	698.53	1.250	41.21	3.119	2.375	1.157	7.406	0.120	0.101	0.380	0.259	0.095	0.036	0.146	0.169	0.135	0.166	0.177
	AB-OPX-2-2	56.45	0.180	3.020	5.986	0.136	33.15	0.950	0.127	89.13	18.76	89.93	5,269.82	56.61	729.64	1.298	39.21	3.692	1.712	1.094	7.562	0.137	0.066	0.237	0.216	0.088	0.027	0.127	0.174	0.128	0.169	0.168
	AB-OPX-2-3	55.80	0.176	3.047	5.780	0.133	34.01	0.937	0.122	89.67	19.84	88.96	5,196.41	56.26	703.14	1.416	39.78	3.267	1.627	1.048	7.292	0.105	0.059	0.254	0.213	0.094	0.029	0.133	0.167	0.140	0.163	0.170
	AB-OPX-2-4	55.80	0.180	2.951	5.957	0.136	33.87	0.982	0.131	89.23	20.48	90.45	5,270.29	57.64	742.70	2.018	41.80	3.525	1.508	1.033	7.458	0.119	0.054	0.210	0.168	0.095	0.031	0.126	0.186	0.133	0.166	0.163
	AB-OPX-2-5	55.20	0.181	3.092	6.126	0.134	33.91	1.118	0.172	88.89	20.07	85.70	4,999.40	58.64	791.88	4.882	41.04	3.042	4.098	1.267	9.060	0.395	0.182	0.622	0.437	0.136	0.055	0.160	0.202	0.149	0.193	0.193
	AB-OPX3-1	55.72	0.197	3.157	6.423	0.139	33.03	1.099	0.158	88.26	19.37	86.48	4,925.36	57.76	817.35	9.431	41.53	3.906	5.600	1.120	10.09	1.094	0.279	0.691	0.486	0.088	0.057	0.152	0.211	0.151	0.168	0.217
	AB-OPX3-2	55.56	0.182	2.981	6.029	0.135	34.14	0.847	0.122	89.53	19.93	92.94	5,151.93	57.03	712.19	1.662	39.72	3.813	1.113	1.025	6.714	0.077	0.050	0.173	0.176	0.076	0.030	0.107	0.163	0.109	0.189	0.157
	AB-OPX3-3	56.17	0.187	3.101	6.069	0.137	33.04	1.136	0.138	88.67	21.73	93.20	5,244.69	55.86	740.13	7.150	39.17	3.889	4.385	1.175	7.502	0.337	0.204	0.617	0.448	0.125	0.044	0.154	0.186	0.124	0.178	0.182
	AB-OPX3-4	56.09	0.182	2.936	5.871	0.136	33.82	0.833	0.123	89.68	19.22	91.98	5,168.71	55.57	727.21	1.015	40.72	3.498	1.063	0.981	6.610	0.074	0.037	0.168	0.180	0.094	0.033	0.111	0.156	0.113	0.153	0.161
	AB-OPX3-5	56.59	0.172	2.945	5.751	0.131	33.45	0.840	0.124	89.73	19.28	89.81	5,222.38	54.79	696.48	1.823	39.50	3.792	1.139	1.006	6.484	0.075	0.051	0.180	0.204	0.042	0.031	0.091	0.133	0.126	0.151	0.158
	AB-OPX4-1	56.55	0.170	2.830	5.830	0.131	33.47	0.894	0.122	89.53	19.52	88.47	4,877.71	79.22	708.62	1.073	41.11	2.918	1.086	0.992	6.532	0.085	0.033	0.151	0.171	0.072	0.027	0.106	0.151	0.115	0.177	0.138
	AB-OPX4-2	56.82	0.166	2.828	5.889	0.132	33.13	0.911	0.125	89.33	17.78	86.07	4,927.89	75.77	715.23	1.169	41.85	3.401	1.179	0.979	6.681	0.066	0.037	0.187	0.192	0.074	0.024	0.116	0.135	0.119	0.138	0.155
	AB-OPX4-3	56.31	0.174	2.899	5.839	0.131	33.59	0.928	0.127	89.50	19.19	85.20	4,825.08	63.47	706.84	1.104	38.75	3.399	1.097	0.950	7.066	0.081	0.034	0.169	0.189	0.069	0.031	0.099	0.161	0.129	0.171	0.159
	AB-OPX4-4	56.51	0.181	2.969	5.802	0.134	33.19	0.970	0.237	89.36	21.07	85.51	4,978.86	56.77	707.08	1.283	31.28	3.369	1.520	1.097	8.426	0.086	0.071	0.209	0.181	0.085	0.040	0.119	0.170	0.132	0.186	0.196
	AB-OPX4-5	56.90	0.168	2.727	5.995	0.138	33.16	0.788	0.127	89.40	17.77	92.50	5,032.91	55.96	747.60	1.450	40.96	3.475	0.931	0.918	6.119	0.060	0.051	0.157	0.123	0.060	0.035	0.099	0.151	0.100	0.157	0.140
	AB-OPX5-1	56.01	0.168	2.865	5.915	0.135	33.90	0.877	0.127	89.57	18.83	87.56	4,847.75	65.05	736.04	1.356	40.92	3.162	1.093	1.006	6.754	0.069	0.062	0.167	0.190	0.066	0.025	0.126	0.147	0.133	0.161	0.160
	AB-OPX5-2	56.60	0.156	2.762	5.862	0.136	33.43	0.930	0.123	89.42	18.50	87.18	4,584.81	55.75	717.24	1.480	39.21	3.416	1.100	1.001	6.947	0.063	0.037	0.160	0.173	0.097	0.025	0.118	0.139	0.118	0.162	0.140
	AB-OPX5-3	56.77	0.162	2.735	5.901	0.134	33.28	0.894	0.123	89.38	17.92	86.30	4,486.93	56.80	728.88	1.401	39.18	2.935	1.047	0.991	6.921	0.078	0.031	0.175	0.132	0.083	0.028	0.124	0.155	0.102	0.184	0.149
	AB-OPX5-4	56.61	0.172	2.863	5.814	0.134	33.40	0.878	0.125	89.56	19.18	87.02	4,911.29	56.68	727.05	1.380	40.56	2.960	0.940	0.984	6.754	0.062	0.036	0.159	0.142	0.064	0.030	0.100	0.158	0.124	0.146	0.174
	AB-OPX5-5	56.56	0.174	2.897	5.812	0.132	33.41	0.894	0.122	89.54	19.44	88.99	4,806.26	56.29	709.99	1.996	39.66	3.283	1.129	1.121	7.211	0.055	0.043	0.170	0.196	0.059	0.034	0.102	0.157	0.128	0.200	0.154
	AB-OPX5-6	57.00	0.172	2.792	5.877	0.133	33.05	0.853	0.124	89.42	19.52	86.57	4,907.66	57.36	689.65	1.252	40.30	3.259	1.031	1.010	6.524	0.075	0.042	0.166	0.167	0.094	0.024	0.108	0.161	0.123	0.173	0.152
	AB-OPX5-7	56.51	0.165	2.847	5.842	0.133	33.46	0.921	0.127	89.47	18.53	84.77	4,690.48	57.61	723.47	1.554	39.84	3.360	1.073	1.079	7.271	0.067	0.034	0.166	0.212	0.067	0.025	0.101	0.167	0.120	0.168	0.153
	AB-OPX5-8	55.97	0.163	2.868	5.880	0.133	33.93	0.929	0.125	89.53	19.19	87.01	4,808.13	56.03	706.86	1.759	39.49	3.398	1.030	0.967	7.112	0.062	0.036	0.171	0.159	0.064	0.033	0.120	0.165	0.109	0.166	0.162
	AB-OPX5-9	55.86	0.174	2.851	6.068	0.137	33.87	0.917	0.128	89.29	19.97	90.24	4,898.26	67.94	739.01	1.908	40.04	3.124	1.046	1.000	6.980	0.071	0.041	0.159	0.146	0.071	0.026	0.134	0.162	0.103	0.150	0.168
	AB-OPX5-10	56.48	0.172	2.893	6.018	0.134	33.26	0.907	0.128	89.20	19.97	90.22	4,894.82	56.84	743.65	0.746	41.19	3.207	1.059	1.053	7.260	0.057	0.039	0.168	0.196	0.055	0.026	0.137	0.160	0.116	0.161	0.146
	AB-OPX6-1	57.63	0.129	2.659	5.775	0.131	32.70	0.850	0.122	89.46	18.06	80.55	4,272.74	54.97	724.88	1.556	40.91	3.122	1.013	0.970	6.896	0.063	0.040	0.146	0.185	0.073	0.038	0.153	0.141	0.121	0.181	0.124
	AB-OPX6-2	56.61	0.139	2.715	5.742	0.132	33.69	0.850	0.123	89.79	19.16	81.57	4,464.99	55.61	711.04	1.629	39.17	3.161	0.966	1.063	7.036	0.084	0.037	0.167	0.221	0.093	0.040	0.126	0.139	0.130	0.132	0.161
	AB-OPX6-3	56.09	0.137	2.624	5.936	0.135	34.08	0.876	0.128	89.59	18.48	82.77	4,304.10	56.84	725.07	1.276	41.70	2.929	1.088	0.947	6.876	0.046	0.042	0.173	0.204	0.073	0.038	0.156	0.158	0.122	0.152	0.121
	AB-OPX6-4	56.48	0.138	2.664	5.889	0.138	33.68	0.891	0.127	89.52	19.55	82.16	4,446.41	59.01	760.30	1.059	40.37	3.005	1.003	1.073	7.241	0.086	0.046	0.162	0.183	0.059	0.024	0.139	0.180	0.120	0.149	0.143
	AB-OPX6-5	56.91	0.130	2.710	5.813	0.132	33.31	0.861	0.125	89.57	18.54	79.82	4,193.62	54.62	739.30	1.155	40.66	3.091	1.048	1.051	7.158	0.063	0.024	0.158	0.160	0.084	0.041	0.122	0.163	0.131	0.148	0.123
	AB-OPX6-6	56.65	0.152	2.691	5.926	0.134	33.46	0.864	0.122	89.45	19.46	81.04	4,359.58	55.19	728.80	1.294	40.06	3.153	0.871	0.941	6.542	0.079	0.050	0.169	0.163	0.092	0.026	0.123	0.131	0.127	0.150	0.145
	AB-OPX6-7	56.44	0.159	2.822	5.837	0.133	33.62	0.861	0.126	89.62	18.59	84.61	5,012.56	55.74	722.77	1.947	42.43	3.144	0.846	0.994	6.728	0.082	0.040	0.151	0.159	0.066	0.023	0.096	0.132	0.126	0.139	0.146
	AB-OPX6-8	56.93	0.159	2.640	5.707	0.130	33.44	0.869	0.122	89.73	18.09	80.86	4,389.04	56.10	710.20	1.515	39.66	3.247	0.980	1.039	6.740	0.067	0.035	0.160	0.184	0.066	0.026	0.102	0.137	0.110	0.139	0.129
	AB-OPX6-9	56.75	0.161	2.774	5.929	0.134	33.25	0.881	0.127	89.36	18.42	84.96	4,753.02	55.68	725.45	2.091	42.27	3.197	0.982	0.967	6.596	0.073	0.031	0.155	0.156	0.087	0.028	0.133	0.150	0.114	0.155	0.159
	AB-OPX6-10	56.89	0.166	2.781	5.803	0.134	33.21	0.897	0.123	89.49	20.28	85.47	4,559.52	56.46	722.44	1.867	40.65	3.192	0.972	1.104	6.853	0.067	0.038	0.172	0.195	0.077	0.030	0.090	0.144	0.122	0.149	0.148
Granular	BX-OPX1-1	55.79	0.117	4.225	6.785	0.147	32.16	0.660	0.113	88.25	15.09	92.04	1,712.71	59.82	746.61	1.198	37.08	2.832	0.118	1.192	1.502	--	BDL	0.013	0.019	0.012	0.012	0.042	0.110	0.178	0.273	0.052
	BX-OPX1-2	55.67	0.118	4.343	6.615	0.139	32.35	0.648	0.108	88.57	16.27	91.25	1,711.84	57.86	745.92	1.125	34.00	3.197	0.131	1.176	1.449	--	BDL	0.011	0.017	0.016	0.011	0.034	0.128	0.177	0.272	0.049
	BX-OPX1-3	55.30	0.121	4.498	6.771	0.140	32.38	0.679	0.111	88.31	16.34	93.49	1,849.74	60.86	735.06	1.776	33.92	3.115	0.107	1.254	1.683	--	BDL	0.012	0.022	0.015	0.011	0.062	0.138	0.193	0.283	0.049
	BX-OPX1-4	54.61	0.121	4.356	6.805	0.143	33.19	0.668	0.113	88.53	16.55	92.80	1,832.23	60.02	750.84	1.112	34.10	3.212	0.131	1.287	1.453	--	BDL	0.010	0.018	0.025	0.015	0.047	0.147	0.169	0.265	0.043
	BX-OPX1-5	56.04	0.124	4.348	6.827	0.145	31.72	0.690	0.112	88.00	15.91	94.69	1,893.11	60.22	769.34	1.343	34.61	3.369	0.140	1.217	1.604	--	0.003	0.010	0.027	BDL	0.014	0.064	0.136	0.169	0.280	0.044
	BX-OPX2-1	56.13	0.125	4.278	6.704	0.140	31.86	0.657	0.107	88.27	16.38	97.04	1,817.71	59.98	761.19	1.076	36.57	3.125	0.113	1.090	1.601	--	BDL	0.008	0.019	0.014	0.006	0.055	0.150	0.170	0.263	0.052
	BX-OPX2-2	55.62	0.131	4.295	6.674	0.144	32.41	0.618	0.112	88.56	15.23	95.55	1,917.52	59.78	757.82	1.110	37.05	3.293	0.109	1.203	1.514	--	BDL	0.015	0.032	0.027	0.011	0.077	0.139	0.178	0.265	0.049

Major and trace elements concentrations for orthopyroxene in xenoliths from Nekempte, Ethopia.

-- = Not Analyzed
BDL = Below Detection limit

Table 3 (cont'd)

	Sample	SiO_2 wt%	TiO_2 wt %	Al_2O_3 wt%	FeO wt %	MnO wt %	MgO wt%	CaO wt%	Na_2O wt%	%En	Sc ppm	V ppm	Cr ppm	Co ppm	Ni ppm	Cu ppm	Zn ppm	Ga ppm	Sr ppm	Y ppm	Zr ppm	Nb ppm	La ppm	Ce ppm	Nd ppm	Sm ppm	Eu ppm	Gd ppm	Dy ppm	Er ppm	Yb ppm	Hf ppm
Granular	BX-OPX2-3	55.85	0.124	4.205	6.465	0.135	32.57	0.551	0.102	89.01	14.92	92.12	1,933.26	57.65	723.15	0.979	34.24	3.130	0.131	1.120	1.408	--	BDL	0.010	0.020	0.018	0.006	0.050	0.119	0.143	0.237	0.041
	BX-OPX2-4	55.83	0.136	4.315	6.624	0.138	32.33	0.528	0.104	88.76	15.66	98.23	2,051.15	58.47	746.96	0.934	34.86	3.311	0.142	1.112	1.362	--	BDL	0.009	0.012	0.012	0.004	0.056	0.124	0.137	0.255	0.057
	BX-OPX2-5	55.68	0.136	4.389	6.737	0.143	32.14	0.661	0.112	88.31	15.60	98.67	2,123.25	60.26	754.22	1.109	36.79	2.915	0.159	1.256	1.578	--	0.004	0.012	0.040	0.027	0.015	0.059	0.158	0.149	0.270	0.063
	BX-OPX2-6	55.43	0.144	4.308	6.886	0.143	32.35	0.625	0.108	88.24	16.27	98.42	2,096.37	60.39	770.73	1.160	36.72	3.297	0.115	1.159	1.627	--	BDL	0.014	0.016	0.024	0.014	0.060	0.151	0.181	0.279	0.070
	BX-OPX2-7	55.89	0.146	4.377	6.784	0.142	31.99	0.568	0.105	88.36	15.73	100.66	2,130.20	60.13	759.43	1.098	34.66	3.234	0.107	1.196	1.490	--	0.005	0.011	0.039	0.026	0.012	0.056	0.130	0.147	0.269	0.082
	BX-OPX2-8	55.55	0.139	4.295	6.876	0.142	32.20	0.682	0.111	88.11	16.40	95.79	2,033.38	59.58	758.06	1.076	35.89	3.287	0.112	1.212	1.621	--	0.004	0.014	0.024	0.019	0.008	0.053	0.150	0.162	0.288	0.062
	BX-OPX2-9	55.67	0.129	4.344	6.678	0.141	32.34	0.585	0.105	88.59	14.41	94.15	1,933.12	60.13	754.78	1.152	34.96	3.024	0.175	1.141	1.529	--	0.004	0.010	0.019	0.021	0.009	0.044	0.139	0.160	0.280	0.065
	BX-OPX2-10	55.51	0.129	4.294	6.701	0.143	32.53	0.591	0.107	88.60	14.65	95.03	2,017.80	60.06	760.14	1.129	35.04	3.398	0.176	1.185	1.514	--	0.004	0.011	0.027	0.014	0.011	0.060	0.121	0.123	0.281	0.050
	BX-OPX3-1	55.60	0.124	4.496	6.699	0.146	32.16	0.666	0.109	88.36	15.31	94.54	1,865.16	57.37	751.51	1.812	35.84	3.434	0.080	1.223	1.627	--	BDL	0.008	0.019	BDL	0.012	0.067	0.144	0.165	0.272	0.037
	BX-OPX3-2	55.12	0.122	4.536	6.668	0.142	32.63	0.672	0.109	88.54	16.50	97.29	1,825.88	58.96	737.52	1.565	34.75	3.511	0.120	1.192	1.736	--	BDL	0.011	0.040	0.015	0.006	0.051	0.133	0.165	0.286	0.050
	BX-OPX3-3	54.99	0.116	4.369	6.731	0.142	32.91	0.634	0.109	88.61	14.83	93.40	1,656.25	61.94	756.91	1.642	32.90	2.808	0.108	1.226	1.479	--	0.008	0.008	0.022	BDL	0.011	0.032	0.142	0.182	0.269	0.046
	BX-OPX3-4	54.98	0.121	4.376	6.729	0.145	32.86	0.682	0.110	88.51	15.28	94.04	1,705.10	62.61	763.68	1.973	37.45	3.341	0.152	1.163	1.432	--	BDL	0.012	0.018	0.014	0.009	0.053	0.135	0.157	0.259	0.039
	BX-OPX3-5	55.22	0.121	4.341	6.679	0.142	32.72	0.666	0.108	88.56	16.53	93.29	1,720.33	66.76	746.85	1.459	36.29	3.133	0.142	1.275	1.608	--	BDL	0.008	0.018	0.030	0.011	0.068	0.133	0.172	0.250	0.046
	BX-OPX3-6	55.30	0.121	4.142	6.864	0.140	32.69	0.630	0.114	88.37	15.39	92.95	1,737.46	68.06	757.34	1.259	37.03	2.890	0.147	1.152	1.511	--	BDL	0.014	0.031	0.010	0.013	0.045	0.124	0.159	0.254	0.046
	BX-OPX3-7	55.61	0.121	4.412	6.684	0.144	32.25	0.660	0.113	88.42	16.17	91.92	1,815.56	64.39	755.11	1.811	35.31	3.080	0.218	1.230	1.589	--	0.005	0.014	0.017	0.027	0.009	0.050	0.130	0.163	0.279	0.057
	BX-OPX3-8	56.10	0.118	4.350	6.665	0.139	31.87	0.647	0.116	88.35	15.99	93.50	1,772.57	59.73	746.23	1.559	36.21	3.303	0.45	1.129	1.536	--	BDL	0.011	0.035	0.021	0.012	0.057	0.140	0.172	0.257	0.047
	BX-OPX3-9	55.35	0.117	4.564	6.789	0.142	32.25	0.669	0.112	88.26	16.00	95.51	1,834.88	61.41	762.65	1.349	35.34	3.392	0.152	1.310	1.758	--	BDL	0.015	0.022	0.025	0.013	0.054	0.133	0.181	0.296	0.050
	BX-OPX3-10	55.12	0.125	4.537	6.700	0.143	32.58	0.682	0.114	88.46	16.35	96.06	1,799.77	61.65	770.10	1.552	35.19	3.402	0.129	1.249	1.650	--	BDL	0.009	0.029	0.015	0.011	0.055	0.151	0.152	0.293	0.039
	BX-OPX4-1	55.10	0.123	4.704	6.905	0.146	32.14	0.715	0.147	87.99	16.35	93.92	1,835.86	62.63	848.98	1.279	37.69	3.652	0.810	1.272	2.125	--	BDL	0.011	0.025	0.016	0.009	0.053	0.131	0.205	0.288	0.051
	BX-OPX4-2	54.89	0.131	4.683	6.800	0.145	32.55	0.691	0.110	88.30	16.50	99.24	1,964.53	58.91	759.12	0.608	33.21	3.535	0.088	1.292	1.679	--	BDL	0.011	0.024	0.024	0.012	0.057	0.124	0.157	0.282	0.049
	BX-OPX4-3	55.26	0.131	4.586	6.742	0.143	32.38	0.649	0.109	88.40	15.81	97.43	1,977.15	58.25	742.06	0.967	34.33	3.185	0.087	1.255	1.709	--	BDL	0.007	0.015	0.020	0.010	0.047	0.119	0.166	0.251	0.045
	BX-OPX4-4	55.41	0.122	4.530	6.733	0.142	32.26	0.688	0.112	88.31	16.46	93.65	1,963.82	60.43	773.76	0.808	35.02	3.377	0.174	1.291	1.660	--	BDL	0.010	0.038	0.011	0.010	0.033	0.145	0.167	0.308	0.050
	BX-OPX4-5	55.84	0.125	4.501	6.739	0.141	31.85	0.694	0.108	88.16	15.86	95.67	1,908.64	59.62	754.32	0.701	32.93	3.350	0.128	1.227	1.601	--	BDL	0.010	0.028	BDL	0.011	0.036	0.133	0.163	0.307	0.049
	BX-OPX4-6	55.38	0.127	4.545	6.804	0.140	32.19	0.697	0.116	88.17	15.63	96.67	1,950.69	59.00	771.71	1.030	35.07	3.435	0.106	1.218	1.671	--	BDL	0.009	0.014	0.012	0.011	0.050	0.133	0.157	0.259	0.046
	BX-OPX4-7	54.90	0.130	4.551	6.747	0.144	32.70	0.714	0.115	88.38	16.71	98.48	1,940.10	59.44	752.10	1.248	36.61	3.293	0.192	1.343	1.721	--	BDL	0.012	0.018	0.031	0.012	0.055	0.128	0.157	0.299	0.052
	BX-OPX4-8	55.81	0.122	4.530	6.634	0.139	32.00	0.655	0.113	88.42	16.51	96.40	1,906.02	58.84	766.89	2.237	35.01	3.282	0.126	1.302	1.779	--	BDL	0.006	0.018	0.017	0.011	0.046	0.148	0.164	0.319	0.050
	BX-OPX4-9	55.69	0.129	4.522	6.877	0.144	31.86	0.666	0.114	88.02	16.89	98.98	2,002.76	59.24	772.45	0.988	33.85	3.218	0.168	1.249	1.672	--	BDL	0.007	0.013	0.013	0.013	0.047	0.131	0.140	0.263	0.053
	BX-OPX4-10	55.55	0.124	4.773	6.690	0.140	31.88	0.685	0.139	88.25	16.54	91.36	1,815.75	59.62	808.10	1.338	37.76	3.321	0.773	1.114	1.973	--	0.005	0.012	0.023	0.019	0.007	0.055	0.136	0.167	0.267	0.059
	BX-OPX5-1	55.20	0.122	4.416	6.607	0.141	32.70	0.698	0.114	88.60	16.07	93.75	1,803.58	58.85	761.39	1.431	34.55	3.298	0.112	1.229	1.600	--	BDL	0.005	0.033	0.024	0.006	0.060	0.146	0.180	0.288	0.047
	BX-OPX5-2	55.70	0.120	4.219	6.645	0.143	32.38	0.682	0.108	88.48	15.49	90.70	1,701.42	58.32	753.71	1.116	36.18	3.102	0.139	1.221	1.558	--	BDL	0.007	0.034	BDL	0.009	0.049	0.141	0.162	0.284	0.067
	BX-OPX5-3	55.36	0.128	4.320	6.666	0.145	32.60	0.674	0.109	88.53	15.43	90.09	1,817.96	58.07	749.34	1.162	33.11	3.259	0.119	1.234	1.605	--	BDL	0.009	0.033	0.017	0.013	0.047	0.120	0.168	0.284	0.052
	BX-OPX5-4	55.81	0.122	4.236	6.618	0.146	32.30	0.649	0.113	88.55	16.48	94.31	1,839.53	60.38	763.74	1.345	35.81	3.241	0.123	1.244	1.604	--	BDL	0.006	0.019	0.026	0.012	0.078	0.121	0.151	0.276	0.039
	BX-OPX5-5	55.71	0.128	4.399	6.775	0.145	32.01	0.723	0.111	88.11	16.36	94.69	1,861.35	59.48	746.54	1.638	36.30	3.300	0.098	1.270	1.776	--	BDL	0.008	0.026	0.020	0.014	0.037	0.122	0.157	0.321	0.047
	BX-OPX5-6	56.32	0.123	4.226	6.576	0.144	31.80	0.696	0.113	88.36	14.54	93.95	1,776.83	60.08	774.43	1.592	37.04	3.066	0.1149	1.223	1.630	--	BDL	0.005	0.021	0.023	0.008	0.049	0.114	0.166	0.285	0.045
	BX-OPX5-7	55.49	0.122	4.357	6.855	0.146	32.19	0.725	0.115	88.06	16.18	92.22	1,836.47	60.10	795.80	1.493	35.23	3.064	0.067	1.243	1.591	--	BDL	0.005	0.031	BDL	0.010	0.057	0.144	0.159	0.251	0.055
	BX-OPX5-8	55.50	0.123	4.249	6.831	0.145	32.32	0.720	0.112	88.14	15.77	91.04	1,927.13	60.44	763.11	1.349	36.67	3.099	0.096	1.324	1.666	--	BDL	0.010	0.007	0.013	0.009	0.047	0.131	0.158	0.269	0.036
	BX-OPX5-9	55.80	0.124	4.155	6.469	0.139	32.54	0.661	0.109	88.80	15.62	90.74	1,820.00	57.91	745.98	1.392	35.02	2.744	0.1158	1.219	1.451	--	BDL	0.005	0.025	BDL	0.011	0.045	0.162	0.176	0.265	0.053
	BX-OPX5-10	55.28	0.126	4.494	6.624	0.138	32.51	0.718	0.110	88.48	16.41	91.12	1,751.24	58.11	746.01	1.498	34.76	3.254	0.092	1.241	1.659	--	BDL	0.010	BDL	0.013	0.011	0.047	0.123	0.180	0.274	0.051
Cumulate	AU-OPX1-1	54.84	0.239	4.417	8.847	0.187	30.57	0.804	0.096	84.66	18.91	124.08	2,180.39	65.06	681.64	0.165	54.03	5.030	0.294	1.638	3.173	0.105	0.017	0.059	0.076	0.034	0.024	0.092	0.201	0.232	0.323	0.105
	AU-OPX1-2	54.98	0.244	4.617	8.612	0.180	30.33	0.921	0.117	84.66	20.99	132.36	2,501.28	62.73	673.44	0.641	51.14	5.089	1.367	1.905	3.393	0.062	0.053	0.152	0.124	0.084	0.024	0.100	0.221	0.211	0.353	0.105
	AU-OPX1-3	54.08	0.248	4.531	8.767	0.187	31.30	0.772	0.115	85.12	19.42	126.81	2,251.30	59.41	611.98	0.237	48.66	4.998	0.362	1.778	3.586	0.014	0.011	0.053	0.092	0.037	0.022	0.116	0.207	0.212	0.376	0.114
	AU-OPX1-4	55.22	0.236	4.357	8.723	0.185	30.36	0.764	0.153	84.80	19.48	125.25	2,214.12	59.57	645.78	6.836	51.04	4.911	0.316	1.619	3.576	0.014	0.014	0.080	0.077	0.060	0.026	0.100	0.177	0.229	0.319	0.106
	AU-OPX1-5	55.21	0.238	4.308	8.799	0.186	30.34	0.758	0.150	84.70	20.19	122.78	2,217.98	61.90	633.88	0.954	50.46	4.371	0.441	1.530	3.559	0.058	0.024	0.064	0.077	0.047	0.017	0.062	0.216	0.209	0.358	0.112
	AU-OPX1-6	53.99	0.253	4.356	9.255	0.188	30.97	0.785	0.189	84.33	19.91	128.96	2,336.79	60.57	636.57	0.808	49.17	4.738	0.441	1.710	4.186	0.026	0.025	0.076	0.112	0.060	0.029	0.111	0.216	0.204	0.330	0.156
	AU-OPX1-7	55.14	0.257	4.496	8.827	0.188	30.08	0.797	0.205	84.48	21.05	130.01	2,340.32	63.18	658.98	0.577	51.08	4.799	0.556	1.767	4.397	0.089	0.020	0.072	0.116	0.039	0.015	0.120	0.230	0.265	0.337	0.133
	AU-OPX1-8	54.48	0.271	4.543	8.832	0.188	30.75	0.781	0.153	84.79	19.55	130.64	2,345.96	60.33	637.15	0.571	49.92	5.393	0.311	1.782	3.710	0.018	0.011	0.054	0.083	0.052	0.015	0.107	0.193	0.231	0.351	0.120
	AU-OPX1-9	54.25	0.254	4.511	8.942	0.185	30.93	0.789	0.134	84.71	20.45	130.12	2,289.37	62.72	655.48	0.548	52.33	4.967	0.32	1.684	3.629	0.013	0.011	0.054	0.064	0.049	0.019	0.111	0.210	0.223	0.369	0.120
	AU-OPX1-10	54.74	0.256	4.505	8.859	0.186	30.54	0.798	0.118	84.64	19.35	132.63	2,400.08	60.12	639.79	0.512	52.83	5.283	0.279	1.742	3.650	0.012	0.019	0.046	0.064	0.046	0.016	0.091	0.212	0.214	0.341	0.121
	AU-OPX2-1	54.61	0.248	4.477	8.913	0.189	30.66	0.795	0.092	84.62	20.22	124.93	2,144.20	61.00	647.66	0.355	50.91	5.108	0.704	1.651	3.518	0.173	0.029	0.086	0.092	0.014	0.019	0.112	0.206	0.238	0.358	0.122
	AU-OPX2-2	55.39	0.238	4.497	8.572	0.185	30.14	0.885	0.091	84.70	21.96	128.00	2,333.44	70.30	666.02	0.214	52.15	5.102	0.297	1.675	2.842	0.016	0.010	0.046	0.109	0.054	0.026	0.087	0.192	0.203	0.353	0.128
	AU-OPX2-3	55.40	0.237	4.354	8.839	0.187	30.12	0.761	0.102	84.54	19.56	126.31	2,216.41	64.34	637.85	0.162	49.62	5.057	0.309	1.750	3.227	0.034	0.014	0.046	0.122	0.047	0.015	0.102	0.204	0.220	0.321	0.105
	AU-OPX2-4	55.13	0.247	4.585	8.788	0.188	30.14	0.768	0.153	84.61	19.23	127.12	2,189.26	61.83	644.24	0.259	46.40	4.710	0.4687	1.631	3.827	0.044	0.017	0.077	0.089	0.043	0.026	0.106	0.210	0.236	0.314	0.117
	AU-OPX2-5	54.61	0.244	4.448	8.628	0.184	30.89	0.799	0.182	85.09	20.55	127.06	2,168.72	62.81	656.99	0.149	52.34	4.792	0.372	1.734	3.713	0.013	0.017	0.064	0.076	0.030	0.027	0.102	0.215	0.205	0.311	0.112

-- = Not Analyzed

BDL = Below Detection limit

Table 4 Clinopyroxene mineral chemistry

	Sample	SiO2 wt%	TiO2 wt %	Al2O3 wt%	FeO wt %	MnO wt %	MgO wt%	CaO wt%	Na2O wt%	% Wo	%En	% Fs	Sc ppm	V ppm	Cr ppm	Co ppm	Ni ppm	Cu ppm	Zn ppm	Ga ppm
Deformed	AB-CPX1-1	53.98	0.565	4.253	3.159	0.090	17.06	19.52	1.288	42.69	51.91	5.390	83.05	272.59	11,800.06	25.18	431.90	21.32	11.96	5.850
	AB-CPX1-2	53.61	0.574	3.863	3.112	0.089	17.63	19.88	1.173	42.44	52.38	5.190	84.74	275.37	11,995.37	24.61	401.99	13.32	10.00	5.589
	AB-CPX1-3	53.56	0.562	4.253	3.233	0.090	16.99	19.96	1.294	43.28	51.25	5.470	79.93	266.11	11,522.49	24.63	395.20	11.66	11.00	5.477
	AB-CPX1-4	53.58	0.604	3.446	3.114	0.091	17.67	20.37	1.012	42.98	51.89	5.130	87.76	286.86	12,012.79	26.14	438.59	27.60	10.35	5.284
	AB-CPX1-5	54.11	0.593	3.406	3.447	0.090	17.58	19.43	1.059	41.71	52.52	5.780	87.23	293.61	11,946.47	29.52	589.92	51.33	13.25	5.303
Cumulate	AU-CPX1-1	51.23	0.953	6.774	4.477	0.121	15.59	19.64	1.210	43.81	48.39	7.800	65.11	301.66	4,031.66	25.00	336.84	2.208	13.74	6.173
	AU-CPX1-2	51.13	0.849	6.863	4.444	0.119	15.38	20.00	1.221	44.58	47.69	7.730	65.57	295.83	3,655.85	23.86	338.14	2.383	13.34	5.868
	AU-CPX1-3	51.30	0.839	6.871	4.579	0.126	15.11	19.95	1.219	44.79	47.19	8.020	62.29	296.89	3,793.21	24.63	349.77	2.153	12.58	5.916
	AU-CPX1-4	50.91	0.862	6.917	4.597	0.123	15.09	20.29	1.197	45.21	46.79	7.990	61.49	299.27	3,874.32	24.15	340.14	2.060	12.80	6.218
	AU-CPX1-5	50.96	0.837	6.929	4.539	0.124	15.26	20.14	1.218	44.83	47.28	7.890	62.00	298.34	3,903.34	23.94	348.56	2.357	13.41	6.354
	AU-CPX1-6	51.00	0.783	7.027	4.424	0.126	15.18	20.16	1.288	45.07	47.22	7.720	62.69	297.27	3,813.77	23.92	346.74	1.831	13.56	6.562
	AU-CPX1-7	51.08	0.868	6.997	4.440	0.121	15.43	19.86	1.207	44.34	47.92	7.740	64.19	300.65	3,876.32	22.83	346.73	2.138	12.87	6.377
	AU-CPX1-8	51.57	0.787	7.035	4.557	0.122	15.51	19.24	1.183	43.35	48.64	8.020	62.56	287.14	3,720.69	24.75	349.42	2.038	14.13	6.142
	AU-CPX1-9	51.26	0.820	6.733	4.678	0.128	15.60	19.59	1.180	43.58	48.30	8.120	63.24	297.51	3,777.33	24.90	339.36	1.791	13.60	5.846
	AU-CPX1-10	50.61	0.959	6.856	4.484	0.118	15.56	20.20	1.208	44.54	47.75	7.720	64.92	305.58	3,991.12	25.02	361.08	1.731	13.82	6.433

	Sample	Rb ppm	Sr ppm	Y ppm	Zr ppm	Nb ppm	Ba ppm	La ppm	Ce ppm	Nd ppm	Sm ppm	Eu ppm	Dy ppm	Yb ppm	Hf ppm	Ta ppm	Pb ppm	Th ppm	U ppm
Deformed	AB-CPX1-1	2.869	304.21	14.97	131.76	1.577	6.577	16.60	44.36	25.58	5.253	1.665	3.268	1.118	3.333	0.165	0.135	0.357	0.092
	AB-CPX1-2	1.869	297.61	15.54	130.89	1.392	2.696	17.75	47.53	27.64	6.011	1.742	3.468	1.225	3.306	0.132	0.093	0.353	0.098
	AB-CPX1-3	1.760	324.55	15.15	139.45	1.779	1.215	18.27	48.97	27.83	5.869	1.867	3.501	1.084	3.499	0.167	0.111	0.537	0.121
	AB-CPX1-4	4.253	266.06	15.91	123.26	2.226	2.549	16.46	45.92	27.82	5.914	1.755	3.594	1.257	3.168	0.123	0.160	0.613	0.119
	AB-CPX1-5	8.134	227.45	15.68	103.18	2.557	10.69	14.19	42.04	25.95	5.698	1.561	3.380	1.191	2.688	0.147	0.249	0.522	0.128
Cumulate	AU-CPX1-1	--	80.32	24.72	46.69	0.316	0.068	3.437	12.13	11.33	3.422	1.245	4.380	2.246	1.413	0.067	0.213	0.086	0.020
	AU-CPX1-2	--	79.65	24.69	42.10	0.297	0.042	3.475	12.07	10.58	3.283	1.178	4.468	2.538	1.311	0.058	0.212	0.085	0.021
	AU-CPX1-3	--	81.25	23.85	42.97	0.273	BDL	3.474	12.54	10.77	3.032	1.207	4.233	2.324	1.258	0.050	0.167	0.081	0.017
	AU-CPX1-4	--	80.19	23.25	42.90	0.311	BDL	3.345	12.11	10.92	3.104	1.234	4.009	2.191	1.312	0.062	0.199	0.083	0.021
	AU-CPX1-5	--	80.23	24.36	43.53	0.338	BDL	3.521	12.49	11.14	3.273	1.218	4.343	2.273	1.286	0.068	0.211	0.084	0.022
	AU-CPX1-6	--	81.74	23.87	41.73	0.351	BDL	3.546	12.31	10.45	2.926	1.193	4.333	2.328	1.177	0.062	0.202	0.081	0.022
	AU-CPX1-7	--	80.82	24.17	45.61	0.377	0.167	3.469	12.06	10.89	3.207	1.240	4.403	2.288	1.351	0.064	0.182	0.084	0.021
	AU-CPX1-8	--	77.01	23.97	42.44	0.328	BDL	3.414	11.62	9.755	3.041	1.095	4.183	2.207	1.259	0.066	0.166	0.082	0.019
	AU-CPX1-9	--	77.02	23.30	41.22	0.370	0.384	3.372	11.92	10.17	2.823	1.136	4.026	2.319	1.234	0.060	0.200	0.080	0.019
	AU-CPX1-10	--	79.96	23.00	45.07	0.338	0.058	3.318	12.17	10.86	3.275	1.225	4.322	2.209	1.506	0.069	0.171	0.070	0.020

Major and trace elements concentrations for clinopyroxene in xenoliths from Nekempte, Ethopia.

-- = Not Analyzed
BDL = Below Detection limit

Table 5 Spinel mineral chemistry

	Sample	TiO2 wt %	Al2O3 wt%	FeO wt %	MnO wt %	MgO wt%	Cr#	Sc ppm	V ppm	Cr ppm	Co ppm	Ni ppm	Cu ppm	Zn ppm	Ga ppm	Al ppm
Granular	BX-SPL1-1	0.135	58.46	12.72	0.088	20.00	0.275	0.197	389.49	58,815	254.10	3,575.15	4.262	690.18	85.10	154,697
	BX-SPL1-2	0.140	58.12	12.60	0.089	20.25	0.281	0.389	415.11	60,252	246.19	3,745.52	3.551	661.34	82.42	153,798
	BX-SPL1-3	0.138	52.37	14.27	0.101	22.92	0.335	0.337	474.37	69,804	262.81	3,931.17	4.055	1,004.60	89.37	138,567
	BX-SPL1-4	0.128	53.39	14.70	0.112	21.92	0.321	0.226	489.41	66,686	263.01	4,094.78	4.033	953.37	80.39	141,271
	BX-SPL1-5	0.140	54.34	13.60	0.098	22.35	0.311	0.428	420.03	64,824	244.14	3,498.07	4.157	840.48	74.92	143,803
	BX-SPL2-1	0.140	58.10	12.54	0.090	20.29	0.282	0.763	409.08	60,463	246.95	3,570.94	3.706	616.94	78.78	153,738
	BX-SPL2-2	0.137	57.69	12.17	0.090	21.19	0.281	0.349	413.86	59,743	240.00	3,496.22	3.559	637.61	74.57	152,650
	BX-SPL2-3	0.147	56.35	13.43	0.100	21.04	0.291	0.448	435.84	61,103	231.01	3,226.43	3.507	715.75	73.50	149,113
	BX-SPL2-4	0.143	54.57	13.70	0.095	21.71	0.317	0.907	468.14	66,957	244.58	3,498.14	5.067	681.98	74.00	144,392
	BX-SPL2-5	0.134	52.54	14.07	0.099	22.95	0.334	0.682	445.38	69,808	254.91	3,616.74	4.248	816.38	74.99	139,033
	BX-SPL3-1	0.119	58.38	12.58	0.094	20.20	0.276	0.438	394.15	58,983	251.31	3,610.12	3.059	615.96	78.08	154,477
	BX-SPL3-2	0.115	57.39	13.71	0.094	20.03	0.281	0.968	388.71	59,251	250.54	3,752.57	3.303	665.08	78.15	151,858
	BX-SPL3-3	0.116	56.65	13.34	0.095	20.50	0.298	0.775	375.68	63,608	259.58	3,651.63	4.181	654.27	79.82	149,905
	BX-SPL3-4	0.113	58.40	12.53	0.091	20.32	0.275	0.752	400.11	58,487	234.51	3,417.28	3.163	580.03	73.13	154,526
	BX-SPL3-5	0.114	58.63	12.50	0.095	20.23	0.271	--	389.07	57,711	243.64	3,317.61	3.357	588.74	73.12	155,136
Cumulate	AU-SPL1-1	0.540	51.68	16.56	0.117	18.46	0.387	2.558	725.95	86,485	189.62	2,540.80	5.039	548.44	107.02	136,740
	AU-SPL1-2	0.537	52.08	16.27	0.113	18.27	0.387	3.146	773.14	87,157	189.13	2,501.80	5.031	499.90	103.23	137,814
	AU-SPL1-3	0.504	50.81	17.07	0.127	18.72	0.394	2.638	764.90	87,348	195.27	2,533.24	5.147	522.83	104.53	134,463
	AU-SPL1-4	0.516	49.22	17.78	0.120	19.37	0.406	2.084	778.46	88,858	199.80	2,921.66	--	589.41	104.06	130,247
	AU-SPL1-5	0.530	49.63	17.42	0.121	19.50	0.400	2.706	763.32	87,546	211.96	2,682.66	--	568.77	95.35	131,325
	AU-SPL2-1	0.655	50.05	17.76	0.133	17.71	0.414	3.248	757.60	93,696	198.02	2,452.42	8.226	537.87	98.26	132,436
	AU-SPL2-2	0.503	50.89	17.05	0.127	18.64	0.394	2.551	750.06	87,530	203.16	2,364.62	5.119	511.66	94.01	134,649
	AU-SPL2-3	0.825	47.77	19.67	0.155	18.10	0.422	2.837	849.42	92,198	208.82	2,390.59	6.994	624.54	100.09	126,404
Replacement Dunite	AE-SPL1-1	0.443	43.44	15.96	0.111	18.76	0.559	3.230	694.44	145,668	250.86	2,475.09	--	715.44	71.73	114,957
	AE-SPL1-2	0.384	44.23	16.39	0.112	17.88	0.551	1.589	681.37	143,771	238.68	2,327.16	3.677	751.54	67.76	117,033
	AE-SPL1-3	0.435	41.02	17.42	0.111	17.97	0.592	1.133	716.42	157,665	241.73	2,345.52	--	737.24	87.83	108,537
	AE-SPL2-1	0.367	43.59	15.85	0.117	18.91	0.557	1.949	740.40	144,811	249.58	2,422.66	6.709	993.24	73.01	115,345
	AE-SPL2-2	0.354	43.70	16.22	0.112	18.19	0.559	2.680	725.43	146,546	239.85	2,422.87	4.778	850.03	74.92	115,631
	AE-SPL2-3	0.400	43.01	16.68	0.112	18.15	0.565	1.079	753.26	148,092	238.40	2,350.91	6.052	781.33	68.34	113,814
	AE-SPL3-1	0.426	42.96	16.47	0.113	17.71	0.573	2.511	731.01	152,660	237.63	2,305.13	4.460	738.54	70.84	113,684
	AE-SPL3-2	0.409	44.10	15.73	0.111	17.67	0.563	2.270	729.26	150,410	234.25	2,286.43	5.196	799.39	76.29	116,682
	AE-SPL3-3	0.456	39.91	16.40	0.126	23.18	0.564	2.685	680.53	136,371	232.12	2,583.97	8.899	832.77	67.16	105,599
	AE-SPL4-1	0.759	39.77	17.89	0.130	19.48	0.588	2.207	764.69	150,371	256.42	2,744.47	--	855.31	84.76	105,230
	AE-SPL5-1	0.419	42.68	16.05	0.116	18.42	0.575	2.224	776.16	152,704	231.87	2,405.93	5.808	837.13	68.68	112,943
	AE-SPL5-2	0.529	42.15	16.08	0.115	18.66	0.580	2.228	763.81	153,752	238.59	2,473.86	6.336	909.62	76.95	111,536
	AE-SPL5-3	0.434	42.86	16.32	0.118	17.63	0.577	1.359	765.17	154,911	231.73	2,348.40	5.335	901.13	71.87	113,408
	AE-SPL5-4	0.374	43.24	17.03	0.114	18.36	0.555	2.117	727.02	142,899	226.79	2,411.54	6.087	854.18	72.94	114,415
	AE-SPL6-1	0.399	40.45	16.99	0.111	20.06	0.584	1.348	754.16	150,454	228.49	2,175.42	9.701	940.30	69.90	107,039

Major and minor element concentrations for spinel in xenoliths from Nekempte, Ethiopia

-- = Not Analyzed
BDL = Below Detection Limit

Table 6 Regional thermobarometry

Sample Name	Location	Temperature (°C)	Pressure (GPa)
This Study			
3143 ab lherzolite	Dedessa	1100	1.00
3143 au lherzolite	Dedessa	1070	1.07
Orlando et al. (2006)			
Spinel lherzolite	Megado/Dilo	949	1.87
Group B pyroxenite	Megado/Dilo	1152	2.32
Group C pyroxenite	Megado/Dilo	898	1.3
Group D pyroxenite	Megado/Dilo	926	1.46
Ferrando et al. (2008)			
IJN16 peridotite (*deformed*)	Injabara	984	1.5
INJ34 peridotite (*transitional*)	Injabara	1015	1.8
INJ3 peridotite (*granular*)	Injabara	991	1.5
Ahmed et al. (2016)			
Xn2 harzburgite	Kishb*	950	1.1
Xn4 harzburgite	Kishb	948	1.1
Xn5 harzburgite	Kishb	924	1.4
Xn6 harzburgite	Kishb	969	1.4
Xn7 harzburgite	Kishb	985	1.0
Xn8 harzburgite	Kishb	1170	1.4
Xn3 wherlite	Kishb	1106	1.2
Conticelli et al. (1999)			
Ets 210a lherzolite	Mer'awi	978	1.24
Ets 210b dunite	Mer'awi	990	1.39
Ets 264/19 lherzolite	West Injabara	949	1.01
Ets 264/12c harzburgite	West Injabara	934	1.06
Ets 264/13a hbl harzburgite	West Injabara	875	1.15
Ets 213 b lherzolite	North Injabara	970	1.08
Ets 243 n harzburgite	Dedessa	1045	1.13
Etn 1a lherzolite	Megga	997	1.30
Etn 1b lherzolite	Megga	980	1.08
Etn 2b lherzolite	Megga	993	1.34
Etn 2c dunite	Megga	965	0.83
Etn 4a harzburgite	Megga	909	0.70
Etn 5a lherzolite	Megga	965	1.03
Etn 6a harzburgite	Megga	1034	0.90
Etn 6b lherzolite	Megga	978	0.98
Etn 7a websterite	Megga	878	0.67
Etn 7b harzburgite	Megga	943	0.74
Etn 8a harzburgite	Megga	975	0.80
Etn 8b lherzolite	Megga	985	1.11
Etn 9a harzburgite	Megga	963	0.84
Etn 10 lherzolite	Megado	959	1.06
Etn 11 lherzolite	Megado	958	1.13
Etn 12 lherzolite	Megado	921	0.93

*In another section of the Nubian Shield. Harrat Kishb is located in Saudi Arabia.

Thermobarometry data from this study and other regional data from Dedessa, Megado/Dilo, Injibara, West Injibara, Kishb, Mer-awi, and Megga locations. Data from this study were calculated with the two-pyroxene method from Purtika, (2008). Standard error for temperature and pressure are 58° C and 2.8 kbar, respectively.

APPENDIX B

FIGURES

Figure 1 East African Rift System (EARS) Location

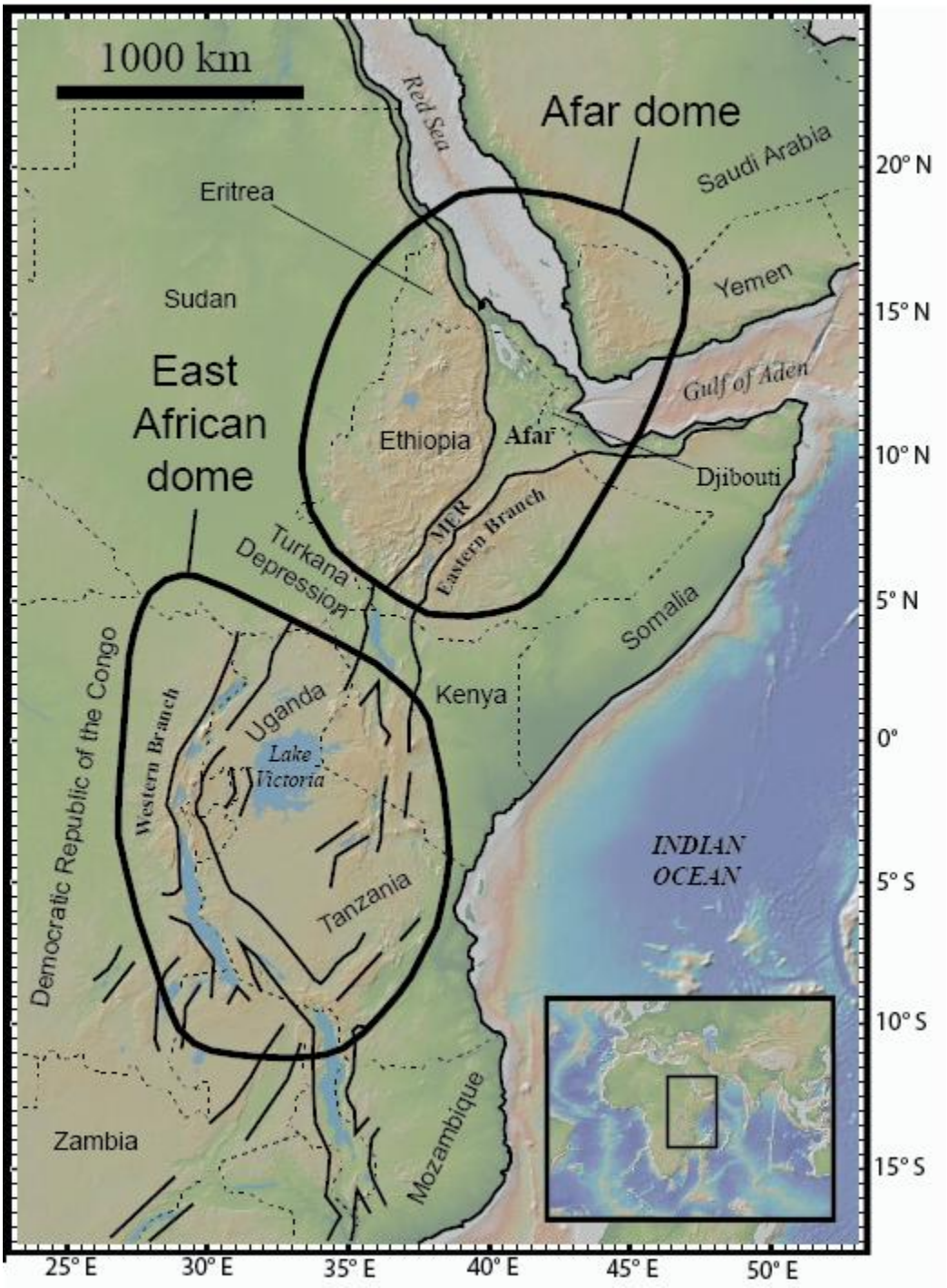

Location of the East African Rift System (EARS).

Figure 2 Main Ethiopian Rift (MER) Location

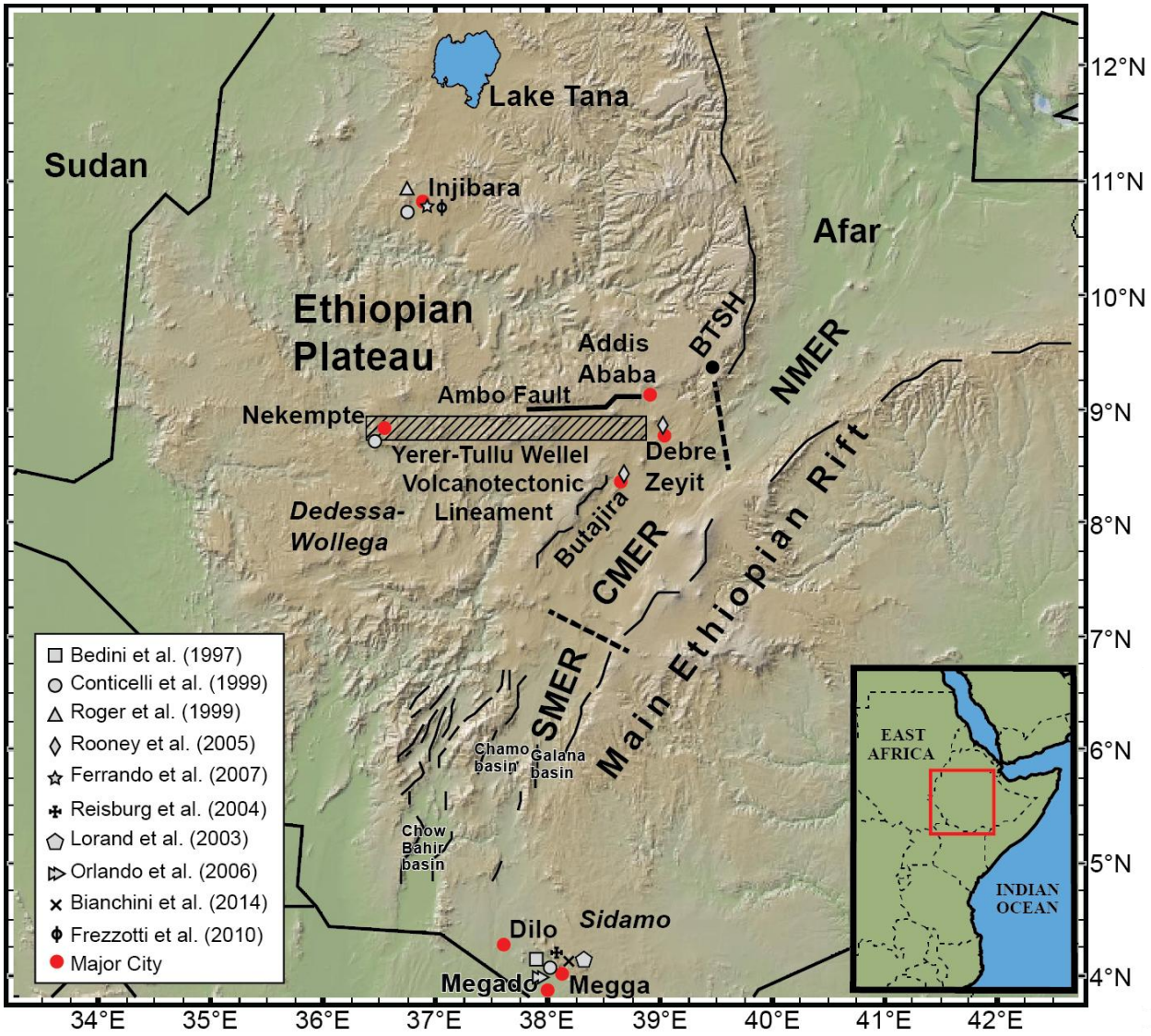

Location of the Main Ethiopian Rift (MER) and regional xenoliths studies from Injibara, Nekempte, Debre Zeyit, Butajira, Dilo, Megado, and Megga. Abbreviations listed in 'KEY TO ABBREVIATIONS'.

Figure 3 Lithospheric Modification of the YTVL

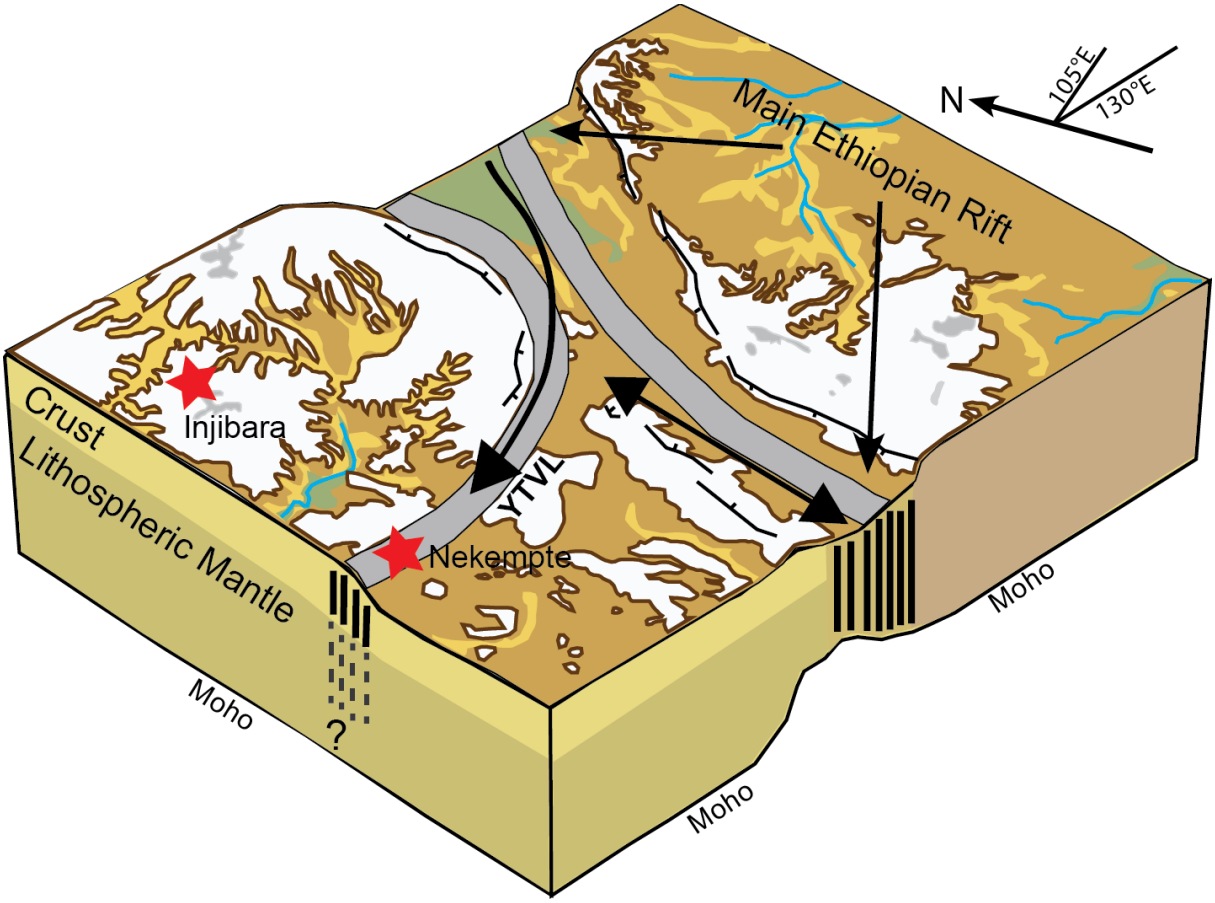

Modified from Keranen & Klemperer (2008). Figure depicts crustal modification along the YTVL with inferred modification extending into the SCLM. Figure not to scale.

Figure 4 Xenolith Petrography

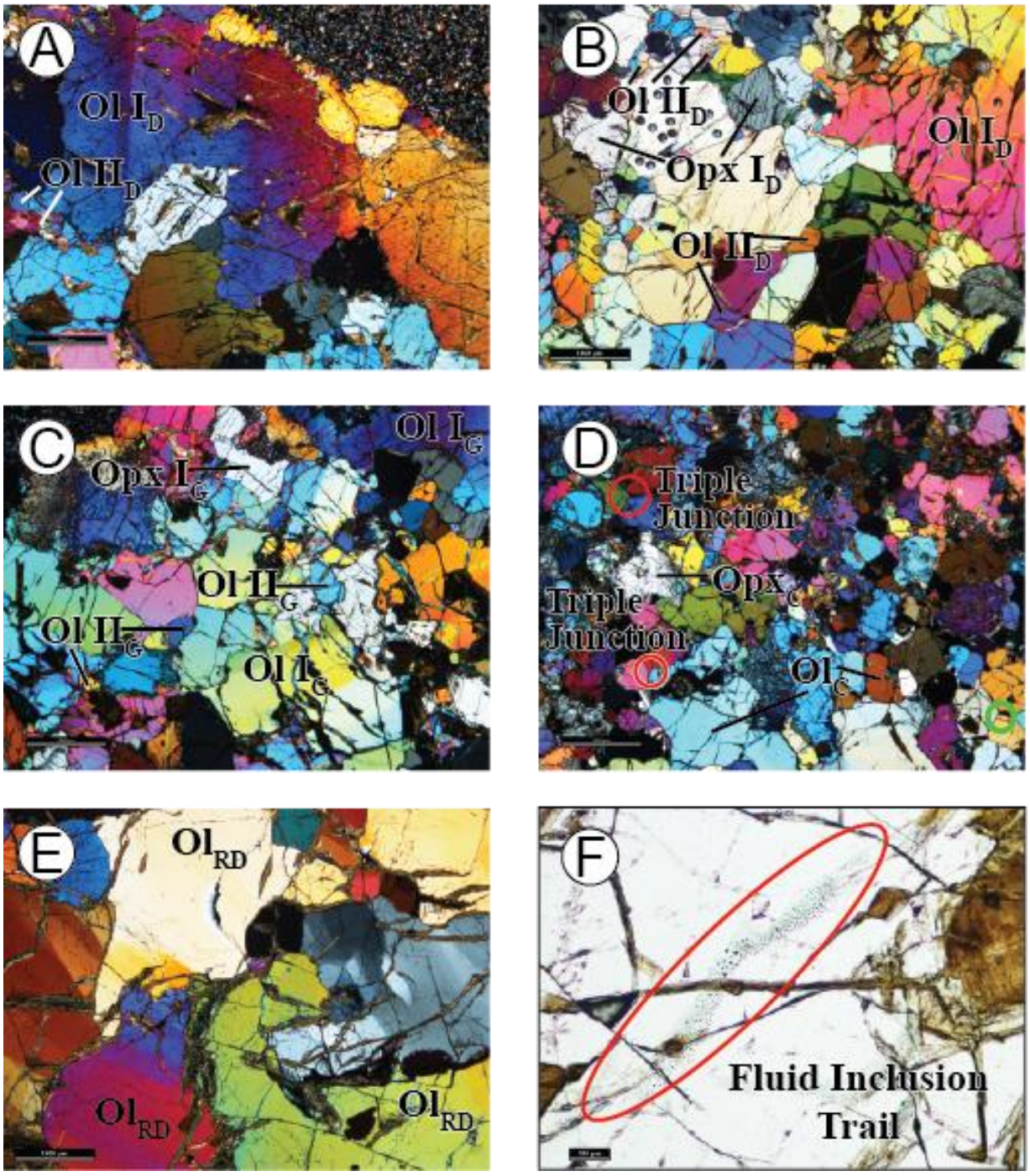

(a,b) Deformed xenoliths in XPL shows two generations of crystals; (c) Granular xenolith in XPL shows more recrystallization; (d) Cumulate xenolith in XPL consists of small euhedral to subhedral crystals. Note: triple junctions between crystals; (e) Dunite replacement xenoliths in XPL show large olivines; (f) fluid inclusion trail in a deformed xenoliths in PPL.

Figure 5 Comparison of Xenoliths

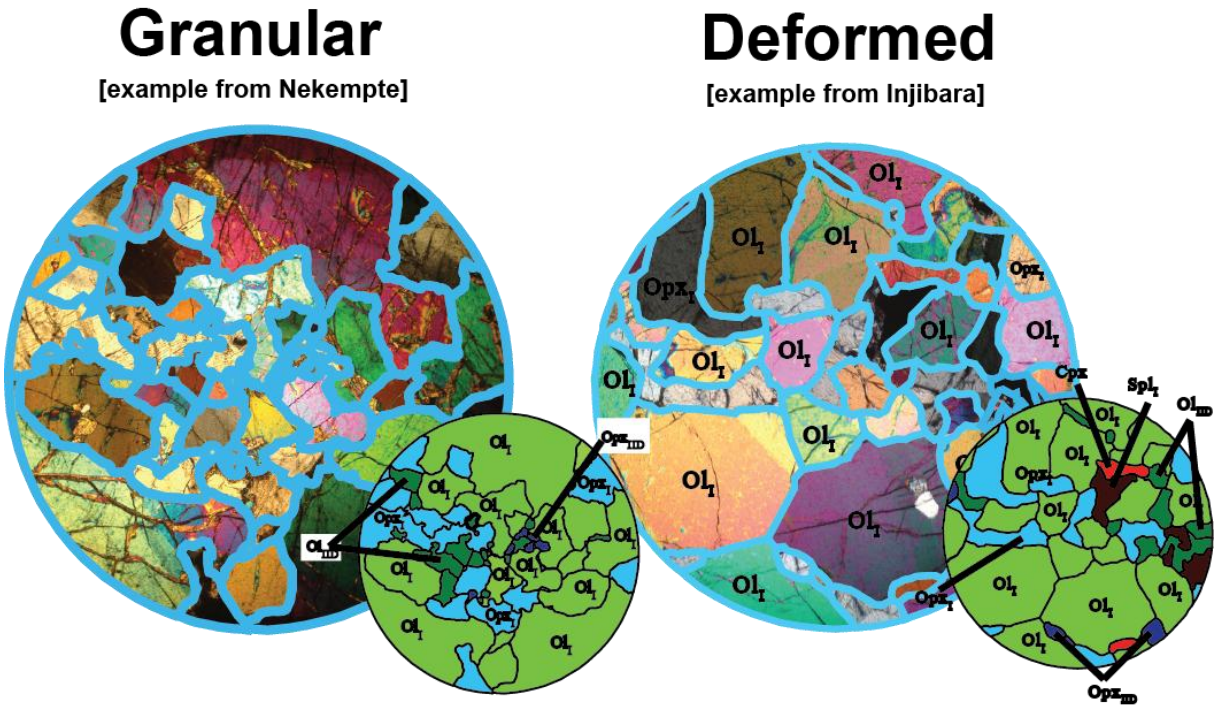

Comparison of deformed versus granular xenoliths. Example of granular xenoliths from Nekempte compared to deformed xenolith from Injibara, Ethiopia. Note that the granular xenoliths from Nekempte contain more second generation crystals indicating recrystallization.

Figure 6 Olivine Major and Minor Element Chemistry

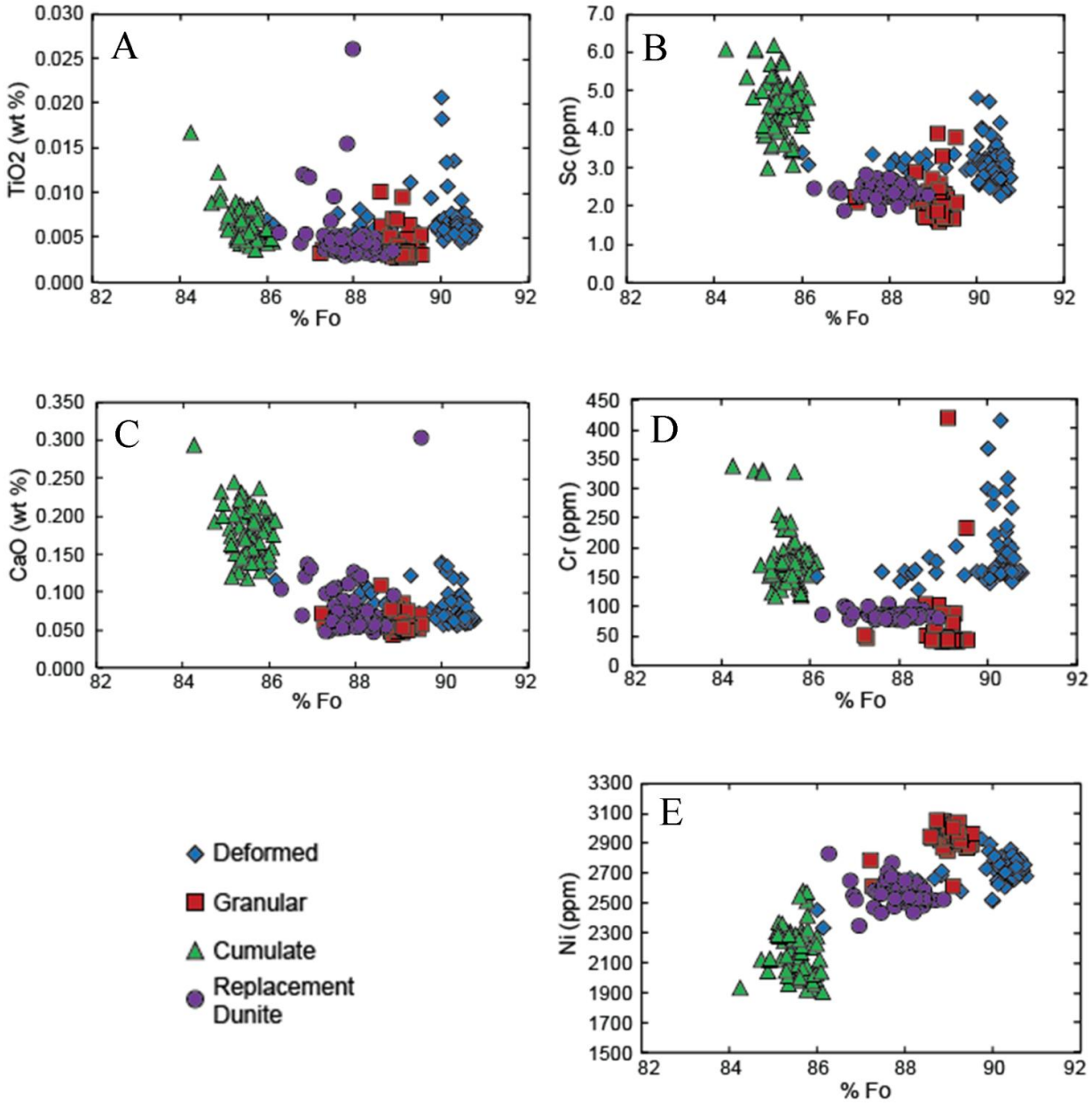

Olivine major and minor element chemistry for TiO_2, CaO_2, Sc, Cr, and Ni versus % forsterite (% Fo).

Figure 7 Orthopyroxene Major and Minor Element Chemistry

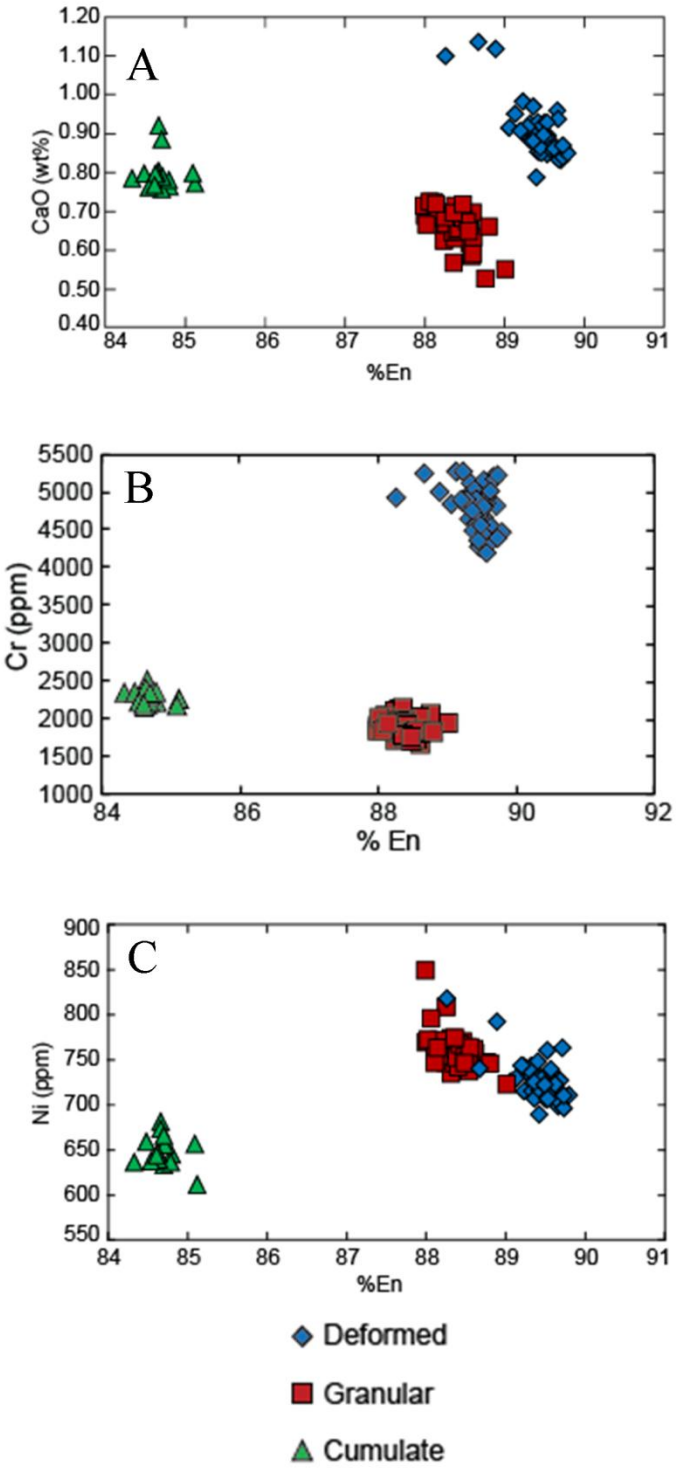

Orthopyroxene major and minor element chemistry for CaO_2, Cr, and Ni versus % enstatite (% En).

Figure 8 Spinel Major Element Chemistry

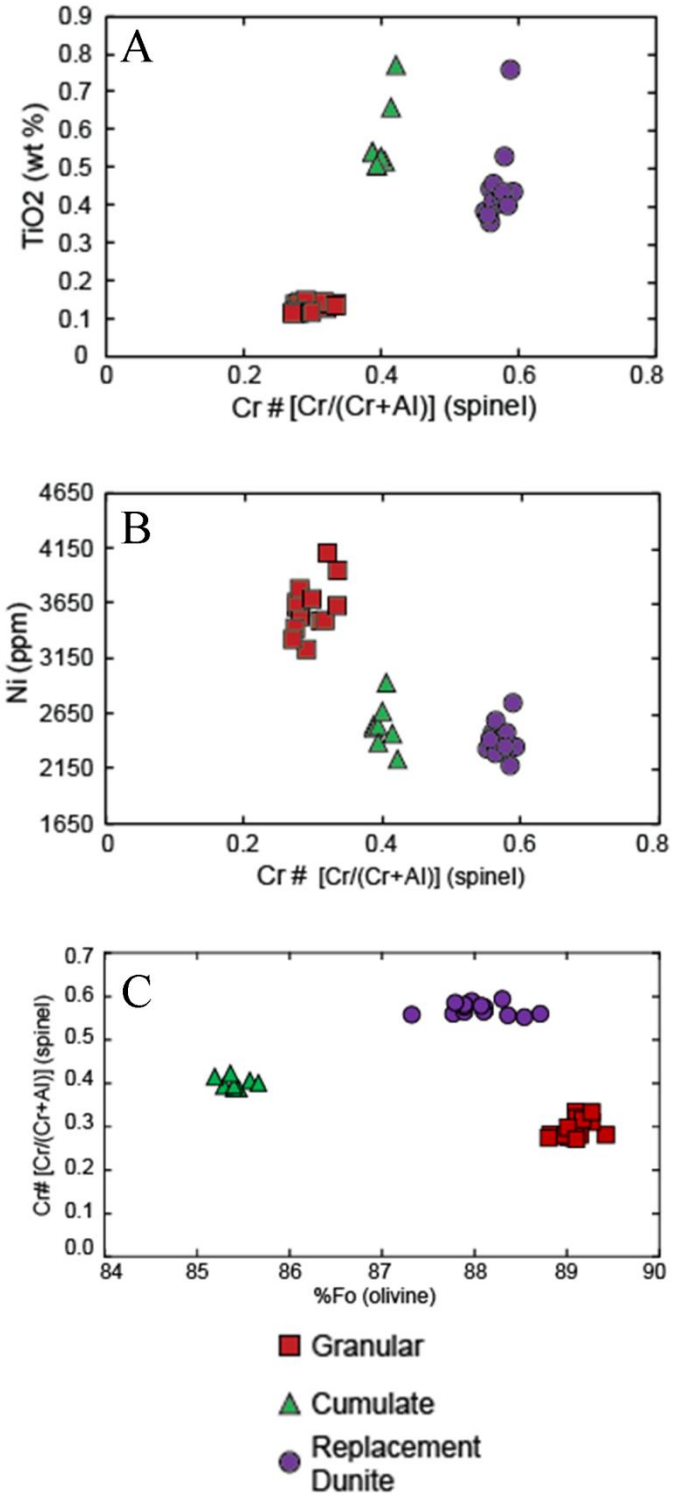

(a,b) Spinel major and minor element chemistry for TiO_2 and Ni versus Cr# [Cr/(Cr+Al)] in spinel(% Fo); (c) Cr# [Cr/(Cr+Al)] in spinel versus % forsterite (% Fo) in olivine.

Figure 9 Orthopyroxene Trace Element Chemistry

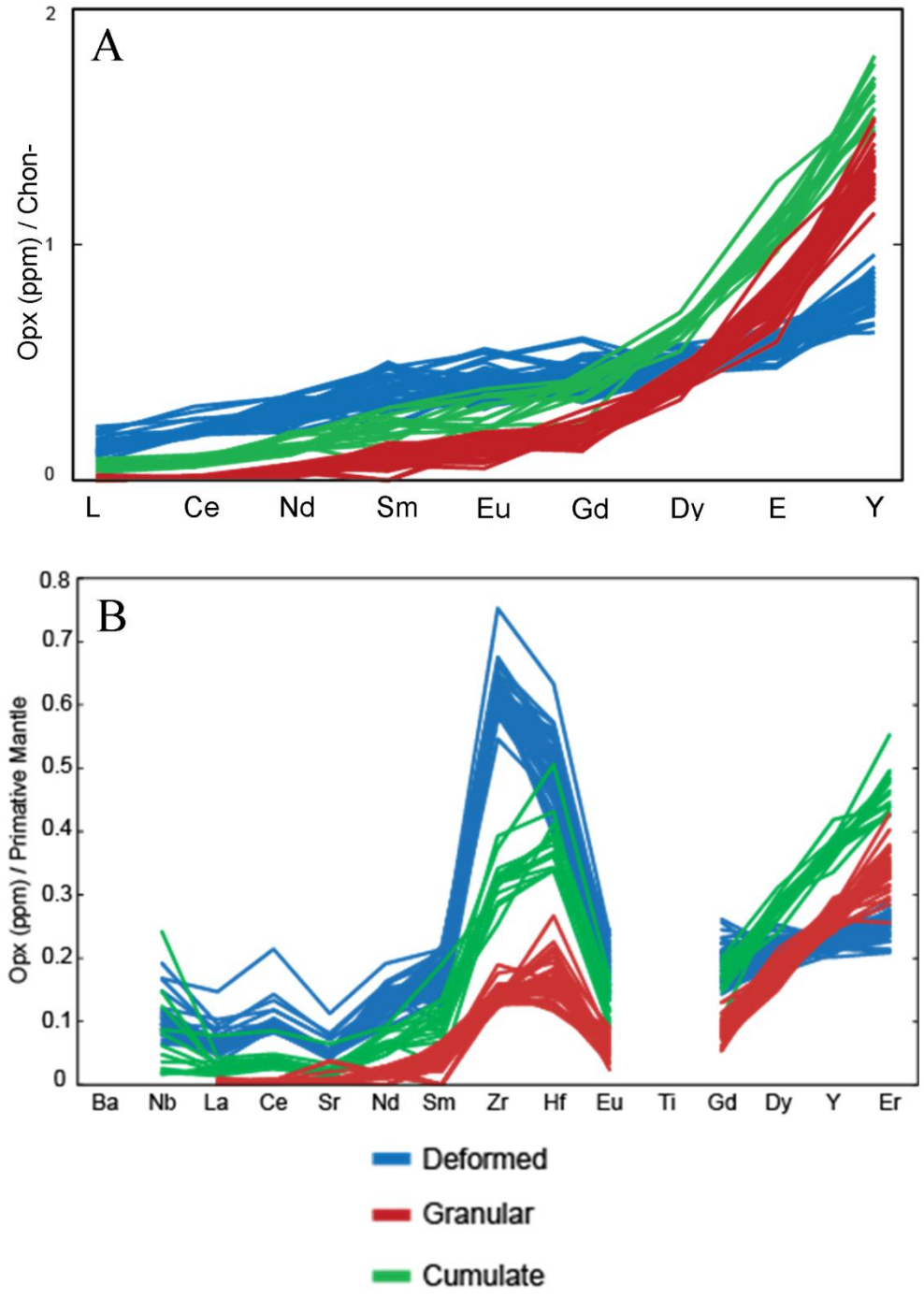

(a) Chondrite normalized trace element abundances in orthopyroxene for the deformed, granular, and cumulate xenoliths. (b) Primitive mantle (PM) normalized trace element chemistry in orthopyroxene for the deformed, granular, and cumulate xenoliths. Chondrite and primitive mantle values taken from Sun & McDonough, (1989).

Figure 10 Clinopyroxene Trace Element Chemistry

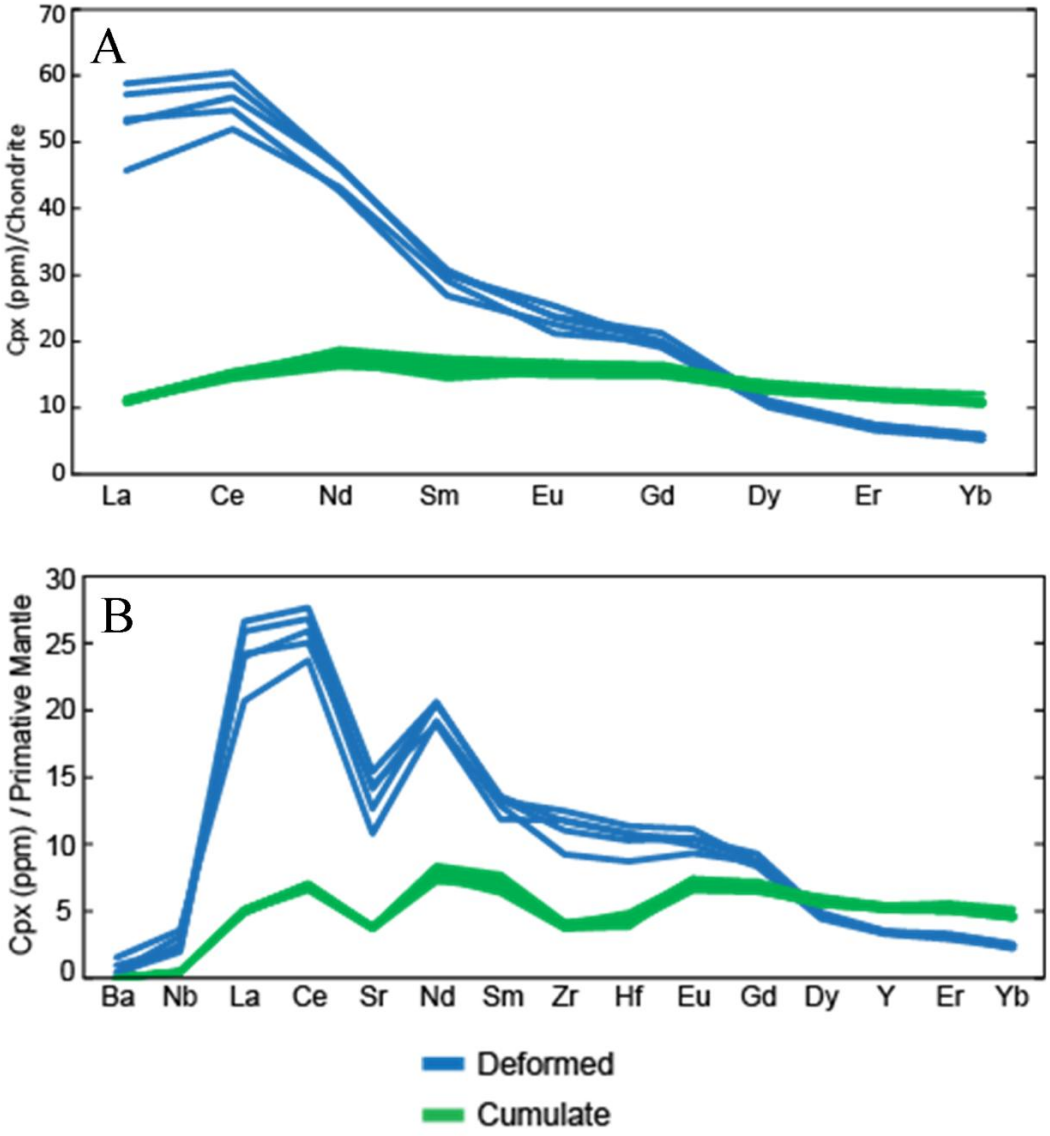

(a) Chondrite normalized trace element chemistry in clinopyroxene for the deformed and cumulate xenolith. (b) Primitive mantle (PM) normalized trace element chemistry in clinopyroxene for the deformed and cumulate xenolith. Chondite and primitive mantle values taken from Sun & McDonough, 1989.

Figure 11 Xenolith Thermobarometry

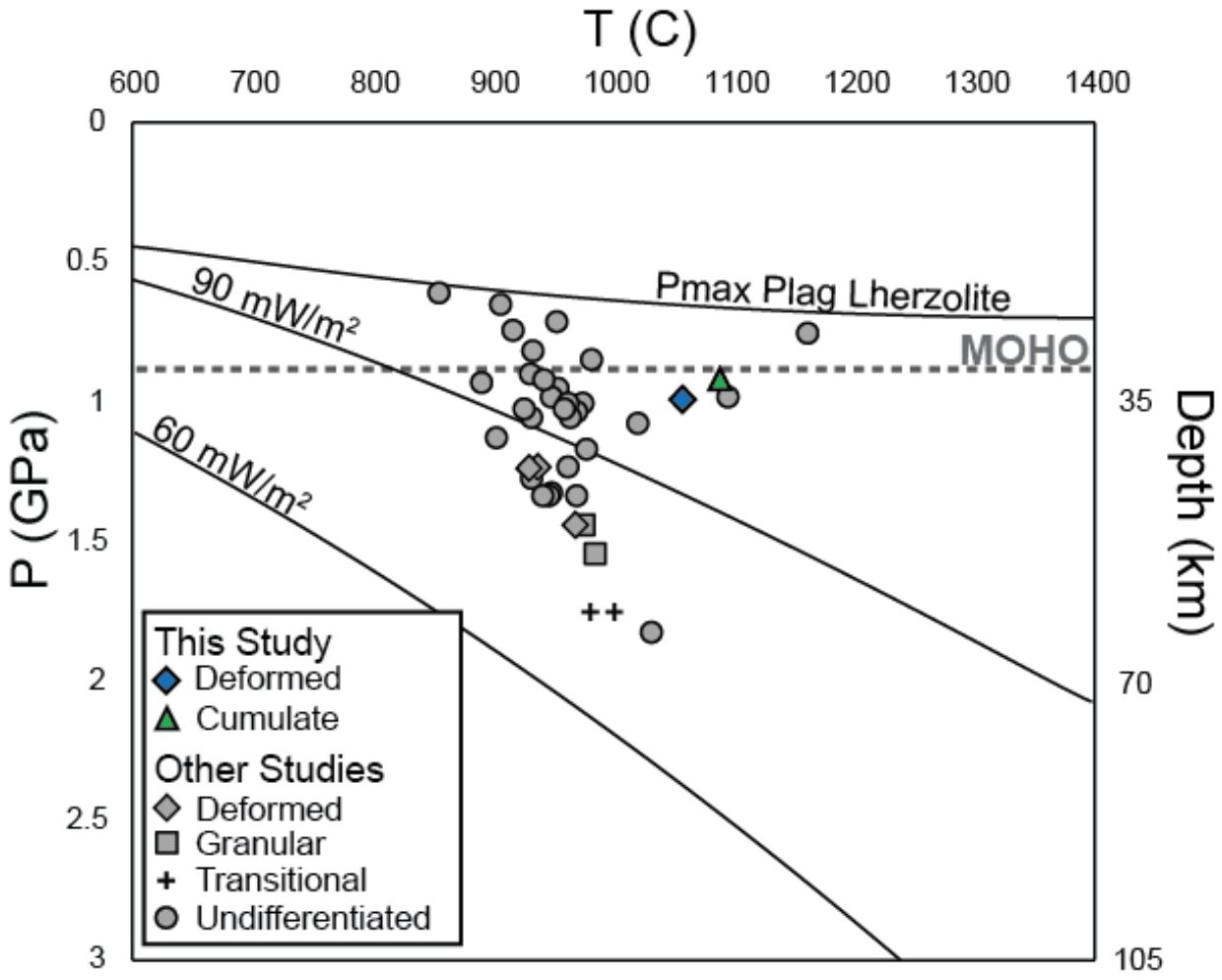

P– T thermobarometry data from this study and other regional data from deformed, granular, transitional, and undifferentiated xenoliths at Dedessa, Megado/Dilo, Injibara, West Injibara, Kishb, Mer-awi, and Megga locations. Thermobarometry data from this study were calculated with the two-pyroxene method from Putirka, (2008) and are shown in **Table 6 Regional Thermobarometry**. Standard error for temperature and pressure are 58° C and 2.8 kbar, respectively.

Figure 12 Zr/Hf Ratio Chemistry

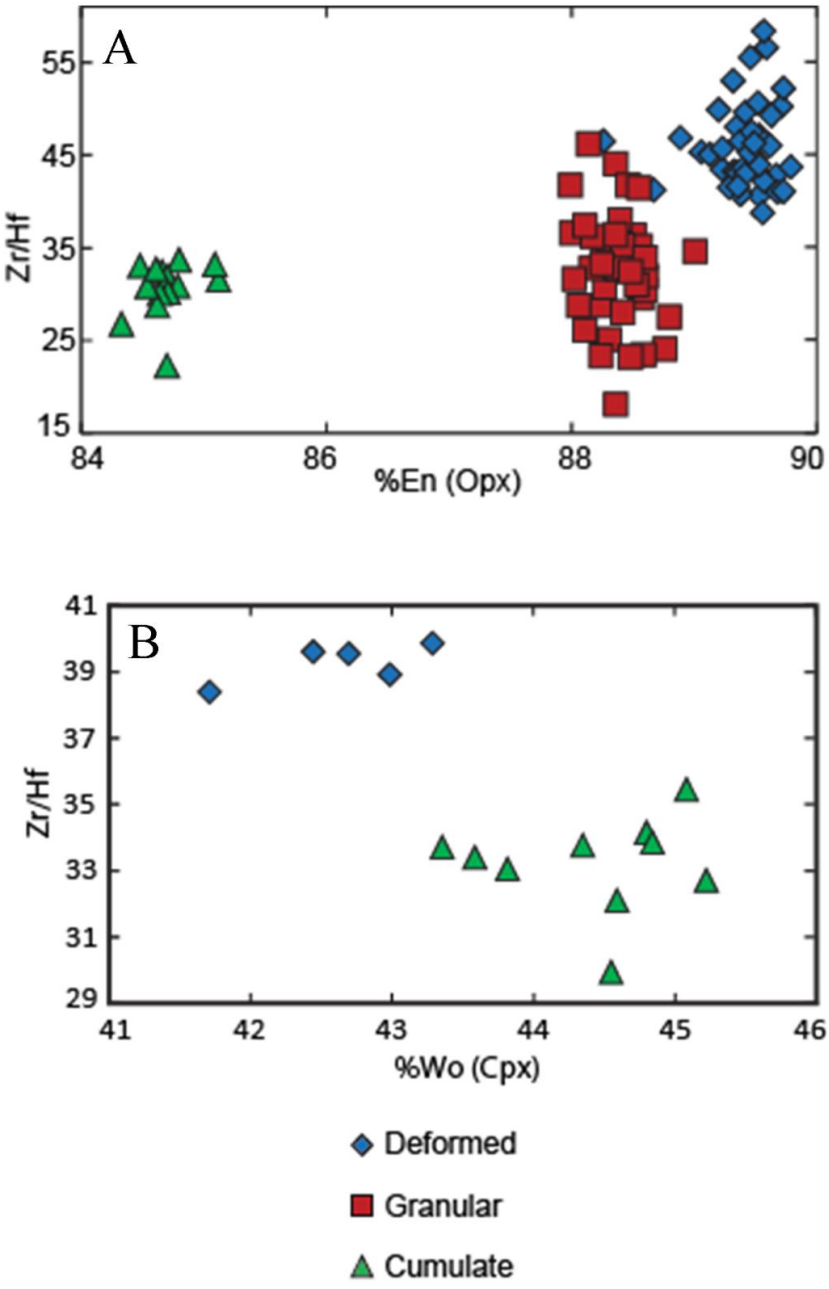

(a) Zr/Hf versus % Enstatite (% En) in orthopyroxene; and (b) Zr/Hf versus % wollastonite (% Wo) in orthopyroxene. In both cases, the deformed xenoliths display higher Zr/Hf ratio compared to other types.

Figure 13 Focused Melt Channel Model

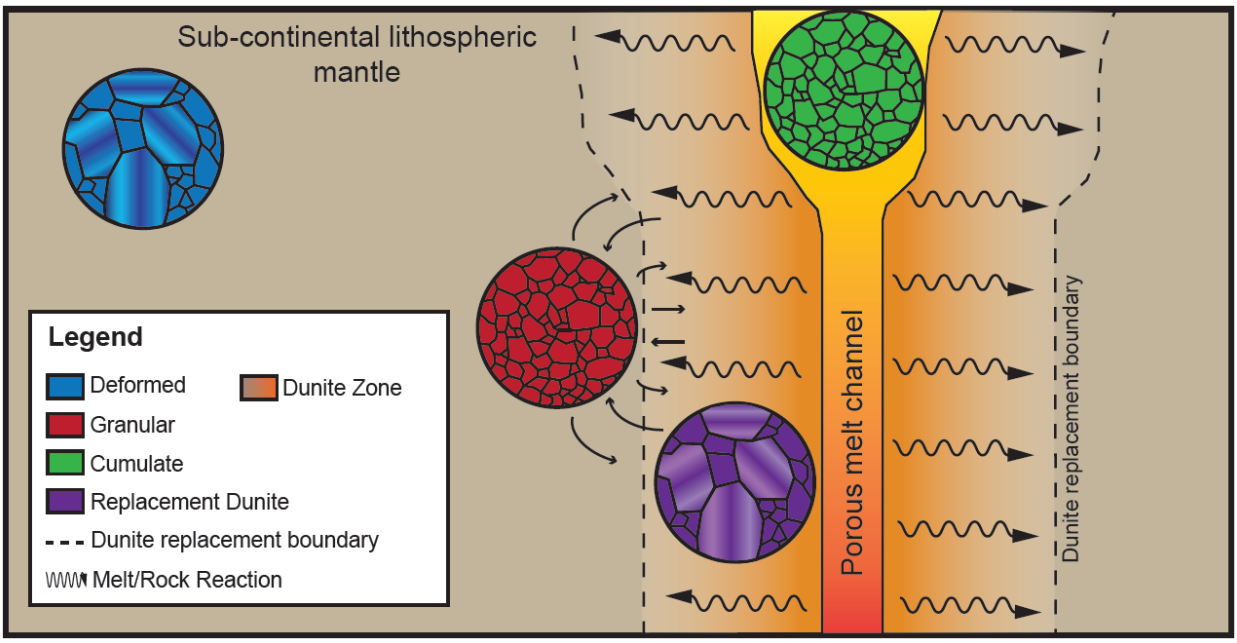

Focused melt channel model shows the relative position of each xenolith type in relation to the focused melt channel. Chemical exchange is allowed in the granular and replacement dunite xenoliths while the deformed xenoliths remains un-reactive with the melt channel. The cumulate xenolith represents a remnant of the melt channel as it cools and crystallizes.

APPENDIX C

CALIBRATION STANDARDS

Table 7 Calibration Standards

Standard	SiO_2 wt%	TiO_2 wt%	Al_2O_3 wt%	FeO wt%	MnO wt%	MgO wt%	CaO wt%	Na_2O wt%	K_2O wt%	Sc ppm	V ppm	Cr ppm	Co ppm	Ni ppm	Cu ppm	Zn ppm	Ga ppm
JB1a	52.41	1.28	14.45	8.145	0.148	7.83	9.31	2.73	1.4	28.3	197	414	38.7	140	N/A	N/A	18
BHVO-1	49.8	2.75	13.7	11.16	0.17	7.22	11.4	2.3	0.53	31.3	316	289	45.5	121	N/A	N/A	21
NIST 612	--	--	--	--	--	--	--	13.7	--		--	--	--	--	--	--	--
GSD-1G	--	--	--	13.3	--	--	--	--	--	51	--	--	--	--	--	--	54
SY-2	--	--	--	--	0.32	--	--	8.94	4.45		--	--	--	--	--	--	--
STM-1	--	--	18.4	--	--	--	--	--	4.28		--	--	--	--	--	--	--
PCC-1	--	--	--	--	--	43.43	--	--	--	--	--	2828	110	2380	--	--	--
DTS-1	--	--	--	--	--	49.59	--	--	--	--	--	3990	137	2360	--	--	--
JA2	--	--	--	--	--	--	--	--	--	--	--	450	--	--	--	--	--
NKT-1G	--	3.92	--	12	--	14.2	13.4	--	--	--	--	--	61.4	--	--	--	--
BIR-1	--	--	--	--	--	--	13.4	--	--	--	--	--		173	--	--	--
BIR-1G	--	--	--	--	--	--	13.3	--	--	--	--	--	--	178	--	--	--
TB-1G	--	--	--	--	--	--	--	--	4.52	--	--	--	--	--	--	--	--
BCR-2G	--	--	--	12.51	--	--	--	--	--	--	425	--	--	--	--	--	--

Standard	Rb ppm	Sr ppm	Y ppm	Zr ppm	Nb ppm	Ba ppm	La ppm	Ce ppm	Nd ppm	Sm ppm	Eu ppm	Gd ppm	Dy ppm	Er ppm	Yb ppm	Hf ppm
JB1a	38.4	441	23.2	140	28.1	495	38.1	66.2	26.3	5.1	1.48	4.93	4.08	2.19	2.13	3.6
BHVO-1	9.49	396	26.2	174	18.5	134	15.5	38.1	24.7	6.14	2.06	6.25	5.3	2.51	2	4.43
NIST 612	--	--	--	--	--	--	--	--	--	--	--	--	--	--	--	--
GSD-1G	--	--	--	--	43.4	--	--	--	--	47	41.2	49	51.2	38.5	50.6	39.5
SY-2	217	700	133	309	--	--	75	175	--	16.1	--	17	18	--	17	--
STM-1	--	--	--	1283	260		150	259	79	--	3.35	--	--	--	--	29.6
PCC-1	--	--	--	--	--	--	--	--	--	--	--	--	--	--	--	--
DTS-1	--	--	--	--	--	--	--	--	--	--	--	--	--	--	--	--
JA2	--	--	--	--	--	--	--	--	--	--	--	--	--	--	--	--
NKT-1G	--	1203	--	286	95.9	724	64.2	127	61.7	--	3.85	--	--	--	--	--
BIR-1	--	--	--	--	--	--	--	--	--	--	--	--	--	--	--	--
BIR-1G	--	--	--	--	--	--	--	--	--	--	--	--	--	--	--	--
TB-1G	--	1363	--	243	--	924.9	--	89.7	--	--	--	--	--	--	--	--
BCR-2G	--	--	--	--	--	--	--	--	--	--	--	--	--	--	--	--

Values compiled from Georem database
Known complex surface reaction effects during fusion in fused powders. Cu and Zn only reported for precision estimation purposes
-- = Not Analyzed

JB1a Geol Surv Japan basalt powder, fused in our labs
BHVO-1 USGS basalt powder, fused in our labs
NIST 612 NBS synthetic Na-Si glass dped with trace elements
GSD-1G USGS synthetic basalt glass doped with trace elements
SY-2 Geol Surv Canada syenite powder, fused in our labs
STM-1 USGS syenite powder, fused in our labs
PCC-1 USGS dunite
DTS-1 USGS harzburgite
JA2 Geol Surv Japan andesite powder, fused in our labs
NKT-1G USGS nephelinite glass
BIR-1 USGS basalt powder, fused in our labs
BIR-1G USGS basalt glass
TB-1G USGS basalt glass
BCR-2G USGS basalt glass

Known geochemical values for select calibration standards.

APPENDIX D

STANDARD DEVIATION OF SELECT CALIBRATION STANDARDS

Table 8 Standard Deviation of Select Calibration Standards

	Standard	SiO_2 wt%	TiO_2 wt%	Al_2O_3 wt%	FeO wt%	MnO wt%	MgO wt%	CaO wt%	Sc ppm	V ppm	Cr ppm	Co ppm	Ni ppm	Cu ppm	Zn ppm	Ga ppm	Rb ppm
Batch 1 (5-Dec-14)	DTS-1**	30.26	0.002	0.127	6.134	0.092	37.48	0.078	2.426	7.270	3,894.55	102.72	1,753.41	11.27	36.46	0.000	0.069
	PCC-1	42.25	0.004	0.629	7.736	0.114	43.49	0.522	8.909	30.71	2,828.78	113.36	2,330.07	12.11	44.32	0.499	0.068
Batch 2 (9-Dec-14)	DTS-1	40.70	0.003	0.175	8.392	0.121	50.22	0.110	3.297	10.27	4,224.33	141.69	2,438.31	16.20	46.47	--	0.118
	PCC-1	41.25	0.005	0.603	7.749	0.117	43.68	0.485	8.122	29.99	2,817.87	115.45	2,361.84	13.04	42.96	0.587	0.095
Batch 3 (1-Apr-15)	DTS-1	40.22	0.003	0.169	8.177	0.121	49.80	0.105	3.080	10.26	4,818.75	140.84	2,394.30	8.747	35.20	--	0.130
	PCC-1	41.90	0.004	0.630	7.408	0.113	44.21	0.525	8.176	32.05	2,923.83	111.64	2,293.13	17.94	30.60	0.460	0.035
Batch 4 (29-Apr-15)	DTS-1	40.60	0.003	0.176	7.820	0.118	49.10	0.111	3.413	10.28	4,226.13	137.74	2,392.52	9.040	39.79	0.409	0.120
	PCC-1	40.71	0.005	0.614	7.275	0.114	43.23	0.495	8.320	29.99	2,777.08	111.40	2,352.81	19.54	38.90	0.609	0.016
DTS-1 Standard Deviation		0.251	0.000	0.004	0.289	0.002	0.565	0.003	0.169	0.012	342.67	2.079	25.937	4.221	5.667	--	0.006
PCC-1 Standard Deviation		0.685	0.000	0.013	0.238	0.002	0.413	0.020	0.361	0.971	62.084	1.875	30.627	3.640	6.179	0.071	0.035

	Standard	Sr ppm	Y ppm	Zr ppm	Nb ppm	Ba ppm	La ppm	Ce ppm	Nd ppm	Sm ppm	Eu ppm	Gd ppm	Dy ppm	Er ppm	Yb ppm	Hf ppm
Batch 1 (5-Dec-14)	DTS-1**	0.238	0.028	0.108	0.018	0.421	0.026	0.057	0.028	-0.005	0.004	-0.003	0.009	0.003	0.012	0.002
	PCC-1	1.183	0.098	0.141	0.007	1.255	0.045	0.060	0.014	0.018	0.004	0.019	0.011	0.011	0.031	0.007
Batch 2 (9-Dec-14)	DTS-1	0.329	0.046	0.229	0.020	0.583	0.028	0.065	0.026	0.005	0.000	0.004	0.007	0.004	0.010	0.001
	PCC-1	1.139	0.091	0.115	0.014	1.206	0.037	0.055	0.025	0.007	-0.001	0.006	0.014	0.014	0.034	0.000
Batch 3 (1-Apr-15)	DTS-1	0.372	0.024	0.152	0.012	0.453	0.021	0.058	0.025	0.007	0.002	0.004	0.007	0.005	0.011	0.007
	PCC-1	0.477*	0.086	0.207	0.011	1.012	0.037	0.063	0.022	-0.003	-0.002	0.006	0.013	0.014	0.021	0.004
Batch 4 (29-Apr-15)	DTS-1	0.314	0.036	0.209	0.017	0.521	0.022	0.064	0.028	0.009	0.004	0.006	0.004	-0.002	0.014	0.001
	PCC-1	0.497*	0.070	0.672	0.014	1.073	0.036	0.072	0.031	0.008	-0.005	0.014	0.007	0.017	0.026	0.005
DTS-1 Standard Deviation		0.030	0.011	0.040	0.004	0.065	0.004	0.004	0.002	0.002	0.002	0.001	0.002	0.004	0.002	0.003
PCC-1 Standard Deviation		0.031	0.012	0.262	0.003	0.113	0.004	0.007	0.007	0.009	0.004	0.006	0.003	0.002	0.005	0.003

* = standard disk may have had Sr contamination
** = Failed ablation. Vaules omitted from standard deviation calculations
-- = Not available

Batch precision analysis of select calibration standards.

.

REFERENCES

REFERENCES

Abebe, T., Mazzarini, F., & Manetti, P. (1998). "The Yerer-Tullu Wellel Volcanotectonic Lineament: a transtensional structure in central Ethiopia and the associated magmatic activity." Journal of African Earth Sciences **26**: 135-150.

Abebe, T. (2014). "The occurrence of a complete continental rift type of volcanic rocks suite along the Yerer-Tullu Wellel Volcano Tectonic Lineament". Journal of African Earth Sciences. **99**: 374-385.

Agostini, A., Bonini, M., Corti, G., Sani, F., Mazzarini, F. (2011). "Fault architecture in the Main Ethiopian Rift and comparison with experimental models: Implications for rift evolution and Nubia-Somalia kinematics". Earth and Planetary Science Letters. **301**. 479-492.

Anderson, D. L. (2007). New theory of the Earth. Cambridge University Press.

Aulbach, S., O'Reilly, S. Y., Pearson, N. J. (2011). "Constraints from eclogite and MARID xenoliths on origins of mantle Zr/ Hf-Nb/Ta variability" Contrib. Mineral. Petrol. **162**: 1047-1062.

Bailey, D. K. (1982). "Mantle metasomatism: continuing chemical change within the Earth." Nature **296**: 525-530.

Beccaluva, L., Bianchini, G., Natali, C., Siena, F. (2009). "Continental flood basalts and mantle plumes: a case study of the Northern Ethiopian Plateau." Journal of Petrology **50** (7): 1377-1403.

Bédard, J. H., Hébert, R. (1998). "Formation of chromitites by assimilation of crustal pyroxenites and gabbros into peridotitic intrusions: North Arm Mountain massif, Bay of Islands ophiolite, Newfoundland, Canada" Journal of Geophysical Research **103**, *B3*: 5165-5184.

Bedini, R. M., Bodinier, J. -L., Dautria, J. -M., Morten, L. (1997). "Evolution of LILE-enriched small melt fractions in the lithospheric mantle: a case study from the East Africa Rift." Earth and Planetary Science Letters **153**: 67-83.

Bedini, R. M., Bodinier, J. -L. (1999). "Distribution of incompatible trace elements between the constituents of spinel peridotite xenoliths: ICP-MS data from the East African Rift." Geochimica et Cosmochimica Acta **63**(22): 3883- 3900.

Begg, G.C., Griffin, W. L., Natapov, L. M., O'Reilly, S. Y., Grand, S. P., O'Neill, C. J., Hronsky, J. M. A., Poudjom Djomani, Y., Swain, C. J., Deen, T., Bowden, P. (2009). "The lithospheric architecture of Africa: Seismic tomography, mantle petrology, and tectonic evolution" Geosphere, **5** (1): 23-50.

Bell, K., & Tilton, G. R. (2001). "Nd, Pb and Sr isotopic compositions of East African carbonatites: evidence for mantle mixing and plume inhomogeneity". Journal of Petrology, **42**(10), 1927-1945.

Bentor, Y. (1985). "The crustal evolution of the Arabo-Nubian Massif with special reference to the Sinai Peninsula". Precambrian Research **28**: 1-74.

Bianchini, G., Beccaluva, L., Bonadiman, C., Nowell, G., Pearson, G., Siena, F., Wilson, M. (2007). "Evidence of diverse depletion and metasomatic events in harzburgite-lherzolite mantle xenoliths from the Iberian plate (Olot, NE Spain): Implications for lithosphere accretionary processes". Lithos. **94**, 25-45.

Bianchini, G., Bryce, J.C., Blichert-Toft, J., Beccaluva, L., Natali, C. (2014). “Mantle dynamics and secular variations beneath the East Africa Rift: Insights from peridotite xenoliths (Mega, Ethiopia)” Chemical Geology. **386**. 49-58.

Bodinier, J. L., Vasseur, G., Vernieres, J., Dupuy, C., Fabries, J. (1990). “Mechanisms of mantle metasomatism: Geochemical evidence from the Lherz Orogenic Peridotite” Journal of Petrology **31**(3) 597-628.

Bodinier, J. L., Menzies, M. A., Thirlwall, M. F. (1991). “Continental to oceanic mantle transition- REE and Sr- Nd isotopic geochemistry of the Lanzo Lherzolite Massif” Journal of Petrology **Special Lherzolites Issue**: 191-210.

Bonini, M., Corti, G., Innocenti, F., Manetti, P., Mazzarini, F., Abebe, T., Pecskay, Z. (2005). “Evolution of the Main Ethiopian Rift in the frame of Afar and Kenya rifts propagation. Tectonics. **24**: TC1007.

Bosworth, W., Huchon, P., McClay, K. (2005). “The Red Sea and Gulf of Aden basins” Journal of African Earth Sciences **43**: 334-378.

Buck, W.R. (2006). “The role of magma in the development of the Afro-arabian Rift System. In: Yirgu, G., Ebinger, C. J., Maguire, P. K. H. (Eds.), The Afar Volcanic Province within the East African Rift System. Geol. Soc. Spec. Publ., **259**. 43-54.

Burke, K. (1996). "The African plate." South African Journal of Geology **99**(4): 341-409.

Chesley, J. T., Rudnick, R. L., Lee, C. T. (1999). “Re-Os systematic of mantle xenoliths from the East African Rift: Age, structure, and history of the Tanzanian craton”. Geochimica et Cosmochimica Acta, **63** (7): 1203-1217.

Chorowicz, J. (2005). "The East African rift system." Journal of African Earth Sciences **43**: 379-410.

Collier, M. L. & Kelemen, P. B. (2010). “The case for reactive crystallization at mid-ocean ridges” Journal of Petrology **51** (9): 1913-1940.

Contecelli, S., Sintoni, M. F., Abebe, T., Mazzarini, F., & Manetti, P. (1999). "Petrology and geochemistry of ultramafic xenoliths and host lavas from the Ethiopian volcanic province: an insight into the upper mantle under Eastern Africa." Acta Vulcanologica **11**: 143-159.

Corti, G. (2009). "Continental rift evolution: From rift initiation to incipient break-up in the Main Ethiopian Rift, East Africa." Earth-Science Reviews **96**: 1-53.

Corti, G. (2012). "Evolution and characteristics of continental rifting: Analog modeling-inspired view and comparison with examples from the East African Rift System” Tectonophysics. 522-523, 1-33.

Courtillot, V., Jaupart, C., Manighetti, I., Tapponnnier, P., Besse, J. (1999). “On causal links between flood basalts and continental breakup”. Earth and Planetary Science Letters. **166**. 177-195.

Cutten, H. (2002). “The Mozambique Belt, eastern Africa-tectonic evolution of Gondwanaland amalgamation and Rodinia breakup”. In *GEOLOGICAL SOCIETY OF AUSTRALIA ABSTRACTS* (**67**: 109-109). Geological Society of Australia; 1999.

Daines, M. J., & Kohlstedt, D. L. (1994). “The transition from porous to channelized flow due to melt/rock reaction during melt migration” Geophysical Research Letters **21** (2): 145-148.

Danyushevski, L. V., Perfit, M. R., Eggins, S. M., Falloon, T. J. (2003). “Crustal origin for coupled ‘ultra-depleted’ and ‘plagioclase’ signatures in MORB olivine-hosted melt inclusions: evidence from the Siqueiros Transform Fault, East Pacific Rise” Contib. Mineral. Petrol. **144**: 619-637.

Danyushevski, L. V., Leslie, R. A., Crawford, A. J., Durance, P. (2004). “Melt inclusions in primitive olivine phenocrysts: the role of localized reaction processes in the origin of anomalous compositions” Journal of Petrology **45** (112): 2531-2553.

De Hoog, J. C. M., Gall, L., Cornell, D. H. (2010). “Trace-element geochemistry of mantle olivine and application to mantle petrogenesis and geothermobarometry” Chemical Geology **270**: 196-215.

Doucet, L. S., Peslier, A. H., Ionov, D. A., Brandon, A. D., Golovin, A. V., Goncharov, A. G., Ashchepkov, I. V. (2014). "High water contents in the Siberian cratonic mantle linked to metasomatism: an FTIR study of Udachnaya peridotite xenoliths." Geochimica et Cosmochimica Acta. doi: http://dx.doi.org/10.1016/j.gca.2014.04.011

Dupuy, C., Liotard, J. M., Dostal, J. (1992). “Zr/Hf fractionation in intraplate basaltic rocks: Carbonitite metasomatism in the mantle source” Geochimica et Cosmochimica Acta **56**: 2417-2423.

Ebinger, C.J., Casey, M., (2001). “Continental breakup in magmatic provinces: an Ethiopian Example”. Geology **29**, 527–530.

Elkins-Tanton, L. T. (2005). “Continental magmatism caused by lithospheric delamination”. Geological Society of America Special Paper. **388**: 449-461.

Ferrando, S., Frezzoti, M. L., Neumann, E. -R., De Astis, G., Peccerillo, A., Dereje, A., Gezahegn, Y. ,Teklewold, A. (2008). "Composition and thermal structure of the lithopshere beneath the Ethiopian plateau: evidence from mantle xenoliths in basanites, Injibara, Lake Tana Province." Journal of Mineralogy and Petrology **93**: 47-78.

Foley, S. F., Prelevic, D., Rehfeldt,T., Jacob, D. E. (2013). “Minor and trace elements in olivines as probes into early igneous and mantle melting processes” Earth and Planetary Science Letters **363**: 181-191.

Frey, F. A., 1984. Rare earth element abundances in upper mantle rocks. In: Henderson, P. (ed.). *Rare Earth Element Geochemistry*. Amsterdam: Elsevier, 153-203.

Frezzotti, M. L., Ferrando, S., Peccerillo, A., Petrellie, M., Tecce, F., Perucchi, A. (2010). "Chlorine-rich metasomatic H_2O-CO_2 fluids in amphibole-bearing peridotites from Injibara (Lake Tana region, Ethiopian plateau): Nature and evolution of volatiles in the mantle of a region of continental flood basalts." Geochimica et Cosmochimica Acta **74**: 3023-3039.

Furman, T. (1995). “Melting of metasomatized subcontinental lithosphere: undersaturated mafic lavas from Rungwe, Tanzania” Contrib. Mineral. Petrol. **122**: 97-115.

Furman, T. (2007). "Geochemistry of East African Rift basalts: An overview." Journal of African Earth Sciences **48**: 147-160.

Griffin, W. L., O'Reilly, S. Y., Afonso, J. C., Begg, G. C. (2009). "The composition and evolution of lithospheric mantle: A re-evaluation and its tectonic implications." Journal of Petrology **50**: 1185-1204.

Gueydan, F., Precigout, P. (2013). "Modes of continental rifting as a function of ductile strain localization in the lithospheric mantle." Tectonophysics. doi: 10.1016/j.tecto.2013.11.029

Guirard, R., Bosworth, W., Thierry, J., Delplanque, A. (2005). "Phanerozoic geological evolution of Northern and Central Africa: An overview." Journal of African Earth Sciences **43**: 83-143.

Havlin, C., Parmentier, E. M., Hirth, G. (2013). "Dike propagation driven by melt accumulation at the lithosphere-asthenosphere boundary". Earth and Planetary Science Letters. **376**: 20-28.

Hellebrand, E., Snow, J. E., Dick, H. J. B., Hofmann, A. W. (2001). "Coupled major and trace elements as indicators of the extent of melting in mid-ocean-ridge peridotites" Nature **410**: 677-681.

Herzberg, C. (2011). "Identification of source lithology in the Hawaiian and Canary Islands: implications for origins" Journal of Petrology **52**, *1*: 113-146.

Hoffman, C., Courtillot, V., Feraud, G., Rochette, P., Yirgu, G., Ketefo, E., Pik, R. (1997). "Timing of the Ethiopian flood basalt event: Implications for plume birth and global change." Nature **389**: 838-841.

Holtzman, B. K., Groebner, N. J., Zimmerman, M. E., Ginsberg, S. B., Kohlstedt, D. L. (2003). "Stress-driven melt segregation in partially molten rocks" Geochemistry, Geophysics, Geosystems **4** (5): 1-26.

Huismans, R.S., Podladchikov, Y.Y., Cloetingh, S., (2001). "Transition from passive to active rifting: relative importance of asthenospheric doming and passive extension of the lithosphere". Journal of Geophysical Research-Solid Earth **106**, 11271–11291.

Huismans, R. S., & Beaumont, C. (2011). "Depth-dependent extension, two-stage breakup and cratonic underplating at rifted margins" Nature, **473** (7345): 74-78.

Ionov, D. A., Dupuy, C., O'Reilly, S. Y., Kopylova, M. G., Genshaft, Y. S. (1993). "Carbonated peridotite xenoliths from Spitsbergen: implications for trace element signature of mantle carbonate metasomatism" Earth and Planetary Science Letters **119**: 283-297.

Ionov, D. A., O'Reilly, S. Y., Genshaft, Y. S., Kopylova, M. G. (1996). "Carbonate-bearing mantle peridotite xenoliths from Spitsbergen: phase relationships, mineral compositions and trace-element residence" Contrib. Mineral Petrol. **125**: 375-392.

Ionov, D. A. (2007). "Compositional variations and heterogeneity in fertile lithospheric mantle: peridotite xenoliths in basalts from Tariat, Mongolia." Contrib Mineral Petrol **154**: 455-477.

Kaeser, B., Kalt, A., & Pettke, T. (2006). "Evolution of the lithospheric mantle beneath the Marsabit Volcanic Field (Northern Kenya): Constraints from textural, P-T and geochemical studies on xenoliths." Journal of Petrology **47**: 2149-2184.

Karato, S., Toriumi, M., Fujii, T. (1980). "Dynamic recrystallization of olivine single crystals during high-temperature creep". Geophysical Research Letters. **7**: (9), 649-652.

Katz, R. F., Spiegelman, M., Holtzman, B. (2006). "The dynamics of melt and shear localization in partially molten aggregates" Nature **442**: 676- 679.

Kawabata, H., Hanyu, T., Chang, Q., Kimura, J., Nichols, A. R. L., Tatsumi, Y. (2011). "The petrology and geochemistry of St. Helena alkali basalts: Evaluation of the oceanic crust-recycling model for HIMU OIB." Journal of Petrology **52**(4): 791-838.

Kay, R.W., Kay, S.M., (1993). "Delamination and delamination magmatism". Tectonophysics **219**, 177–189.

Keir, D., Bastow, I. D., Whaler, K.A., Daly, E., Cornwell, D. G., Hautot, S. (2009). "Lower crustal earthquakes near the Ethiopian rift induced by magmatic processes". Geochem. Geophys. Geosyst. **10**. Q0AB02, doi: 10.1029.2010TC002785.

Kelemen, P. B., Dick, H. J. B., Quick, J. E. (1992). "Formation of harzburgite by pervasive melt/rock reaction in the upper mantle" Nature **358**: 635-641.

Kelemen, P. B., & Dick, H. J. B. (1995). "Focused melt flow and localized deformation in the upper mantle: juxtaposition of replacive dunite and ductile shear zones in the Josephine peridotite, SW Oregon" Journal of Geophysical Research **100** (B1): 423-438.

Keranen, K., Klemperer, S.L. (2008). "Discontinuous and diachronous evolution of the Main Ethiopian Rift: Implications for development of continental rifts." Earth and Planetary Science Letters **265**: 96-111.

Kieffer, B., Arndt, N., Lapierre, H., Bastien, F., Bosch, D., Pecher, A., Yirgu, G., Ayalew, D., Weis, D., Jerram, D. A., Keller, F., Meugniot, C. (2004). "Flood and shield basalts from Ethiopia: Magmas from the African Superswell." Journal of Petrology **45** (4): 793-834.

Kohlstedt, D. L. & Holtzman, B. K. (2009). "Shearing melt out of the Earth: An experimentalist's perspective on the influence of deformation on melt extraction" Annual Rev. Earth Planet. Sci. **37**: 561-593.

Korenaga, J. & Kelemen, P. B. (1997). "Origin of gabbro sills in the Moho transition zone of the Oman ophiolite: Implications for magma transport in the oceanic lower crust" Journal of Geophysical Research **102** (B12:27): 729- 27,749.

Lavier, L. L., & Manatschal, G. (2006). "A mechanism to thin the continental lithosphere at magma-poor margins". Nature, **440**: 324-328.

Lee, W. J., & Wyllie, P. J. (2000). " The system CaO-MgO-SiO_2-CO_2 at 1 GPa, metasomatic wehrlites, and primary carbonate magmas" Contrib. Mineral Petrol. **138**: 214-228.

le Roux, A., Class, C. (2014). "Metasomatism of the Pan-African lithospheric mantle beneath the Damara Belt, Namibia, by the Tristan mantle plume: geochemical evidence from mantle xenoliths." Contrib. Mineral. Petrol. **168**(1046). doi: 10.1007/s00410-014-1046-y

Lorand, J-P., Reisburd, L., Bedini, R. M. (2003). "Platinum-group elements and melt percolation processes in Sidamo spinel peridotite xenoliths, Ethiopia, East Africa Rift". Chemical Geology. **196**. 57-75.

MacGregor, I. D. (2015). "Empirical geothermometers and geothermobarometers for spinel peridotite phase assemblages" International Geology Review **57**, *15*: 1940-1974.

McWilliams, M. O. (1981). “Palaeomagnetism and Precambrian tectonic evolution of Gondwana”. Developments in Precambrian Geology, **4**: 649-687.

Meshesha, D., Shinjo, R., Matsumura, R., Chekol, T. (2011). “Metasomatized lithospheric mantle beneath Turkana depression in southern Ethiopia (the East Africa Rift): Geochemical and Sr-Nd-Pb isotopic characteristics” Contrib. Mineral. Petrol. **162**: 889-907.

Muntener, O., Manatschal, G., Desmurs, L., Pettke, T. (2010). "Plagioclase peridotites in ocean-continent transitions: Refertilized mantle domains generated by melt stagnation in the shallow mantle lithoshere." Journal of Petrology **51**: 255-294.

Mohr, P. (1983). “Ethiopian flood basalt province”. Nature. **303**. 577-584.

Moore, W.B., Schubert, G., Tackley, P.J., (1999). “The role of rheology in lithospheric thinning by mantle plumes”. Geophysical Research Letters **26**, 1073–1076.

Morency, C., Doin, M.P., Dumoulin, C., (2002). “Convective destabilization of a thickened continental lithosphere”. Earth and Planetary Science Letters **202**, 303–320.

Nielson, J. E., & Wilshire, H. G. (1993). “Magma transport and metasomatism in the mantle: A critical review of current geochemical models” American Mineralogist **78**: 1117-1134.

Ottonello, G. (1980). “Rare earth abundances and distribution in some spinel peridotite xenoliths from Assab (Ethiopia)” Geochimica et Cosmochimica Acta **44**: 1885-1901.

Orlando, A., Abebe, T., Manetti, P., Santo, A. P., Corti, G. (2006). "Petrology of mantle xenoliths from Megado and Dilo, Kenya Rift, Southern Ethiopia." Ofioliti **31**(2): 71-87.

Pik, R., Deniel, C., Coulon, C., Yirgu, G., Marty, B. (1999). "Isotopic and trace element signatures of Ethiopian flood basalts: Evidence for plume- lithosphere interactions." Geochimica et Cosmochimica Acta **63**(15): 2263-2279.

Pilet, S., Herdandez, J., Sylvester, P., Poujol, M. (2005). “The metasomatic alternative for ocean island basalt chemical heterogeneity” Earth and Planetary Science Letters **236**: 148-166.

Putirka, K. D. (2008). “Thermometers and barometers for volcanic systems” Reviews in Mineralogy & Geochemistry **69:** 61-120.

Reisberg, L., Lorand, J-P., Bedini, R. M. (2004). “Reliabilty of Os model ages in pervasively metasomatized continental mantle lithosphere: a case study of Sidamo spinel peridotite xenoliths (East Africa Rift, Ethiopia)”. Chemical Geology. **208**. 119-140.

Roger, S., Dautria, J.-M., Coulon, C., Pik, R., Yirgu, G., Michard, A., Legros, P., Ayalew, D. (1999). "An insight on the nature, composition and evolution of the lithospheric mantle beneath the north-western Ethiopian plateau: the ultrabasic xenoliths from the Lake Tana Province." Acta Vulcanologica **11**(1): 161-198.

Rogers, N.W. (2006). “Basaltic magmatism and the geodynamics of the East African Rift System.” In: Yirgu, G., Ebinger, C. J., Maguire, P. K. H. (Eds.), The Afar Volcanic Province within the East African Rift System. Geol. Soc. Spec. Publ., **259**. 77-93.

Rooney, T.O., Furman, T., Yirgu, G., Ayalew, D. (2005). "Structure of the Ethiopian lithosphere: Xenolith evidence in the Main Ethiopian Rift". Geochimica et Cosmochimica Acta. **69**. (15). 3889-3910.

Rooney, T. O. (2010) "Geochemical evidence of lithospheric thinning in the southern Main Ethiopian Rift" Lithos **117**: 33-48.

Rooney, T. O., Hertzberg, C., Bastow, I. (2011). "Elevated mantle temperature beneath East Africa" Geology **40**, *1*, 27-30.

Rooney, T. O., Bastow, I. D., Keir, D., Mazzarini, F., Movsesian, E., Grosfils, E. B., Zimbelman, J. R., Ramsey, M. S., Ayalew, D., Yirgu, G. (2014a) "The protracted development of focused magmatic intrusion during continental rifting" Tectonics **33**: 875- 897.

Rooney, T. O., Nelson, W. R., Dosso, L., Furman, T., Hanan, B. (2014b). "The role of continental lithosphere metasomes in the production of HIMU-like magmatism on the northeast African and Arabian plates" Geology **42**: 419-422.

Rudnick, R. L., McDonough, W. F., Chappell, B. W. (1993). "Carbonatite metasomatism in the northern Tanzanian mantle: petrographic and geochemical characteristics" Earth and Planetary Science Letters **114**: 463-475.

Sanfilippo, A., Tribuzio, R., Tiepolo, M. (2014). "Mantle-crust interactions in the oceanic lithosphere: Constraints from minor and trace elements in olivine." Geochimica et Cosmochimica Acta **141**: 423-439.

Seyler, M., & Bonatti, E. (1997). "Regional-scale melt-rock interaction in lherzolitic mantle in the Romanche Fracture Zone (Atlantic Ocean)" Earth and Planetary Science Letters **146**: 273-287.

Skemer, P., Karato, S. (2008). "Sheared lherzolite xenoliths revisited." Journal of Geophysical Research: Solid Earth **113**. doi: 10.1029/2007JB005286

Sobolev, A. V., Hofmann, A. W., Kuzmin, D. V., Yaxley, G. M., Arndt, N. T., Chung, S-L., Danyushevsky, L. V., Elliott, T., Frey, F. A., Garcia, M. O., Gurenko, A. A., Kamenetsky, V. S., Kerr, A.C., Krivolutskaya, N. A., Matveinkov, V. V., Nikogosian, I. K., Rocholl, A., Sigurdsson, I. A., Sushchevskaya, N. M., Teklay, M. (2007). "The amount of recycled crust in sources of mantle-derived melts" Science **316**: 412-417.

Spiegelman, M., & Kelemen, P. B. (2003). "Extreme chemical variability as a consequence of channelized melt transport" Geochemistry, Geophysics, Geosystems **4**, *7*: 1-18.

Stein, M. & Goldstein S. L. (1996). "From plume head to continental lithosphere in the Arabian-Nubian shield" Nature **382**: 773-778.

Stern, R. J. (1994). "Arc assembly and continental collision in the Neoproterozoic East African Orogen: Implications for the consolidation of Gondwanaland" Annual Rev. Earth Planet Sci. **22**: 319- 351.

Stevenson, D. J. (1989). "Spontaneous small-scale melt segregation in partial melts undergoing deformation" Geophysical Research Letters **16** (9): 1067-1070.

Stosch, H-G. (1982). "Rare earth element partitioning between minerals from anhydrous from spinel peridotite xenoliths". Geochimica et Cosmochimica Acta **46**: 793-811.

Suhr, G. (1999). “Melt migration under oceanic ridges: influences from reactive transport modeling of upper mantle hosted dunites” Journal of Petrology **40** (4): 575-599.

Sun, C., Liang, Y. (2014). "An assessment of subsolidus re-equilibration on REE distribution amoung mantle mineral olivine, orthopyroxene, clinopyroxene, and garnet in peridotites." Chemical Geology **372**: 80-91.

Sun, S. S. & McDonough, M. H. (1989). “Chemical and isotopic systematic of oceanic basalts: Implications for mantle composition and processes”, in *Magmatism in the Ocean basins*, edited by A. D. Saunders. Geol. Soc. London. Spec. Publ. **42**: 313-345.

Takazawa, E., Frey, F. A., Shimizu, N., Obata, M., Bodinier, J. L. (1992). “Geochemical evidence for melt migration and reaction in the upper mantle”. Nature **359**: 55-58.

Tommasi, A., Vauchez, A., Fernandes, L. A. D., Porcher, C. C. (1994). “Magma-assisted strain localization in an orogen-parallel transcurrent shear zone of southern Brazil” Tectonics **13** (2): 421-437.

Tommasi, A., Vauchez, A., Ionov, D. (2008). “Deformation, static recrystallization, and reactive melt transport in shallow subcontinental mantle xenoliths (Tok Cenozoic volcanic field, SE Siberia)” Earth and Planetary Science Letters **272**: 65-77.

Van der Wal, D., Chopra, P., Drury, M., Gerald, J. F. (1993). “Relationships between dynamically recrystallized grain size and deformation conditions in experimentally deformed olivine rocks”. Geophysical Research Letters. **20:** (14): 1479-1492.

van Wijk, J., van Hunen, J., Goes, S., (2008). “Small-scale convection during continental rifting: evidence from the Rio Grande rift”. Geology **36**, 575–578.

Vauchez, A., Tommasi, A., Barruol, G. (1998). “Rheological heterogeneity, mechanical anisotropy and deformation of the continental lithosphere” Tectonophysics, **296**: 61-86.

Voigt, M., & von der Handt, A. (2011). “Influence of subsolidus processes on the chromium number in spinel in ultramafic rocks” Contrib. Mineral. Petrol. **162**: 675-689.

Warren, J. M., Hirth, G., Kelemen, P. B. (2008). “Evolution of olivine lattice preferred orientation during simple shear in the mantle” Earth and Planetary Science Letters **272**: 501-512.

Warren, J. M., Hauri, E. H. (2014). "Pyroxenes as tracers of mantle water variations." Journal of Geophysical Research: Solid Earth **119**. doi: 10.1002/2013JB010328

Wiessel, J. K., & Karner, G. D. (1989) “Flextural uplift of rift flanks due to mechanical unloading of the lithosphere during extension” Journal of Geophysical Research, **94** (B10): 13, 919-950.

Weyer, S., Münker, C., Mezger, K. (2003). “Nb/Ta, Zr/Hf and REE in the depleted mantle: implications for the differentiation history of the crust-mantle system” Earth and Planetary Science Letters **205**: 309-324.

Wilson, A. H. (1982). “The geology of the Great Dyke, Zimbabwe: The ultramafic rocks” Journal of Petrology **23**: 240-292.

Wilson, D. H., Aster, R., West, M., Ni, J., Grand, S., Gao, W., Baldridge, W. S., Semken, S., Patel, P. (2005). “Lithopsheric structure of the Rio Grande rift” Letters to Nature, **433**: 851-855.

Whitehead, J. A., & Kelemen, P. (1994). “Fluid and thermal dissolution instabilities in magmatic systems, Magmatic Systems”.Magmatic Systems **57**, 355-379.

Wolfenden, E., Ebinger, C., Yirgu, G., Deino, A., Ayalew, D. (2004). "Evolution of the northern Main Ethiopian rift: birth of a triple junction." Earth and Planetary Science Letters **224**: 213-228.

Wolfenden, E., Ebinger, C., Yirgu, P. R. Renne, and S. P. Kelley. (2005). “Evolution of a volcanic rifted margin: Southern Red Sea, Ethiopia. Geological Society of America Bulletin **117**: 846-864.

Yaxley, G. M., Green, D. H., & Kamenetsky, V. (1998). “Carbonatite metasomatism in the southeastern Australian lithosphere”. Journal of Petrology, **39** (11-12), 1917-1930.

Zeyen, H., et al., (1997). “Styles of continental rifting: crust–mantle detachment and mantle plumes”. Tectonophysics **278**, 329–352.

Zhang, H-F. (2005). “Transformation of lithospheric mantle through peridotite-melt reaction: a case of Sino-Korean craton” Earth and Planetary Science Letters **273**: 768-780.

Ziegler, P.A., Cloetingh, S., (2004). “Dynamic processes controlling evolution of rifted Basins”. Earth Science Reviews **64**, 1–50.